Fast Estimation of Specific Absorption Rate for Magnetic Resonance Imaging

by

Yu Shao

A dissertation submitted to the Graduate Faculty of
Auburn University
in partial fulfillment of the
requirements for the Degree of
Doctor of Philosophy

Auburn, Alabama
August 1, 2015

Keywords: SAR, MRI, RF coil, FDTD, Fast Estimation Method

Approved by

Shumin Wang, Chair, Associate Professor of Electrical and Computer Engineering
Lloyd Stephen Riggs, Professor of Electrical and Computer Engineering
Michael Baginski, Associate Professor of Electrical and Computer Engineering
Soo-Young Lee, Professor of Electrical and Computer Engineering

Abstract

Specific absorption rate (SAR) is a main safety concern in magnetic resonance imaging (MRI). The radio frequency (RF) power deposition and SAR level have a significant impact on RF coil and pulse design. In high field MRI, multichannel RF transmission is widely used to mitigate B_1 field inhomogeneity. A specific B_1 map can be generated by adjusting the magnitude, phase and pulse shape of each coil. The dynamic changing of transmission will result in a subject dependent SAR distribution. Therefor we need to evaluate SAR in real subjects in real time. In addition, since the SAR is subject dependent, we need to investigate a large number of samples to get the statistical character of SAR. However, SAR evaluation requires full-wave electromagnetic simulation, which is time-consuming. So it is necessary to develop fast SAR evaluation methods. This dissertation presents some approaches to fast estimate the SAR in human body during MRI scan. Specifically, we present the following topics: (1) a brief introduction to finite-difference time-domain (FDTD) method is given and we verify the program by a scattering problem, a good agreement between analytical solution and simulation results is obtained; (2) a parallel implementation of FDTD based on GPU is provided and its performances and efficiency are compared with CPU; (3) SAR and temperature calculation are introduced. The B_1^+ field, SAR and temperature distribution within a human head in the birdcage coil at several frequencies as high as 498MHz are presented; (4) a hybrid technique that combines method of moments (MoM) and FDTD is presented to estimate local SAR rapidly, the accuracy and efficiency of this method are studied in detail; (5) a fast approach for statistical simulation of SAR based on the unscented transform is investigated, the number of sample points can be reduced and a meaningful

safety margin can be established efficiently by this method. The methods presented in this dissertation can speed up the SAR estimation procedure, and they will be helpful to the coil design and SAR monitoring in MRI practice.

Acknowledgments

I am very grateful to my advisor, Dr. Shumin Wang for his support and guidance throughout my graduate studies. Thanks for giving me the opportunity to study and work in Auburn and thanks for his invaluable advice. His diligence and passion to research always inspire me.

I would like to thank my advisory committee members, Dr. Lloyd Stephen Riggs, Dr. Michael Baginski and Dr. Soo-Young Lee for teaching me course and giving me advice and support on my dissertation.

I would like to show my appreciation to my past and current colleagues in our research group, including Hai Lu, Xiaotong Sun, Shuo Shang, Ziyuan Fu, Ran Cheng and Tiantong Ren for their assistance and friendship.

I would like to thank all the Professors who taught me during my graduate study and thank everyone who helped me in some way.

Thanks to my parents and other family members for their love, encouragement and support.

Table of Contents

List of Tables

List of Figures

List of Abbreviations

API	Application Program Interface
CPU	Central Processing Unit
CFLN	Courant-Freidrichs-Lewy Number
CT	Computed Tomography
CUDA	Computer-Unified Device Architecture
FDA	Food and Drug Administration
FDTD	Finite-Difference Time-Domain
GPU	Graphics Processing Unit
IEC	International Electrotechnical Commission
MoM	Method of Moments
MRI	Magnetic Resonance Imaging
NMR	Nuclear Magnetic Resonance
PML	Perfectly Matched Layer
RF	Radio Frequency
SAR	Specific Absorption Rate
SD	Standard Deviation
SM	Streaming Multiprocessors
SNR	Signal-to-Noise Ratio
TF/SF	Total-Field/Scattered-Field

Chapter 1 Introduction

Magnetic resonance imaging (MRI) is a powerful medical imaging technique which can produce high resolution and high contrast anatomic images through the human body. It was first proposed by Lauterbur in 1973, for which he was awarded Nobel Prize in 2003. After that, a large number of imaging techniques have been developed hence the image quality has dramatically increased. Unlike x-ray and computed tomography (CT), MRI does not use the hazardous ionizing radiation. Particularly MRI provides higher soft-tissue contrast than other medical techniques. So this risk free technique plays an important role in medical imaging area.

MRI is based on the physical phenomenon called nuclear magnetic resonance (NMR). When an atomic nucleus is placed in a static magnetic field, it has two states: higher energy state and lower energy state. Nuclei can transfer between these two states by emitting or absorbing photons whose energy equal to the energy difference between the two states. Actually the photons are electromagnetic fields of certain frequency which is proportional to the strength of the static magnetic field and is known as Larmor Frequency. In MRI, the static magnetic field is called B_0 field. Radiofrequency (RF) coil transmits electromagnetic field of Larmor frequency which is called B_1 field to excite the nuclei. The nuclei in the lower energy state absorb the energy and jump to the higher energy state. After RF pulse is turned off, to recover the thermal equilibrium, the excess nuclei in the higher energy state will relax back to the lower energy state by emitting electromagnetic fields which can be received by RF coil. The energy difference between the two states of nuclei is proportional to the strength of the external magnetic field B_0, and so does the Larmor frequency. By changing the main magnetic field as a function of position, the energy difference can be made different at each point in the object. In MRI this procedure is done by another set of coils which is called

gradient coils. Therefore, the frequency of electromagnetic fields emitted by the nuclei and received by RF coil are different from point to point. This difference can be used to determine spatial information about nuclei.

1.1 Static field $\boldsymbol{B_0}$

Atomic nuclei have a property called spin. That is the proton with positive charges rotates at a high speed about its axis. The rotating charges produce a small magnetic field called magnetic moment μ. The nuclei specie discussed in the dissertation is limited to hydrogen, because it is the most significant nucleus for most MRI research due to its large concentration in the human body as a composition of water molecule. When placed in a static magnetic field B_0, the two states of hydrogen nuclei are magnetic moment parallel and anti-parallel to B_0. Consider a bulk sample contains many individual magnetic moments (Figure 1.1a). The average behavior of so many individual spins result in a net magnetic moment aligns with B_0, which is called magnetization M. The strength of the magnetization is proportional to B_0, which is [1]:

$$\mathrm{M}_0 = \sum_{n=1}^{N_s} \mu_n = \frac{B_0 \gamma^2 h^2}{4kT} P_D \tag{1.1}$$

where N_s is the number of individual magnetic moments, γ is known as gyromagnetic ratio, h is Planck's constant, k is Boltzmann's constant, T is temperature (from absolute zero), and P_D is proton density.

By MRI convention, B_0 field points in the z direction. B_0 produces a torque on the magnetization which satisfies the following equation:

$$\frac{d\vec{M}}{dt} = \gamma \vec{M} \times \vec{B} \tag{1.2}$$

Suppose the initial angle between magnetization vector and z-axis is α, the solution of (1.2) is:

$$M_x(t) = M_0 sin\alpha \, cos(-\omega t + \varphi) \tag{1.3a}$$

$$M_y(t) = M_0 sin\alpha \, sin(-\omega t + \varphi) \tag{1.3b}$$

$$M_z(t) = M_0 cos\alpha \tag{1.3c}$$

where

$$\omega = \gamma B_0 \tag{1.4}$$

ω is the Larmor frequency which is mentioned before, and φ is an arbitrary angle. These equations describe a precession of M around B_0. After the RF magnetic field B_1 which is perpendicular to the z-axis is applied, magnetization gets another procession around B_1 and it will be tipped away from the z-axis (Figure 1.1b). The tip angle depends on amplitude and duration of B_1, which is given by:

$$\alpha = \gamma \int_0^{\tau_p} B_1(t)dt \tag{1.5}$$

In the case of rectangular pulse, the tip angle is simplified as:

$$\alpha = \gamma B_1 \tau_p \tag{1.6}$$

From (1.3a) and (1.3b), the transverse component of magnetization is time varying. According to Faraday induction, it will induce a voltage in the receiving coil located outside the sample, this is how the signal in MRI comes.

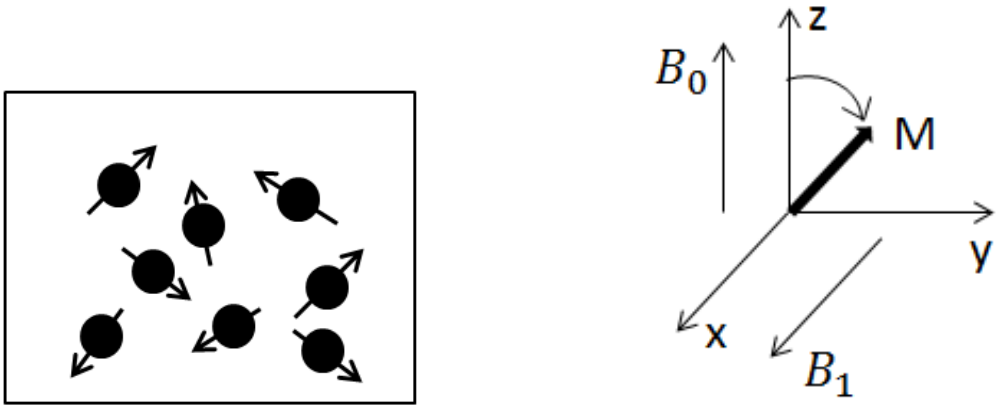

(a) (b)

Figure 1.1 (a) Before B_1 field applies, random individual magnetic moments in a bulk of sample; (b) After B_1 field applies, magnetization vector is tipped away from z-axis by B_1 field.

To improve MRI quality, modern scanners have very high B_0 field because signal-to-noise ratio (SNR) increases linearly with B_0. On one hand, the signal induced in the receiving coil increases as the square of B_0 due to two independent factors: (1) from equation (1.1), the magnetization is proportional to the B_0 field and (2) from equation (1.2), the Larmor frequency is proportional to the B_0 field; the rate of change of magnetic flux will increase with frequency, so by Faraday's electromagnetic induction law, the signal induced in the coil will increase with frequency. On the other hand, the noise in MRI mainly comes from eddy currents induced in the patient. As Larmor frequency increases, the frequency of eddy currents also increases and so does the noise voltage induced in receiving coil. So the SNR is linearly proportional to the strength of B_0.

1.2 RF coil

In MRI, RF coil is used to couple the energy between nuclei and external circuit. Specifically, RF coil generate B_1 magnetic field to tip the magnetization away from the alignment with B_0 field so that it can precess. The magnetization rotates at Larmor frequency in a left-handed sense relative to the main field. So in order to excite nuclei effectively, the frequency of B_1 field should be equal to Larmor frequency. For hydrogen, the Larmor frequency under several static magnetic fields is shown in the following table:

Table 1.1 Larmor frequency of hydrogen under several static magnetic fields.

B_0 field (Tesla)	1.5	3	7	11.7
Larmor frequency (MHz)	64	128	298	498

Any RF magnetic field can be decomposed into two circularly polarized components. For example, for a x polarized field [2]:

$$B_1 = \hat{x}B_{10}cos\omega t = B_1^+ + B_1^- \tag{1.7}$$

where

$$B_1^+ = \frac{1}{2} B_{10}(\hat{x}cos\omega t - \hat{y}sin\omega t) \tag{1.8}$$

$$B_1^- = \frac{1}{2} B_{10}(\hat{x}cos\omega t + \hat{y}sin\omega t) \tag{1.9}$$

B_1^+ and B_1^- are the left-handed and right-handed circularly polarized components with respect to the static magnetic field respectively. Due to the magnetization precesses in a left-handed sense, the nuclei are only sensitive to the B_1^+ component, so the circularly polarized coil is more efficient than linearly polarized one.

There are two basic requirements on RF coils so that we can obtain high quality MRI image. First, transmit coils should be able to produce homogeneous B_1 field at Larmor frequency in the volume of interest. Since the tip angle is a function of B_1 field magnitude, inhomogeneity will distort the receiving signal and introduce artifact into image. A homogeneous B_1 field ensures the nuclei can be excited uniformly. Second, the receive coils should have high signal-to-noise ratio. As mentioned before, SNR is linearly proportional to the strength of B_0. However, high field MRI will make B_1 field inhomogeneous. When B_0 increases, the Larmor frequency increases and the wavelength of B_1 decreases. Under 3T, the RF wavelength in human body is similar to the dimension of body trunk. The wave interference becomes obvious in small wavelength, which in turn causes the inhomogeneity. Further RF effects in high frequency such as eddy current and dielectric effect altogether distort the B_1 field pattern.

Some of the most common RF coils used in MRI are shown in the Figure 1.2.

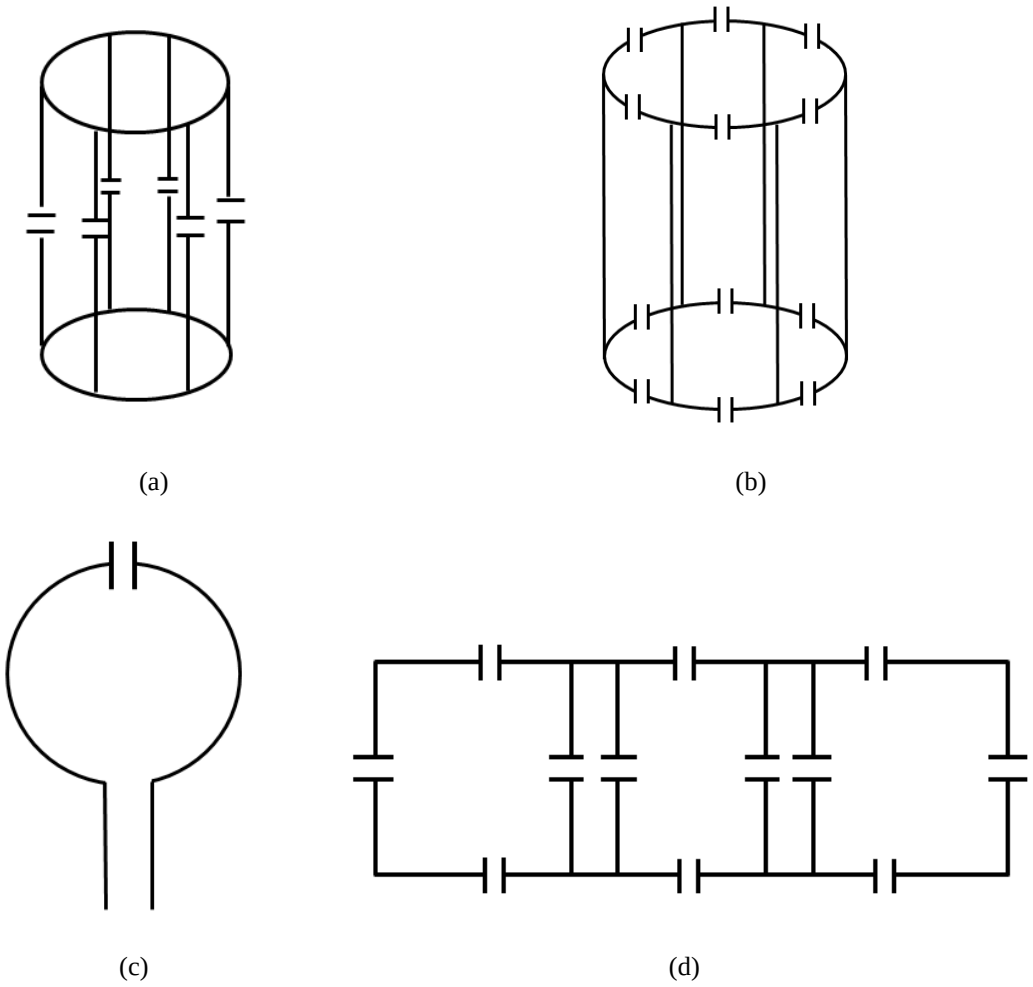

Figure 1.2 schematic diagram of several RF coils: (a) Lowpass birdcage coil; (b) Highpass birdcage coil; (c) Single-loop coil; (d) Coil array.

According to the shapes, RF coils can be divided into two types: volume coils and surface coils. Volume coils are designed to surround the object being imaged, and they can produce a very homogeneous B_1 field over a large volume within them. Birdcage coil, shown in Figure 1.2 (a) and (b), is a typical volume coil. This coil combines lumped capacitors with distributed inductance to form a volume resonator. When the birdcage coil is tuned to a certain mode, it will produce a very uniform B1 field. Surface coils, as shown in Figure 1.2 (c) and (d), are usually smaller than volume coils and are placed on the surface in very close proximity to the object. Hence they have higher SNR due to they only receive noise from nearby region. Figure 1.2 (c) shows a single loop coil. The coil will resonate at Larmor frequency by tuning to capacitor. Figure 1.2 (d) is a phased array which is made up of several

single loops. By adjusting the magnitude and phase of each loop, the array can produce a uniform magnetic field. However its performance of homogeneous B1 field is relatively poorer than volume coil.

1.3 SAR

When human is exposed to the RF electromagnetic field, the energy will deposit into the body tissue and cause body heating. Specific absorption rate (SAR) is the RF power absorbed by per unit of mass of an object, and is measured in watts per kilogram (W/kg). SAR is defined as:

$$SAR = \frac{\sigma |E|^2}{\rho} \tag{1.10}$$

where σ is the electrical conductivity, E is the RMS electric field and ρ is the density. SAR value is related to flip angle, B_0 strength, RF pulse duty cycle, patient size and transmit coil type. To obtain a large flip angle, the RF magnetic field should be large, which makes a large RF electric field and in turn a large SAR. When the magnitude of magnetic field is fixed, the electric field is proportional to the frequency by Faraday's law. So when B_0 increases, the Larmor frequency increases and so does the electric field. Furthermore, the electric conductivities of body tissue get larger as the frequency increases. These factors altogether lead to a large SAR in high field MRI, SAR increases with the square of B_0.

There are two types of SAR: local SAR and global SAR. Local SAR is defined at each individual point, while global SAR is obtained by averaging the local SAR over a specified volume of tissue, for example head, torso or whole body. High SAR value indicates the potential for temperature rises in the tissue. The temperature increasing in the body in MRI depends on the thermal properties of the tissue, the thermal diffusion mechanism, RF pulse duration and duty cycle. Because the field pattern changes with the frequency, the SAR and temperature distribution also depend on frequency. In the transmit coil array case, to obtain a

homogeneous field, different combination of magnitude and phase will be applied on different scanning sample. So the SAR distribution is influenced by variable magnitude and phase excitation. If there are some metallic medical implants in patient's body, extreme high SAR may occur near the tip of the metallic wire and cause local heating. This heating due to metallic implants depends on the shape, dimension, location and orientation of the implants [24]. To avoid local thermal damage or whole-body thermoregulatory problems, the supervision of SAR in high field MRI is crucial.

The Food and Drug Administration (FDA) has suggested the limits of SAR in MRI [3]. For instance, the ratio of maximum 1-gram local SAR to whole-head SAR is 2.7. In International Electrotechnical Commission (IEC) [4, 5], the limit for the ratio of maximum 10-gram local SAR to whole-head SAR is 3.12. The limits of absolute value of local SAR and global SAR are shown in Table 1.2 and Table 1.3.

Table 1.2 FDA regulatory limits for the local SAR and global SAR.

Site	Dose	Time (min)	SAR (W/kg)
Whole body	Averaged over	15	4
Head	Averaged over	10	3
Head or torso	Per gram of tissue	5	8
Extremities	Per gram of tissue	5	12

Table 1.3 IEC regulatory limits for the local SAR and global SAR.

	Whole body SAR (W/kg)	Partial body SAR (W/kg)	Head SAR (W/kg)	Local SAR (W/kg)		
Body region	Whole body	Exposed part	Head	Head	Trunk	Extremities
Normal	2	2-10	3.2	10	10	20
1st level controlled	4	4-10	3.2	20	20	40
2nd level controlled	>4	> (4-10)	>3.2	>20	>20	>40

1.4 Document overview

From 1990s, with the development of computer technique, many numerical methods have been applied to analyze MRI RF coil. Grandolfo et al. [6] calculated the SAR in a human-torso model by three-dimensional impedance method. Collins et al. [7] studied B_1 field in a birdcage coil at 125 MHz using finite-element method. In 1998, they evaluated B_1 field and SAR distribution in a heterogeneous human head model by FDTD method. Chen et al. [8] used FDTD combined with the method of moments to compute the electromagnetic fields in anatomically accurate model up to 256 MHz. Wang et al. [9] applied combined field integral equation method to analyze eight-channel head coil arrays for 7T MRI. Later they presented a fast integral-equation method for large-scale human model simulation [11]. They also developed a FDTD and finite-element time-domain hybrid method for RF coil simulation [10]. S. Wolf et al. [12] discussed how to reduce the effort (simplifications of the tissue and reduction of human model extent) while maintaining robust results in SAR simulation.

Since SAR supervision is critical in MRI, many scholars have done a lot of research on this topic [13][14]. Ibrahim et al. [15] studied RF power requirements and B_1 field homogeneity for ultra-high-field human MRI. Zhangwei Wang et al. [16] presented SAR and temperature in human head in a volume coil at several different frequencies; they compared these values with regulatory limits. The field and SAR pattern depends on frequency and individual patient. Neufeld et al. [17] calculated the maximum increase of SAR for three different human models in multi-channel transmit coil at 128 MHz. Homann et al. [18] discussed SAR management by RF shimming for a 3T coil with eight transmit elements. Temperature increasing caused by RF heating can be calculated by bio-heat equation. Collins et al. [19] calculated temperature and SAR for human head within volume and surface coil at 64 MHz and 300 MHz. Lier et al. [20] evaluated temperature in the head after exposure to a 300 MHz RF field using two thermal simulation methods. Massire et al. [21] conducted thermal

simulations for parallel transmission MRI. Mrubach et al. [22] investigated the local thermal hotspots in four anatomical human models within 1.5T body coil. Sukhoon et al. [23] verified the numerical simulation by comparing it with the measurement of temperature increase in a phantom and vivo.

Metallic implant is a main safety concern in MRI. Henry S. Ho [24] calculated the increased SAR caused by metallic implant in body at 64 MHz in a birdcage body coil. Carmichael et al. [25] investigated the heating of intracranial electroencephalograph electrodes during 1.5T and 3T MRI. Nordbeck et al. [26] measured the RF-induced current in a cardiac pacemaker lead and studied the impact of device configuration on the MRI-related heating. Tagliati et al. [27] performed a survey of the safety of MRI in patients implanted with deep brain stimulation device. Liu et al. [28] did computational and experimental study on the MRI-related heating in orthopedic implant.

1.5 Dissertation contributions and outline

As we have mentioned before, SAR is a main safety concern in MRI practice, especially when it comes to metallic medical implants. So it is important to get the knowledge of SAR and temperature distribution in human body during MRI. However, it is impossible to measure the local SAR and temperature throughout the body. Therefore, numerical simulation is an efficient way to predict heating situation in human body. Transmit coil array is widely used, different magnitude/phase combination in the array will result in different field pattern, and so do the SAR and temperature. Thus we need to know in real time whether the safety constrains are violated in different human model. This dissertation presents some approaches to fast estimate the SAR in MRI.

The rest of the dissertation is organized in the following way.

Chapter 2 presents the fundamental theory of Finite-Difference Time-Domain (FDTD) method, which is the numerical method we used to calculate electromagnetic field in human

body. We discuss some numerical concerns when it is applied in RF coil simulation. To verify the validity of the program, a scattering problem which has analytical solutions is simulated and the comparisons of FDTD results and analytical results are presented.

One way to achieve fast field estimation is using the graphical processing unit (GPU) to accelerate FDTD. This topic is discussed in Chapter 3. GPU architecture is briefly introduced and the Computer-Unified Device Architecture (CUDA) parallel programing model is presented. We develop a parallel code for FDTD on GPU and compare its performance with sequential code. A birdcage coil is designed as an application example; we calculate the fields produced by this coil in a phantom at different frequency and discuss the results.

In Chapter 4, after obtaining the electromagnetic fields in human body, we present the SAR calculation algorithm. Then we evaluate the temperature distribution with local SAR by using bio-heat equation. A high resolution human model is described and the birdcage coil with this model is studied. The B_1^+ map, SAR distribution and temperature increasing in human head are presented.

In Chapter 5, a rapid local SAR estimation method is developed. It is a hybrid technique that combines method of moments (MoM) and FDTD. In first step, MoM is used to solve the strong coil/body coupling in frequency domain and obtain the fields on an imaginary surface surrounding the human body. Then these fields are injected into FDTD simulation by treating them as Dirichlet boundary condition. Validation and simulation examples are presented.

Chapter 6 explores statistical SAR simulation by unscented transform method. Since many factors that may influence the SAR value exhibit uncertainty, it is more appropriate to treat the SAR estimation as a statistical procedure. The conventional statistical simulation methods such as the Monte Carlo method require a large number of random sample points which is very time-consuming. Unscented transform which only requires a few deterministic sample points is explored to accelerate the statistical simulation of SAR.

Chapter 7 concludes this dissertation.

The outline of the work in this dissertation can be illustrated by Figure 1.3.

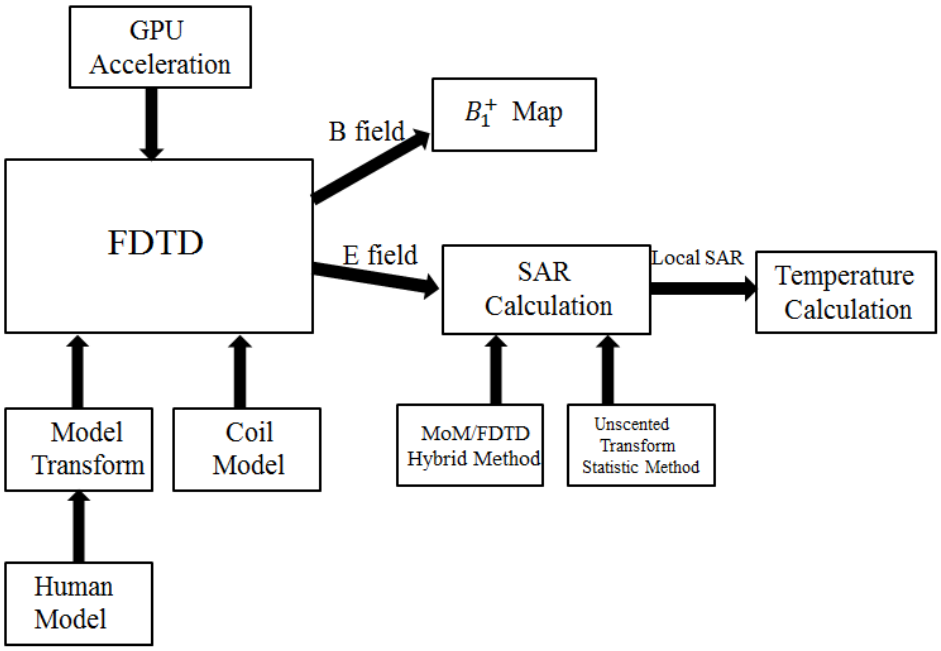

Figure 1.3 Outline of the work in this dissertation. FDTD method is the numerical simulation method used in this dissertation. The inputs of FDTD are human model and coil model. The outputs of FDTD can be used to calculate B_1^+ and SAR, then the temperature can be calculated by local SAR value. GPU is applied to accelerate FDTD. A hybrid technique and a statistic method are proposed to estimate the SAR rapidly.

Chapter 2 Finite-Difference Time-Domain Method

Finite-difference time-domain method, which is introduced by Yee in 1966, is an efficient tool for solving Maxwell's equations. This method is based on a set of simple formulations and is a fully explicit method without complex matrix computation. It is accurate and robust. It calculates electromagnetic fields in time-domain, the wide band frequency-domain results can be obtained in one single simulation by Fourier transform. It uses volume grid to discretize the object, so it can easily handle inhomogeneous geometries consisting of different types of material. In addition, parallel computation algorithms can be easily used in FDTD. These advantages make FDTD widely used in various engineering applications for electromagnetic modeling. Since the human body is a composite geometry composed of many tissues with different electric properties, FDTD is the most attractive tool in MRI coil simulation.

2.1 Basic equations [29, 30]

Maxwell's equations in time-domain are:

$$\nabla \times \vec{H} = \frac{\partial \vec{D}}{\partial t} + \vec{J} \tag{2.1a}$$

$$\nabla \times \vec{E} = -\frac{\partial \vec{B}}{\partial t} \tag{2.1b}$$

$$\nabla \cdot \vec{D} = \rho \tag{2.1c}$$

$$\nabla \times \vec{B} = 0 \tag{2.1d}$$

where $\vec{E}$ is the electric field strength vector, $\vec{D}$ is the electric displacement vector, $\vec{H}$ is the magnetic field strength vector, $\vec{B}$ is the magnetic flux density vector, $\vec{J}$ is the electric current density vector, ρ is the electric charge density. Constitutive relations for linear, isotropic and nondispersive media are:

$$\vec{D} = \varepsilon \vec{E} \tag{2.2a}$$

$$\vec{B} = \mu \vec{H} \tag{2.2b}$$

$$\vec{J} = \sigma\vec{E} + \vec{J}_i \tag{2.2c}$$

where ε is the permittivity, μ is the permeability and σ is the electric conductivity, $\vec{J}_i$ is the impressed current density.

$$\varepsilon = \varepsilon_0\varepsilon_r \tag{2.3a}$$

$$\mu = \mu_0\mu_r \tag{2.3b}$$

ε_r is the relative permittivity and μ_r is the relative permeability, $\varepsilon_0 \approx 8.854 \times 10^{-12}\, F/m$, $\mu_0 \approx 4\pi \times 10^{-7}\, H/m$. Substitute (2.2a)-(2.2c) into (2.1a)-(2.1d), we can get the following two curl equations for electric field and magnetic field:

$$\nabla \times \vec{H} = \epsilon\frac{\partial\vec{E}}{\partial t} + \sigma\vec{E} + \vec{J}_i \tag{2.4a}$$

$$\nabla \times \vec{E} = -\mu\frac{\partial\vec{H}}{\partial t} \tag{2.4b}$$

Each vector equation in (2.4) can be decomposed into three scalar equations. So in Cartesian coordinate, (2.4) can be represented by the following scalar equations:

$$\epsilon\frac{\partial E_x}{\partial t} + \sigma E_x = \frac{\partial H_z}{\partial y} - \frac{\partial H_y}{\partial z} - J_{ix} \tag{2.5a}$$

$$\epsilon\frac{\partial E_y}{\partial t} + \sigma E_y = \frac{\partial H_x}{\partial z} - \frac{\partial H_z}{\partial x} - J_{iy} \tag{2.5b}$$

$$\epsilon\frac{\partial E_z}{\partial t} + \sigma E_z = \frac{\partial H_y}{\partial x} - \frac{\partial H_x}{\partial y} - J_{iz} \tag{2.5c}$$

$$\mu\frac{\partial H_x}{\partial t} = \frac{\partial E_y}{\partial z} - \frac{\partial E_z}{\partial y} \tag{2.5d}$$

$$\mu\frac{\partial H_y}{\partial t} = \frac{\partial E_z}{\partial x} - \frac{\partial E_x}{\partial z} \tag{2.5e}$$

$$\mu\frac{\partial H_z}{\partial t} = \frac{\partial E_x}{\partial y} - \frac{\partial E_y}{\partial x} \tag{2.5f}$$

The time and space derivatives in (2.5) can be approximated by finite difference which is based on Taylor series expansion:

$$f(x+\Delta x) = f(x) + \Delta x f'(x) + \frac{(\Delta x)^2}{2}f''(x) + \frac{(\Delta x)^3}{6}f'''(x) + \cdots \tag{2.6a}$$

$$f(x-\Delta x) = f(x) - \Delta x f'(x) + \frac{(\Delta x)^2}{2}f''(x) - \frac{(\Delta x)^3}{6}f'''(x) + \cdots \tag{2.6b}$$

Minus (2.6b) from (2.6a), $f'(x)$ can be written as:

$$f'(x) = \frac{f(x+\Delta x)-f(x-\Delta x)}{2\Delta x} + O((\Delta x)^2) \tag{2.7}$$

2.2 FDTD updating equations [29, 30]

In FDTD the three dimensional space is discretized into cells. Each cell is called Yee cell [32] shown in Figure 2.1. With Yee cell, any object of arbitrary shape can be approximated by staircase grid shown in Figure 2.2.

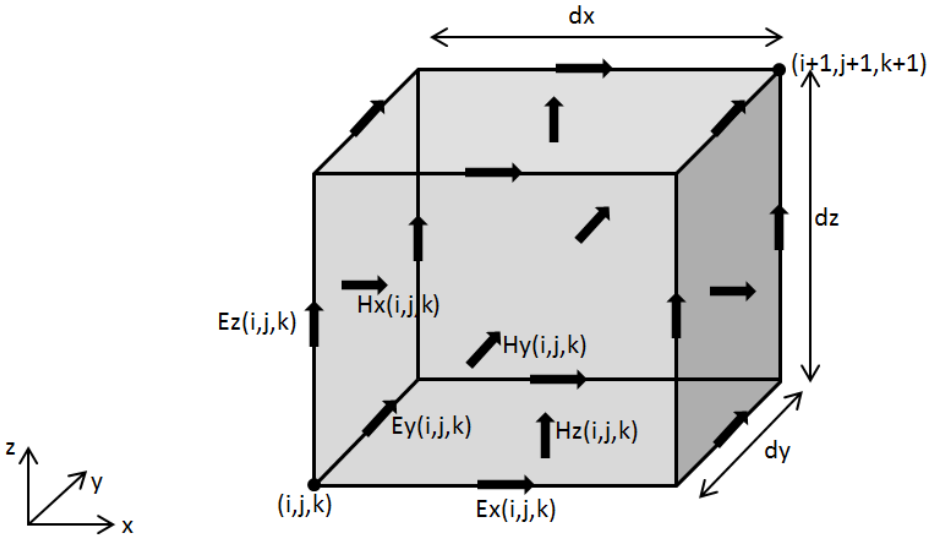

Figure 2.1 Field components in a Yee cell. The electrical field is defined on the center of edge and magnetic field is defined on the center of face. This definition satisfies Faraday's law and Ampere's law.

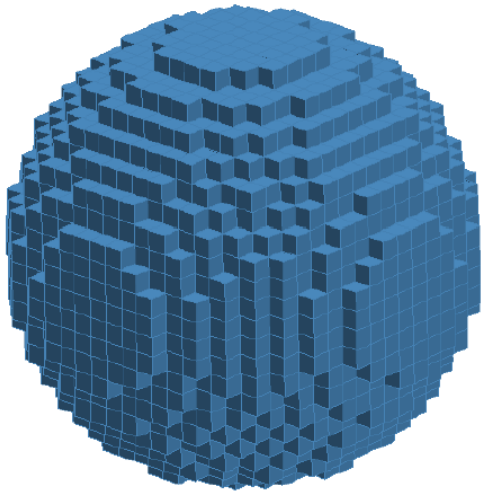

Figure 2.2 A sphere is approximated by staircase grid

In FDTD, electric and magnetic field components are sampled at different special positions and different time instants. Take Figure 2.1 for example, if the cell is indexed as (i,j,k), then the actual positions and instant of each field component are shown in Table 2.1:

Table 2.1 The actual positions and instants of each field component

	x	y	z	t
$E_x^n(i,j,k)$	(i+0.5)Δx	jΔy	kΔz	nΔt
$E_y^n(i,j,k)$	iΔx	(j+0.5)Δy	kΔz	nΔt
$E_z^n(i,j,k)$	iΔx	jΔy	(k+0.5)Δz	nΔt
$H_x^{n+\frac{1}{2}}(i,j,k)$	iΔx	(j+0.5)Δy	(k+0.5)Δz	(n+0.5)Δt
$H_y^{n+\frac{1}{2}}(i,j,k)$	(i+0.5)Δx	jΔy	(k+0.5)Δz	(n+0.5)Δt
$H_z^{n+\frac{1}{2}}(i,j,k)$	(i+0.5)Δx	(j+0.5)Δy	kΔz	(n+0.5)Δt

Applying finite difference scheme to equation (2.5), we can derive updating equation for each field component in Yee cell. Considering the field component indices, they can be written as the following:

$$\begin{aligned} E_x^{n+1}(i,j,k) = {} & \frac{2\varepsilon(i,j,k)-\Delta t\sigma(i,j,k)}{2\varepsilon(i,j,k)+\Delta t\sigma(i,j,k)}E_x^n(i,j,k) \\ & \frac{2\Delta t}{\big(2\varepsilon(i,j,k)+\Delta t\sigma(i,j,k)\big)\Delta y}\left(H_z^{n+\frac{1}{2}}(i,j,k)-H_z^{n+\frac{1}{2}}(i,j-1,k)\right) \\ & -\frac{2\Delta t}{\big(2\varepsilon(i,j,k)+\Delta t\sigma(i,j,k)\big)\Delta z}\left(H_y^{n+\frac{1}{2}}(i,j,k)-H_y^{n+\frac{1}{2}}(i,j,k-1)\right) \\ & -\frac{2\Delta t}{\big(2\varepsilon(i,j,k)+\Delta t\sigma(i,j,k)\big)}J_{ix}^{n+\frac{1}{2}}(i,j,k) \end{aligned} \tag{2.8a}$$

$$\begin{aligned} E_y^{n+1}(i,j,k) = {} & \frac{2\varepsilon(i,j,k)-\Delta t\sigma(i,j,k)}{2\varepsilon(i,j,k)+\Delta t\sigma(i,j,k)}E_y^n(i,j,k) \\ & \frac{2\Delta t}{\big(2\varepsilon(i,j,k)+\Delta t\sigma(i,j,k)\big)\Delta z}\left(H_x^{n+\frac{1}{2}}(i,j,k)-H_x^{n+\frac{1}{2}}(i,j,k-1)\right) \\ & -\frac{2\Delta t}{\big(2\varepsilon(i,j,k)+\Delta t\sigma(i,j,k)\big)\Delta x}\left(H_z^{n+\frac{1}{2}}(i,j,k)-H_z^{n+\frac{1}{2}}(i-1,j,k)\right) \\ & -\frac{2\Delta t}{\big(2\varepsilon(i,j,k)+\Delta t\sigma(i,j,k)\big)}J_{iy}^{n+\frac{1}{2}}(i,j,k) \end{aligned} \tag{2.8b}$$

$$E_z^{n+1}(i,j,k) = \frac{2\varepsilon(i,j,k) - \Delta t\sigma(i,j,k)}{2\varepsilon(i,j,k) + \Delta t\sigma(i,j,k)} E_z^n(i,j,k)$$
$$\frac{2\Delta t}{\big(2\varepsilon(i,j,k) + \Delta t\sigma(i,j,k)\big)\Delta x}\left(H_y^{n+\frac{1}{2}}(i,j,k) - H_y^{n+\frac{1}{2}}(i-1,j,k)\right)$$
$$-\frac{2\Delta t}{\big(2\varepsilon(i,j,k) + \Delta t\sigma(i,j,k)\big)\Delta y}\left(H_x^{n+\frac{1}{2}}(i,j,k) - H_x^{n+\frac{1}{2}}(i,j-1,k)\right)$$
$$-\frac{2\Delta t}{\big(2\varepsilon(i,j,k) + \Delta t\sigma(i,j,k)\big)} J_{iz}^{n+\frac{1}{2}}(i,j,k)$$

(2.8c)

$$H_x^{n+\frac{1}{2}}(i,j,k) = H_x^{n-\frac{1}{2}}(i,j,k)$$
$$\frac{\Delta t}{\mu(i,j,k)\Delta z}\left(E_y^n(i,j,k+1) - E_y^n(i,j,k)\right)$$
$$-\frac{\Delta t}{\mu(i,j,k)\Delta y}\left(E_z^n(i,j+1,k) - E_z^n(i,j,k)\right)$$

(2.8d)

$$H_y^{n+\frac{1}{2}}(i,j,k) = H_y^{n-\frac{1}{2}}(i,j,k)$$
$$\frac{\Delta t}{\mu(i,j,k)\Delta x}\left(E_z^n(i+1,j,k) - E_z^n(i,j,k)\right)$$
$$-\frac{\Delta t}{\mu(i,j,k)\Delta z}\left(E_x^n(i,j,k+1) - E_x^n(i,j,k)\right)$$

(2.8e)

$$H_z^{n+\frac{1}{2}}(i,j,k) = H_z^{n-\frac{1}{2}}(i,j,k)$$
$$\frac{\Delta t}{\mu(i,j,k)\Delta y}\left(E_x^n(i,j+1,k) - E_x^n(i,j,k)\right)$$
$$-\frac{\Delta t}{\mu(i,j,k)\Delta x}\left(E_y^n(i+1,j,k) - E_y^n(i,j,k)\right)$$

(2.8f)

From the equations (2.8a)-(2.8f), the so called leapfrog time marching algorithm can be constructed. It is shown in Figure 2.3:

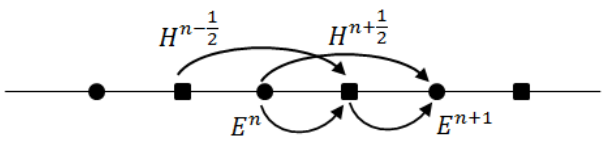

Figure 2.3 Leapfrog time marching algorithm. In the figure, square denotes magnetic field and circle denotes electrical field. In this algorithm, the new field component is updated by the old field component.

Firstly we update $H^{n+\frac{1}{2}}$ by (2.8d)-(2.8f) using $H^{n-\frac{1}{2}}$ and E^n, then E^{n+1} can be updated by (2.8a)-(2.8c) using E^n and $H^{n+\frac{1}{2}}$. Every new field component can be updated by the old field components, so it is an explicit iterative scheme.

2.3 Perfectly matched layer absorbing boundary

Since the computer memory is finite, the FDTD computational space should be truncated on the boundary. In MRI coil simulation, we need to simulate the free space. However, if we truncate the boundary directly, numerical reflection will occur and corrupt the computational domain. To simulate free space, we need a boundary which can absorb the outgoing waves completely to avoid reflections. This type of boundary is called absorbing boundary.

In 1994, Berenger [33, 34] developed a robust absorbing boundary called perfectly matched layer (PML). PML is an anisotropic and lossy medium with constitutive parameters which satisfy impedance matching condition independent of the frequency of the wave so that the outgoing wave can penetrate into PML without reflection. In order to absorb the wave, electric conductivity σ_e and magnetic conductivity σ_m are introduced into PML. Figure 2.4 shows interface of the computation space and PML.

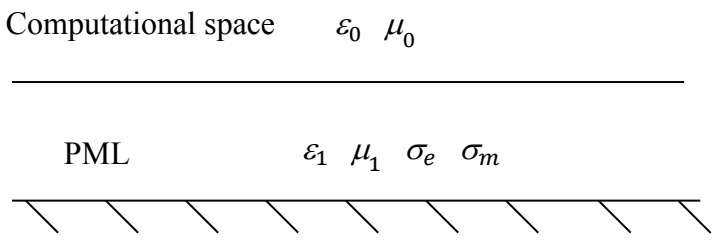

Figure 2.4 Interface of the computational space and PML. The medium in computational space is usually air, which is denoted by ε_0 and μ_0. The medium in PML is anisotropic and lossy, which is denoted by ε_1, μ_1, σ_e and σ_m.

To satisfy wave-impedance matching condition, the constitutive parameters in PML should be chosen as:

$$\varepsilon_1 = \varepsilon_0 \tag{2.9a}$$

$$\mu_1 = \mu_0 \tag{2.9b}$$

$$\frac{\sigma_e}{\varepsilon_0} = \frac{\sigma_m}{\mu_0} \tag{2.9c}$$

Due to the PML is anisotropic, the conductivities in PML are defined in different regions, take two-dimensional PML for example, the conductivities in different region are shown in the Figure 2.5:

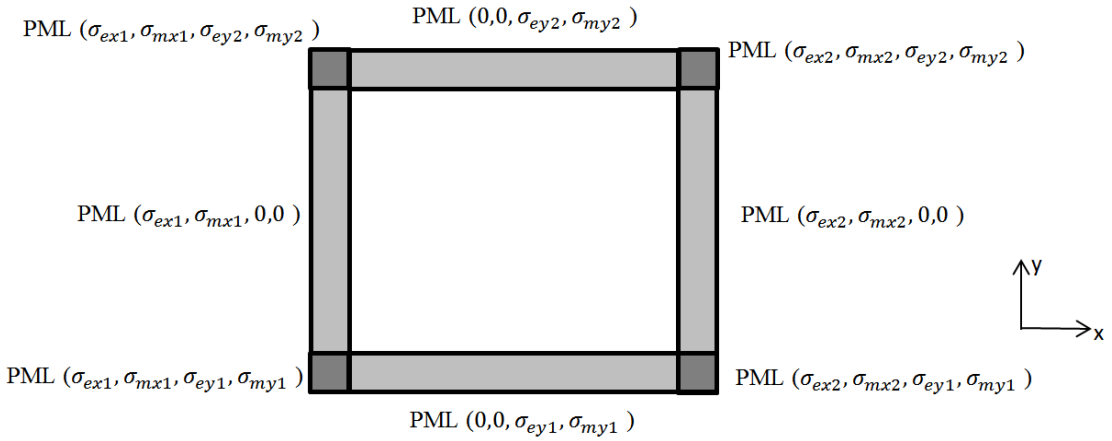

Figure 2.5 Conductivities definition in different regions of two-dimensional PML.

In Figure 2.5, σ_{ex1} is the electric conductivity in negative x direction, σ_{ex2} is the electric conductivity in positive x direction, σ_{mx1} is the magnetic conductivity in negative x direction, σ_{mx2} is the magnetic conductivity in positive x direction. Conductivities in y direction follow the similar donation. The conductivities should be gradually increasing distribution rather than uniform, the distribution function is:

$$\sigma(\rho) = \sigma_{max}(\frac{\rho}{\delta})^n \tag{2.10a}$$

$$\sigma_{max} = -\frac{(n+1)\varepsilon_0 cln(R(0))}{2\delta} \tag{2.10b}$$

where ρ is the distance from PML interface to the position of the field component, δ is the thickness of PML, n is the order of the distribution function, c is the wave velocity, $R(0)$ reflection coefficient.

In Berenger's implementation, each field component is split into two field components:

$$E_x\begin{Bmatrix}E_{xy}\\E_{xz}\end{Bmatrix} \quad E_y\begin{Bmatrix}E_{yx}\\E_{yz}\end{Bmatrix} \quad E_z\begin{Bmatrix}E_{zx}\\E_{zy}\end{Bmatrix} \quad H_x\begin{Bmatrix}H_{xy}\\H_{xz}\end{Bmatrix} \quad H_y\begin{Bmatrix}H_{yx}\\H_{yz}\end{Bmatrix} \quad H_z\begin{Bmatrix}H_{zx}\\H_{zy}\end{Bmatrix} \tag{2.11}$$

Now the Maxwell's equation in PML can be written as:

$$\varepsilon_0 \frac{\partial E_{xy}}{\partial t} + \sigma_{ey} E_{xy} = \frac{\partial (H_{zx}+H_{zy})}{\partial y} \tag{2.12a}$$

$$\varepsilon_0 \frac{\partial E_{xz}}{\partial t} + \sigma_{ez} E_{xz} = -\frac{\partial (H_{yx}+H_{yz})}{\partial z} \tag{2.12b}$$

$$\varepsilon_0 \frac{\partial E_{yx}}{\partial t} + \sigma_{ex} E_{yx} = -\frac{\partial (H_{zx}+H_{zy})}{\partial x} \tag{2.12c}$$

$$\varepsilon_0 \frac{\partial E_{yz}}{\partial t} + \sigma_{ez} E_{yz} = \frac{\partial (H_{xy}+H_{xz})}{\partial z} \tag{2.12d}$$

$$\varepsilon_0 \frac{\partial E_{zx}}{\partial t} + \sigma_{ex} E_{zx} = \frac{\partial (H_{yx}+H_{yz})}{\partial x} \tag{2.12e}$$

$$\varepsilon_0 \frac{\partial E_{zy}}{\partial t} + \sigma_{ey} E_{zy} = -\frac{\partial (H_{xy}+H_{xz})}{\partial y} \tag{2.12f}$$

$$\mu_0 \frac{\partial H_{xy}}{\partial t} + \sigma_{my} H_{xy} = -\frac{\partial (E_{zx}+E_{zy})}{\partial y} \tag{2.12g}$$

$$\mu_0 \frac{\partial H_{xz}}{\partial t} + \sigma_{mz} H_{xz} = \frac{\partial (E_{yx}+E_{yz})}{\partial z} \tag{2.12h}$$

$$\mu_0 \frac{\partial H_{yx}}{\partial t} + \sigma_{mx} H_{yx} = \frac{\partial (E_{zx}+E_{zy})}{\partial x} \tag{2.12i}$$

$$\mu_0 \frac{\partial H_{yz}}{\partial t} + \sigma_{mz} H_{yz} = -\frac{\partial (E_{xy}+E_{xz})}{\partial z} \tag{2.12j}$$

$$\mu_0 \frac{\partial H_{zx}}{\partial t} + \sigma_{mx} H_{zx} = -\frac{\partial (E_{yz}+E_{yz})}{\partial x} \tag{2.12k}$$

$$\mu_0 \frac{\partial H_{zy}}{\partial t} + \sigma_{my} H_{zy} = \frac{\partial (E_{xy}+E_{xz})}{\partial y} \tag{2.12l}$$

Approximating the derivative in (2.12a)-(2.12l) by finite difference, we can get the field updating equations in PML. For example, the updating equations for electric field in x direction are:

$$E_{xy}^{n+1}(i,j,k) = \frac{2\varepsilon_0 - \sigma_{ey}\Delta t}{2\varepsilon_0 + \sigma_{ey}\Delta t} E_{xy}^{n}(i,j,k) + \frac{2\Delta t}{(2\varepsilon_0 + \sigma_{ey}\Delta t)\Delta y}\left(H_z^{n+\frac{1}{2}}(i,j,k) - H_z^{n+\frac{1}{2}}(i,j-1,k)\right) \tag{2.13a}$$

$$E_{xz}^{n+1}(i,j,k) = \frac{2\varepsilon_0 - \sigma_{ez}\Delta t}{2\varepsilon_0 + \sigma_{ez}\Delta t} E_{xz}^{n}(i,j,k) - \frac{2\Delta t}{(2\varepsilon_0 + \sigma_{ez}\Delta t)\Delta z}\left(H_y^{n+\frac{1}{2}}(i,j,k) - H_y^{n+\frac{1}{2}}(i,j,k-1)\right) \tag{2.13b}$$

The updating equations for magnetic field in x direction are:

$$H_{xy}^{n+\frac{1}{2}}(i,j,k) = \frac{2\mu_0 - \sigma_{my}\Delta t}{2\mu_0 + \sigma_{my}\Delta t} H_{xy}^{n-\frac{1}{2}}(i,j,k) - \frac{2\Delta t}{(2\mu_0 + \sigma_{my}\Delta t)\Delta y}\left(E_z^{n}(i,j+1,k) - E_z^{n}(i,j,k)\right) \tag{2.14a}$$

$$H_{xz}^{n+\frac{1}{2}}(i,j,k) = \frac{2\mu_0 - \sigma_{mz}\Delta t}{2\mu_0 + \sigma_{mz}\Delta t} H_{xz}^{n-\frac{1}{2}}(i,j,k) + \frac{2\Delta t}{(2\mu_0 + \sigma_{mz}\Delta t)\Delta z}(E_y^n(i,j,k+1) - E_y^n(i,j,k)) \quad (2.14b)$$

Updating equations for other field components can be derived in similar manner.

A point source is placed at the center of the computational domain, the electromagnetic wave will propagate from the center to outside. In this experiment, the cell size is 2mm, the thickness of PML is 10 cells, and the order of the distribution function is 4. Figure 2.6(a) shows the field distribution when there is no PML surrounding the computational domain. We can see the wave is reflected back and corrupts the domain. In contrast, Figure 2.6(b) shows the field distribution with PML absorbing boundary. In this case, outgoing wave is absorbed completely and there is no reflected wave.

To investigate the reflection error of PML quantitatively, we record the field at an observation point which is 10 cells far away from the PML interface, and compare it with reference value which is obtained by removing PML and setting the computation domain large enough so that the reflection from the boundary can be isolated. Then the reflection error can be computed (2.15):

$$R = 20log_{10}(\frac{|P_{PML}(t) - P_{ref}(t)|}{max|P_{ref}(t)|}) \quad (2.15)$$

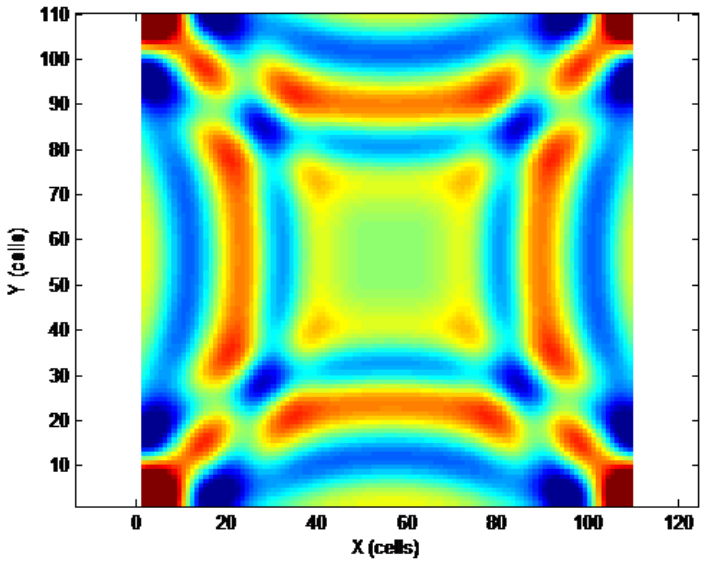

(a)

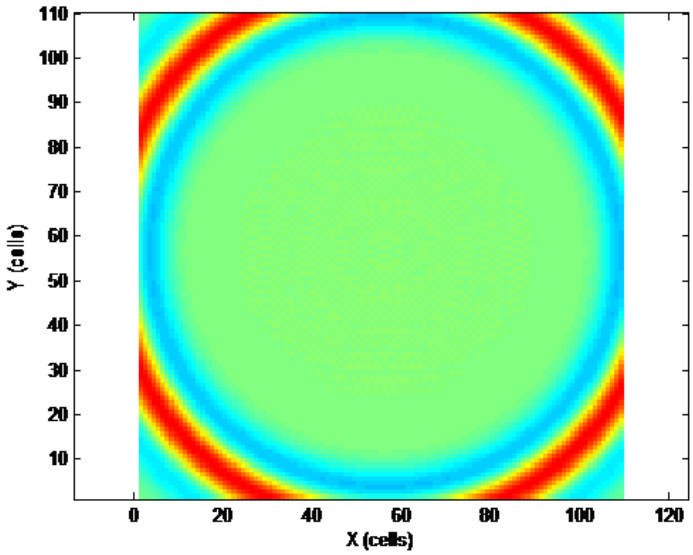

(b)

Figure 2.6 (a) Field distribution without PML. The wave is reflected back and corrupts the computational domain; (b) Field distribution with PML, the outgoing wave is absorbed completely. Here the spatial resolution is 2mm, the thickness of PML is 10 cells, and the order of the distribution function is 4.

Figure 2.7(a) shows the time-domain signal at the observation point with PML and the reference signal at the same point. These two signals coincide with each other very well. Figure 2.7(b) shows the reflection error. The maximum reflection error is about -64dB.

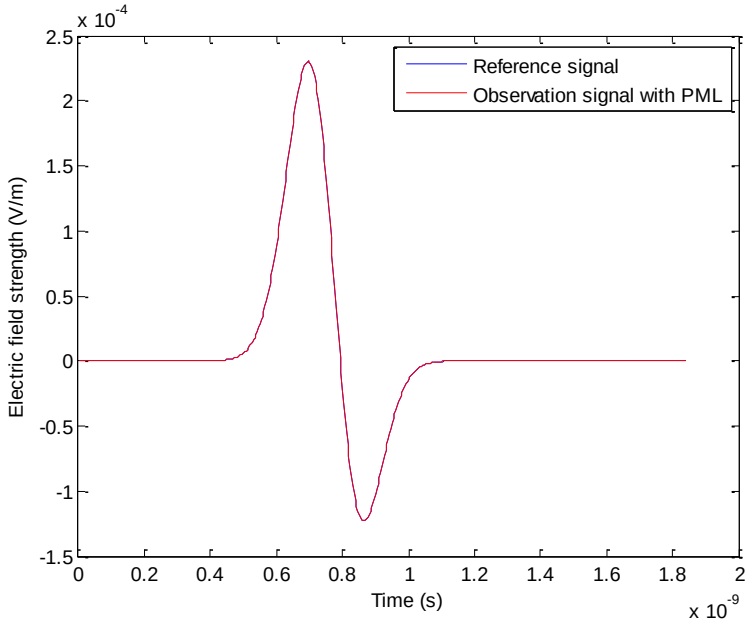

(a)

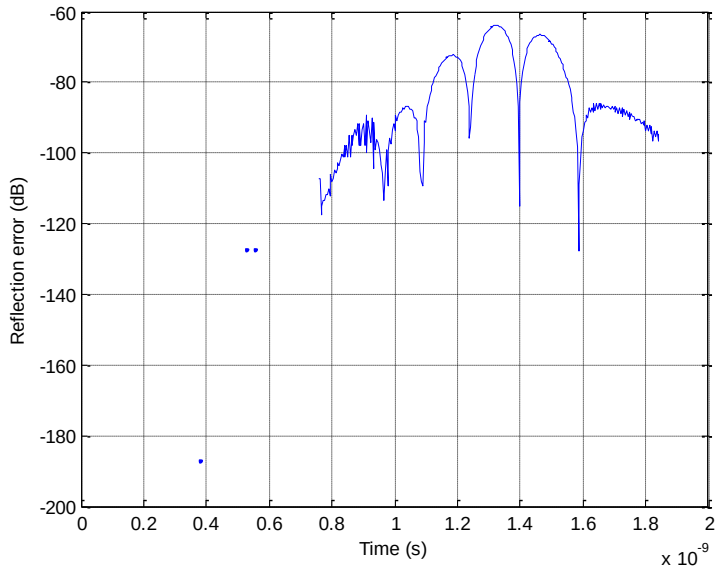

(b)

Figure 2.7 (a) Comparison of reference signal and observation signal with PML, they coincide with each other very well; (b) Reflection error of PML. The observation point is 10 cells far away from the PML interface. All simulation settings are the same as Figure 2.6.

Figure 2.8(a) shows the relation between the conductivity distribution function order and reflection error. We can see the reflection error increases as the order decreases. Figure 2.8(b) shows the effect of PML thickness. Although 6 cells of thickness has worse overall performance than 10 and 14 cells, the reflection error is less than -60dB everywhere. So the thickness of PML should not be less than 6 cells.

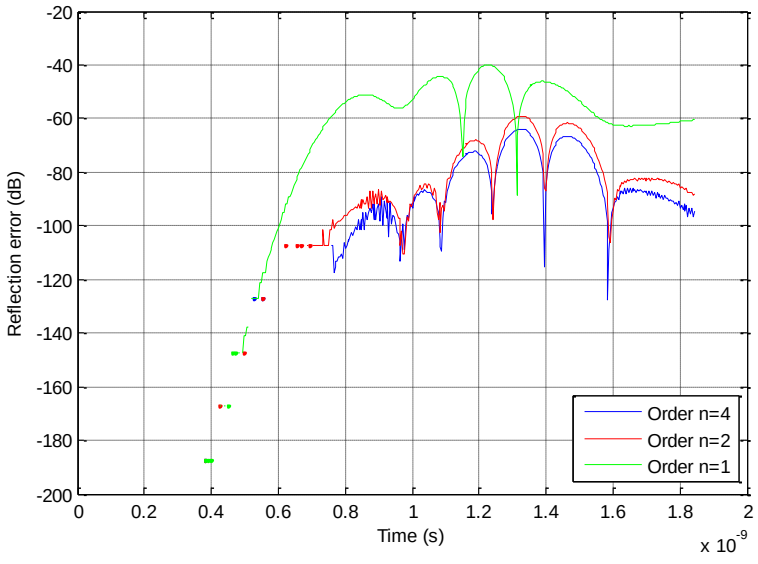

(a)

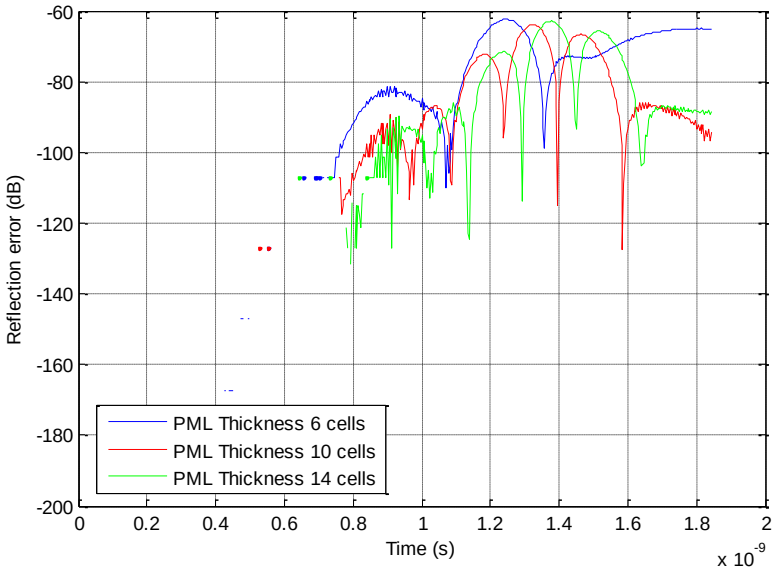

(b)

Figure 2.8 (a) Effect of the conductivity distribution function order on reflection error. The error decreases as the order increases; (b) Effect of PML thickness on reflection error. Other simulation settings are the same as Figure 2.6 and 2.7.

2.4 Time step and convergence

FDTD is an explicit iterative scheme, it is conditionally stable. This condition is called Courant-Freidrichs-Lewy (CFL) stability condition which requires the time step Δt has an upper bound relative to spatial resolution Δx, Δy and Δz:

$$\Delta t \leq \frac{1}{c\sqrt{\frac{1}{(\Delta x)^2}+\frac{1}{(\Delta y)^2}+\frac{1}{(\Delta z)^2}}} \tag{2.16}$$

In other words, if we define CFL number (CFLN) as:

$$CFLN = c\Delta t\sqrt{\frac{1}{(\Delta x)^2}+\frac{1}{(\Delta y)^2}+\frac{1}{(\Delta z)^2}} \tag{2.17}$$

the stability condition is:

$$CFLN \leq 1 \tag{2.18}$$

If CFL condition is not satisfied, the algorithm will be divergent. This case is shown in Figure 2.9, the fields grow to infinity after several time steps.

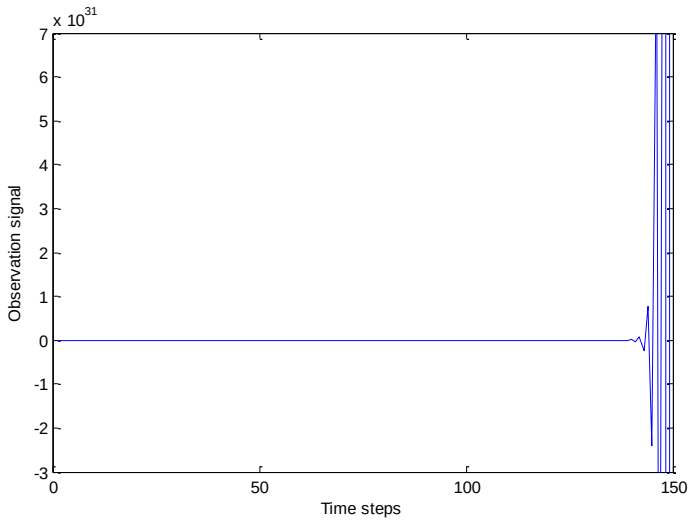

Figure 2.9 The time signal of one observation point when CFLN>1. The algorithm diverges in this case.

To obtain accurate results, the FDTD must continue running until it reaches a steady state. If the excitation signal is wideband signal, for example Gaussian derivative signal shown in Figure 2.10(a) steady state means the output observation signal decays to zero (or below a predefined threshold) (Figure 2.10(b)). If the excitation signal is single sinusoid signal shown in Figure 2.10(c), the steady state means the magnitude of the output signal doesn't change with time (or varies below a predefined threshold) (Figure 2.10(d)).

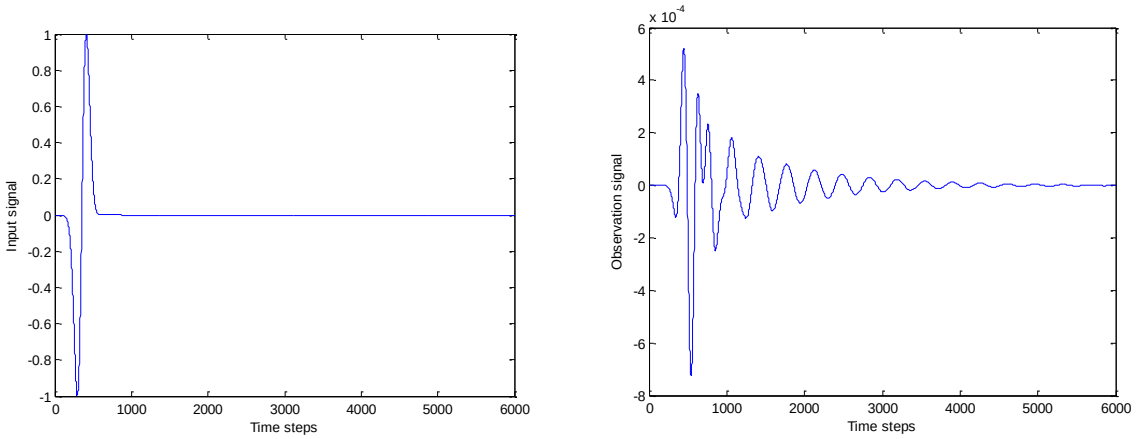

(a) (b)

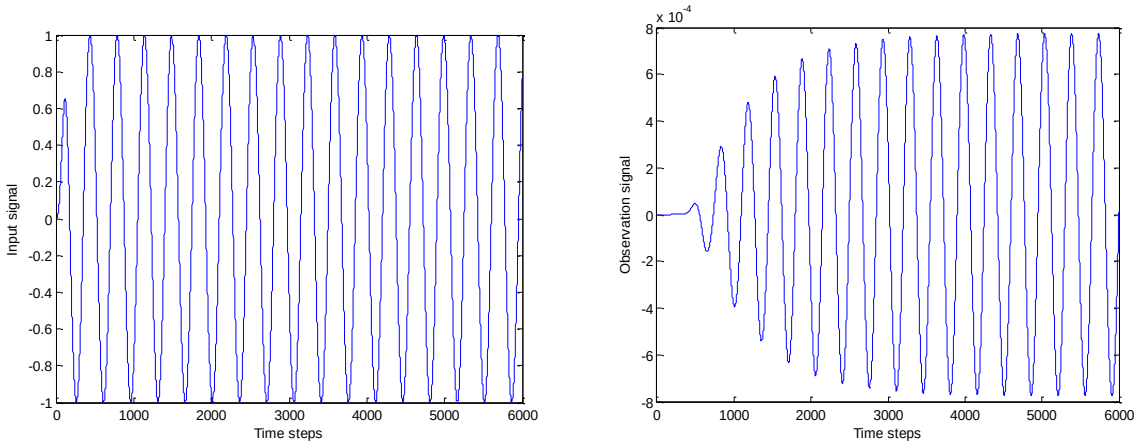

(c) (d)

Figure 2.10 (a) Gaussian derivative excitation signal; (b) Steady state of Gaussian derivative signal. The signal decays to zero gradually; (c) Sinusoid excitation signal; (d) Steady state of sinusoid signal. The magnitude of the output signal doesn't change with time.

2.5 Spatial resolution and numerical dispersion

When the dimension of the geometry is larger than wavelength, which is electrically large problem, the cell size is limited by wavelength. To get an accurate result, the cell size should be no larger than λ/10, where λ is the wavelength. Conversely, when the dimension of the object is smaller than wavelength, which is electrically small problem, the cell size is limited by the model. It should be small enough to distinguish the finest structure of geometry.

The main error of FDTD method is the numerical dispersion which arises due to the discretization. The numerical dispersion relation can be derived by Fourier analysis [31]:

$$sin^2\left(\frac{\omega\Delta t}{2}\right) = \left(\frac{c\Delta t}{\Delta x}\right)^2 sin^2\left(\frac{k_x\Delta x}{2}\right) + \left(\frac{c\Delta t}{\Delta y}\right)^2 sin^2\left(\frac{k_y\Delta y}{2}\right) + \left(\frac{c\Delta t}{\Delta z}\right)^2 sin^2\left(\frac{k_z\Delta z}{2}\right) \qquad (2.19)$$

where ω is angular frequency, c is wave velocity, k is wave number with three components k_x, k_y and k_z. From (2.19), the numerical wave velocity can be written as:

$$v = \frac{2}{k\Delta t} sin^{-1}\left[c\Delta t \sqrt{\frac{1}{(\Delta x)^2} sin^2\left(\frac{ksin\theta cos\varphi\Delta x}{2}\right) + \frac{1}{(\Delta y)^2} sin^2\left(\frac{ksin\theta sin\varphi\Delta y}{2}\right) + \frac{1}{(\Delta z)^2} sin^2\left(\frac{kcos\theta\Delta z}{2}\right)}\right] \qquad (2.20)$$

where θ is the zenith angle and φ is the azimuth angle. Figure 2.11 shows the relative velocity v/c as a function of azimuth angle, cell size and CFLN. In Figure 2.11, $\Delta x = \Delta y = \Delta z = \Delta$, $\theta = 90^{\circ}$. We can see that the numerical velocity depends on propagation angle, this is called numerical anisotropy. In Figure 2.11(a) CFLN=0.6, the anisotropy is reduced with decreasing cell size. In Figure 2.11(b) $\Delta = \lambda/20$, numerical velocity increases as CFLN increases.

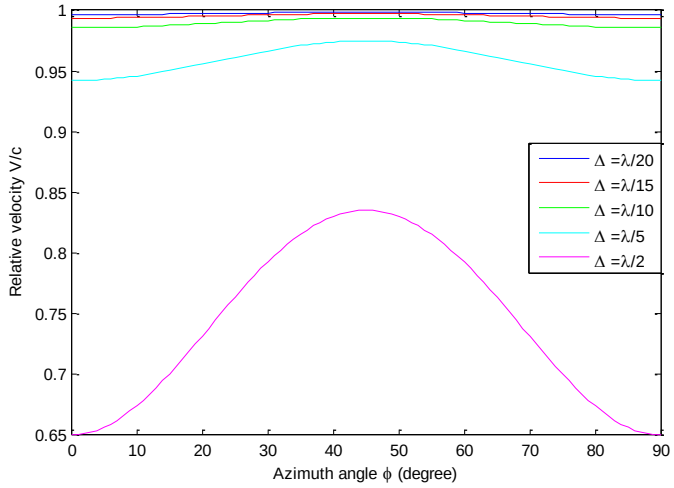

(a)

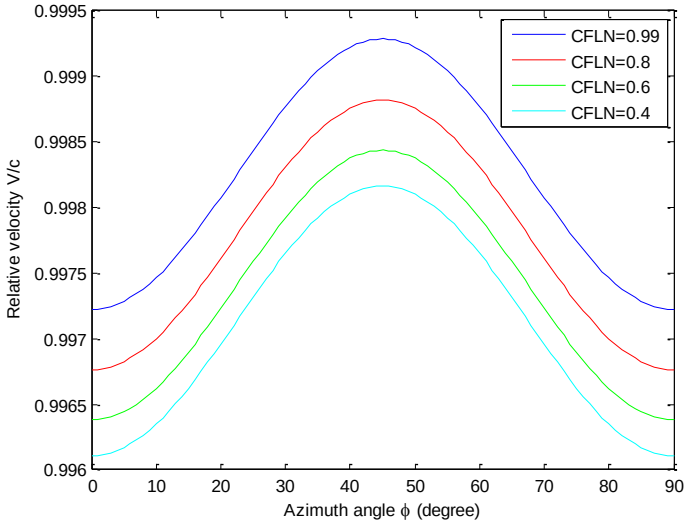

(b)

Figure 2.11 (a) Relative wave velocity as a function of azimuth angle for varied cell size. Zenith angle is 90 degree, CFLN=0.6; (b) Relative wave velocity as a function of azimuth angle for varied CFLN. Zenith angle is 90 degree, $\Delta = \lambda/20$.

2.6 Wave sources

2.6.1 Hard source

Hard source is realized simply by assigning a waveform to specific electric or magnetic field components at single or multiple points [31]. For example, a sinusoid waveform is assigned to $E_z(i,j,k)$ can be written as:

$$E_z^n(i,j,k) = A\sin(\omega n\Delta t) \tag{2.21}$$

2.6.2 Voltage and current sources

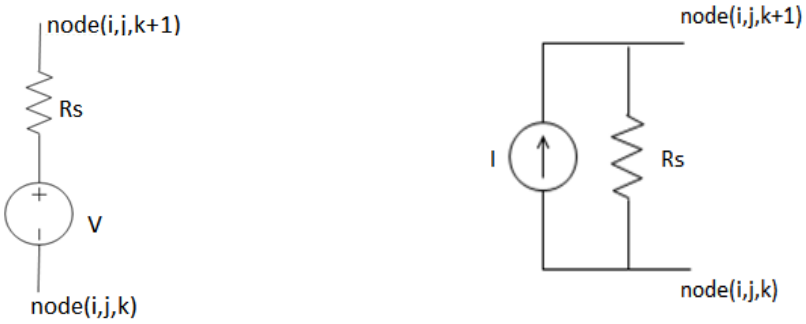

(a) (b)

Figure 2.12 (a) Voltage source with series resistor. The voltage source is along z direction; (b) Current source with parallel resistor. The current is along z direction.

The voltage and current sources are shown in Figure 2.12(a) and (b). The updating equations for voltage and current sources in Figure 2.12 are (2.22) and (2.23) respectively [30]. The updating equations for sources oriented in other direction can be derived in similar way.

$$\begin{aligned} E_z^{n+1}(i,j,k) = {} & \frac{2\varepsilon(i,j,k)R_s\Delta x\Delta y-\Delta t\Delta z}{2\varepsilon(i,j,k)R_s\Delta x\Delta y+\Delta t\Delta z}E_z^n(i,j,k) + \\ & \frac{2\Delta tR_s\Delta x\Delta y}{(2\varepsilon(i,j,k)R_s\Delta x\Delta y+\Delta t\Delta z)\Delta x}\left(H_y^{n+\frac{1}{2}}(i,j,k) - H_y^{n+\frac{1}{2}}(i-1,j,k)\right) \\ & - \frac{2\Delta tR_s\Delta x\Delta y}{(2\varepsilon(i,j,k)R_s\Delta x\Delta y+\Delta t\Delta z)\Delta y}\left(H_x^{n+\frac{1}{2}}(i,j,k) - H_x^{n+\frac{1}{2}}(i,j-1,k)\right) \\ & - \frac{2\Delta t}{(2\varepsilon(i,j,k)R_s\Delta x\Delta y+\Delta t\Delta z)}V^{n+\frac{1}{2}}(i,j,k) \end{aligned} \tag{2.22}$$

$$\begin{aligned} E_z^{n+1}(i,j,k) = {} & \frac{2\varepsilon(i,j,k)R_s\Delta x\Delta y-\Delta t\Delta z}{2\varepsilon(i,j,k)R_s\Delta x\Delta y+\Delta t\Delta z}E_z^n(i,j,k) + \\ & \frac{2\Delta tR_s\Delta x\Delta y}{(2\varepsilon(i,j,k)R_s\Delta x\Delta y+\Delta t\Delta z)\Delta x}\left(H_y^{n+\frac{1}{2}}(i,j,k) - H_y^{n+\frac{1}{2}}(i-1,j,k)\right) \end{aligned}$$

$$-\frac{2\Delta t R_s \Delta x \Delta y}{(2\varepsilon(i,j,k)R_s\Delta x\Delta y+\Delta t\Delta z)\Delta y}\left(H_x^{n+\frac{1}{2}}(i,j,k)-H_x^{n+\frac{1}{2}}(i,j-1,k)\right)$$

$$-\frac{2\Delta t R_s}{(2\varepsilon(i,j,k)R_s\Delta x\Delta y+\Delta t\Delta z)}I^{n+\frac{1}{2}}(i,j,k) \tag{2.22}$$

2.6.3 Plane wave source

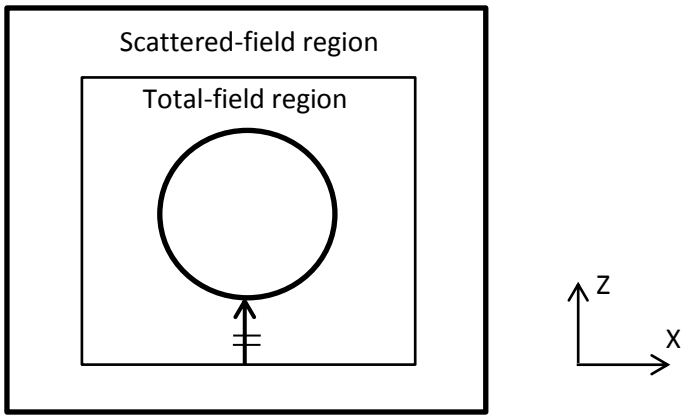

Figure 2.13 Total-field and scattered-field regions in FDTD space with a plane wave incidents alone z direction.

To simulate scattering problem, we need to implement plane wave in FDTD. The total-field scattered-field (TF/SF) boundary is often used to introduce plane waves. As shown in the Figure 2.13, the space is divided into two distinct regions: the inner region is the total-field region and the outer one is the scattered-field region. The plane wave is launched on the TF/SF boundary by setting the fields on the both sides of the boundary to be discontinuous by the value of the incident field. This can be implemented simply by adding a correction term in the field updating equations at the grids around the TF/SF boundary. A detailed description of TF/SF formulations can be found in [29] and [31], here we just list the correction terms of each field component in Table 2.2-2.4.

Table 2.2 TF/SF algorithm correction terms at –X and +X interface.

-X		+X	
Total-field		Total-field	
$E_y^{n+1}(i,j,k)$	$\frac{dt}{\varepsilon dx}H_{z\,inc}^{n+\frac{1}{2}}(i-1,j,k)$	$E_y^{n+1}(i,j,k)$	$-\frac{dt}{\varepsilon dx}H_{z\,inc}^{n+\frac{1}{2}}(i,j,k)$
$E_z^{n+1}(i,j,k)$	$-\frac{dt}{\varepsilon dx}H_{y\,inc}^{n+\frac{1}{2}}(i-1,j,k)$	$E_z^{n+1}(i,j,k)$	$\frac{dt}{\varepsilon dx}H_{y\,inc}^{n+\frac{1}{2}}(i,j,k)$

Scattered-field		Scattered-field	
$H_y^{n+\frac{1}{2}}(i-1,j,k)$	$-\frac{dt}{\mu dx}E_{z\,inc}^{n}(i,j,k)$	$H_y^{n+\frac{1}{2}}(i,j,k)$	$\frac{dt}{\mu dx}E_{z\,inc}^{n}(i,j,k)$
$H_z^{n+\frac{1}{2}}(i-1,j,k)$	$\frac{dt}{\mu dx}E_{y\,inc}^{n}(i,j,k)$	$H_z^{n+\frac{1}{2}}(i,j,k)$	$-\frac{dt}{\mu dx}E_{y\,inc}^{n}(i,j,k)$

Table 2.3 TF/SF algorithm correction terms at –Y and +Y interface.

-Y		+Y	
Total-field		Total-field	
$E_x^{n+1}(i,j,k)$	$-\frac{dt}{\varepsilon dy}H_{z\,inc}^{n+\frac{1}{2}}(i,j-1,k)$	$E_x^{n+1}(i,j,k)$	$\frac{dt}{\varepsilon dy}H_{z\,inc}^{n+\frac{1}{2}}(i,j,k)$
$E_z^{n+1}(i,j,k)$	$\frac{dt}{\varepsilon dy}H_{x\,inc}^{n+\frac{1}{2}}(i,j-1,k)$	$E_z^{n+1}(i,j,k)$	$-\frac{dt}{\varepsilon dy}H_{x\,inc}^{n+\frac{1}{2}}(i,j,k)$
Scattered-field		Scattered-field	
$H_x^{n+\frac{1}{2}}(i,j-1,k)$	$\frac{dt}{\mu dy}E_{z\,inc}^{n}(i,j,k)$	$H_x^{n+\frac{1}{2}}(i,j,k)$	$-\frac{dt}{\mu dy}E_{z\,inc}^{n}(i,j,k)$
$H_z^{n+\frac{1}{2}}(i,j-1,k)$	$-\frac{dt}{\mu dy}E_{x\,inc}^{n}(i,j,k)$	$H_z^{n+\frac{1}{2}}(i,j,k)$	$\frac{dt}{\mu dy}E_{x\,inc}^{n}(i,j,k)$

Table 2.4 TF/SF algorithm correction terms at –Z and +Z interface.

-Z		+Z	
Total-field		Total-field	
$E_x^{n+1}(i,j,k)$	$\frac{dt}{\varepsilon dz}H_{y\,inc}^{n+\frac{1}{2}}(i,j,k-1)$	$E_x^{n+1}(i,j,k)$	$-\frac{dt}{\varepsilon dz}H_{y\,inc}^{n+\frac{1}{2}}(i,j,k)$
$E_y^{n+1}(i,j,k)$	$-\frac{dt}{\varepsilon dz}H_{x\,inc}^{n+\frac{1}{2}}(i,j,k-1)$	$E_y^{n+1}(i,j,k)$	$\frac{dt}{\varepsilon dz}H_{x\,inc}^{n+\frac{1}{2}}(i,j,k)$
Scattered-field		Scattered-field	
$H_x^{n+\frac{1}{2}}(i,j,k-1)$	$-\frac{dt}{\mu dz}E_{y\,inc}^{n}(i,j,k)$	$H_x^{n+\frac{1}{2}}(i,j,k)$	$\frac{dt}{\mu dz}E_{y\,inc}^{n}(i,j,k)$
$H_y^{n+\frac{1}{2}}(i,j,k-1)$	$\frac{dt}{\mu dz}E_{x\,inc}^{n}(i,j,k)$	$H_y^{n+\frac{1}{2}}(i,j,k)$	$-\frac{dt}{\mu dz}E_{x\,inc}^{n}(i,j,k)$

2.7 Validation

To validate the FDTD program, the scattering by a dielectric sphere is analyzed. The problem is showing in Figure 2.14. The diameter of the sphere is 160mm, the relative permittivity ε_r is 36 and the conductivity σ is 0.657. The incident plane wave travels along z axis, the E field is polarized in x direction.

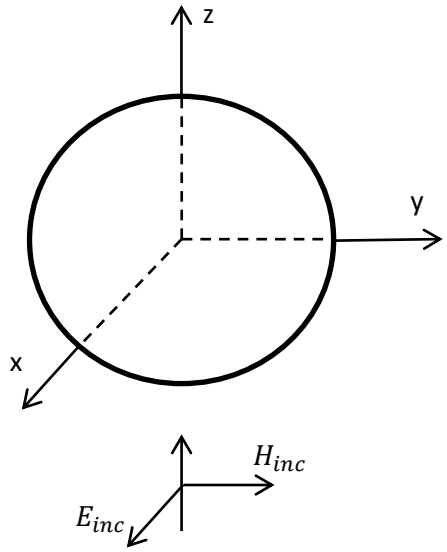

Figure 2.14 Scattering by a dielectric sphere. The diameter of the sphere is 160mm, relative permittivity is 36, and conductivity is 0.657. The incident plane wave travels along z axis, the E field is polarized in x direction.

According to reference [35], the total field inside the dielectric sphere can be written in the form of vector potentials as:

$$A_r = E_0 \frac{\cos\varphi}{\omega} \sum_{n=1}^{\infty} d_n \hat{J}_n(\dot{\beta}_d r) P_n^{(1)}(\cos\theta) \tag{2.23}$$

$$F_r = E_0 \frac{\sin\varphi}{\dot{\omega}\eta} \sum_{n=1}^{\infty} e_n \hat{J}_n(\dot{\beta}_d r) P_n^{(1)}(\cos\theta) \tag{2.24}$$

The coefficients d_n and e_n can be derived by boundary condition which requires the tangential electric and magnetic fields on the surface of the sphere to be continuous. They can be written as:

$$d_n = -j \frac{\dot{\mu}_r \sqrt{\dot{\varepsilon}_r}}{\sqrt{\dot{\varepsilon}_r}\, \hat{H}_n^{(2)'}(\beta_0 a) \hat{J}_n(\dot{\beta}_d a) - \sqrt{\dot{\mu}_r}\, \hat{H}_n^{(2)}(\beta_0 a) \hat{J}_n'(\dot{\beta}_d a)} a_n \tag{2.25}$$

$$e_n = j\frac{\dot{\mu}_r\sqrt{\dot{\varepsilon}_r}}{\sqrt{\dot{\varepsilon}_r}\,\hat{H}_n^{(2)}(\beta_0 a)\,\hat{J}_n'(\dot{\beta}_d a)-\sqrt{\dot{\mu}_r}\,\hat{H}_n^{(2)'}(\beta_0 a)\,\hat{J}_n(\dot{\beta}_d a)}a_n \tag{2.26}$$

$$a_n = j^{-n}\frac{2n+1}{n(n+1)} \tag{2.27}$$

In (2.25) and (2.26):

$$\dot{\beta}_d = \omega\sqrt{\mu\dot{\varepsilon}_d} \tag{2.28}$$

$$\beta_0 = \omega\sqrt{\mu\varepsilon_0} \tag{2.29}$$

$$\dot{\varepsilon}_d = \varepsilon_d - j\frac{\sigma}{\omega} \tag{2.30}$$

$$\dot{\varepsilon}_r = \varepsilon_r - j\frac{\sigma}{\varepsilon_0\omega} \tag{2.31}$$

$$\dot{\eta} = \sqrt{\frac{\mu}{\dot{\varepsilon}}} \tag{2.32}$$

The electric field in the sphere calculated by:

$$E_r = \frac{1}{j\omega\mu\varepsilon}(\frac{\partial^2}{\partial r^2}+\beta^2)A_r \tag{2.33}$$

$$E_\theta = \frac{1}{j\omega\mu\varepsilon}\frac{1}{r}\frac{\partial^2 A_r}{\partial r\partial\theta}-\frac{1}{\varepsilon}\frac{1}{r\sin\theta}\frac{\partial F_r}{\partial\varphi} \tag{2.34}$$

$$E_\varphi = \frac{1}{j\omega\mu\varepsilon}\frac{1}{r\sin\theta}\frac{\partial^2 A_r}{\partial r\partial\varphi}-\frac{1}{\varepsilon}\frac{1}{r}\frac{\partial F_r}{\partial\theta} \tag{2.35}$$

Substitute (2.23)-(2.27) into (2.33-2.35), we can get:

$$\begin{aligned} E_r &= \frac{1}{j\omega\dot{\mu}\dot{\varepsilon}}E_0\frac{\cos\varphi}{\omega}\sum_{n=1}^{\infty}d_n(\frac{\partial^2}{\partial r^2}+\beta^2)\hat{J}_n(\dot{\beta}_d r)P_n^{(1)}(\cos\theta) \\ &= -j\frac{E_0\cos\varphi}{\dot{\beta}_d^2 r^2}\sum_{n=1}^{\infty}n(n+1)d_n\hat{J}_n(\dot{\beta}_d r)P_n^{(1)}(\cos\theta) \end{aligned} \tag{2.36}$$

$$
\begin{aligned}
E_\theta &= \frac{1}{j\omega\mu\dot{\varepsilon}}\frac{1}{r}E_0\frac{\cos\varphi}{\omega}\sum_{n=1}^{\infty}d_n\frac{\partial}{\partial r}(\hat{J}_n(\dot{\beta}_d r))\frac{\partial}{\partial\theta}(P_n^{(1)}(\cos\theta)) \\
&\quad -\frac{1}{\dot{\varepsilon}}\frac{1}{r\sin\theta}\frac{E_0}{\omega\dot{\eta}}\frac{\partial}{\partial\varphi}(\sin\varphi)\sum_{n=1}^{\infty}e_n\hat{J}_n(\dot{\beta}_d r)P_n^{(1)}(\cos\theta) \\
&= \frac{jE_0\cos\varphi\sin\theta}{\dot{\beta}_d r}\sum_{n=1}^{\infty}d_n\hat{J}_d'(\dot{\beta}_d r)P_n^{(1)'}(\cos\theta)-\frac{E_0\cos\varphi}{\dot{\beta}_d r\sin\theta}\sum_{n=1}^{\infty}e_n\hat{J}_n(\dot{\beta}_d r)P_n^{(1)}(\cos\theta)
\end{aligned}
\tag{2.37}
$$

$$
\begin{aligned}
E_\varphi &= \frac{1}{j\omega\mu\dot{\varepsilon}}\frac{1}{r\sin\theta}\frac{E_0}{\omega}\frac{\partial}{\partial\varphi}(\cos\varphi)\sum_{n=1}^{\infty}d_n\frac{\partial}{\partial r}(\hat{J}_n(\dot{\beta}_d r))P_n^{(1)}(\cos\theta) \\
&\quad +\frac{1}{\dot{\varepsilon}r}E_0\frac{\sin\varphi}{\omega\dot{\eta}}\sum_{n=1}^{\infty}e_n\hat{J}_n(\dot{\beta}_d r)\frac{\partial}{\partial\theta}(P_n^{(1)}(\cos\theta)) \\
&= \frac{jE_0\sin\varphi}{\dot{\beta}_d r\sin\theta}\sum_{n=1}^{\infty}d_n\hat{J}_n'(\dot{\beta}_d r)P_n^{(1)}(\cos\theta)-\frac{E_0\sin\varphi\sin\theta}{\dot{\beta}_d r}\sum_{n=1}^{\infty}e_n\hat{J}_n(\dot{\beta}_d r)P_n^{(1)'}(\cos\theta)
\end{aligned}
\tag{2.38}
$$

We implement (2.36)-(2.38) with Matlab, the infinite series can be approximated by first ten terms given that the truncation error is less than 0.1%. Then we simulate the same problem by FDTD with 2mm cell size. The thickness of PML is 10 cells and the order is 4. The plane wave is launched by TF/SF boundary described in 2.6.3. The total electric fields in the sphere at three different frequencies are shown in Figure 2.15-2.17, the unit of electric field is V/m. In Figure 2.15 the frequency is 100MHz, in Figure 2.16 the frequency is 300MHz and in Figure 2.17, the frequency is 1GHz. From these figures, we can see that the FDTD results agree with analytical solution very well at each frequency. The results verify the validity of our program.

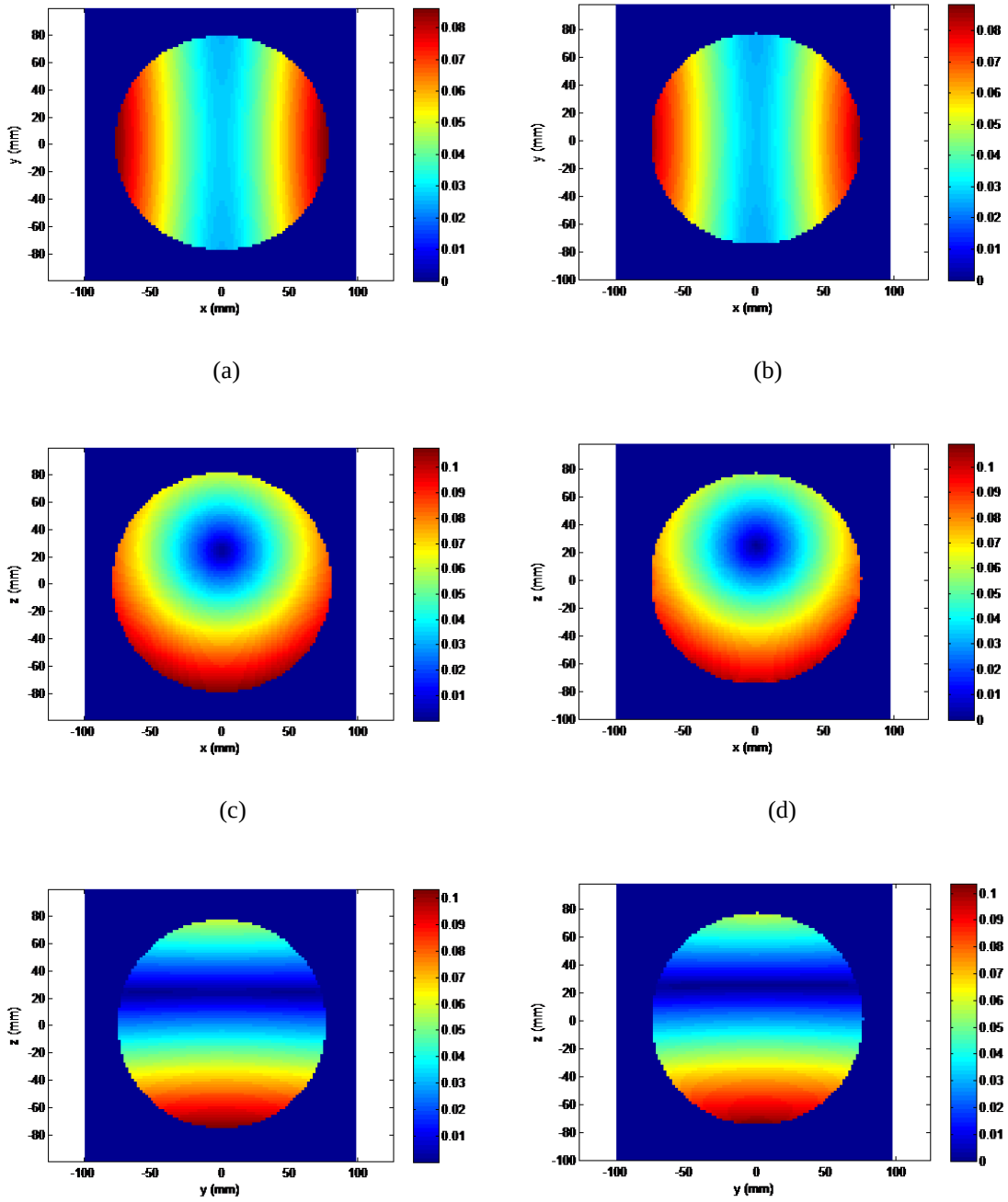

(a) (b)

(c) (d)

(e) (f)

Figure 2.15 The electric field distribution in a dielectric sphere laminated by a plane wave at 100MHz. (a) Analytical solution in XY plane ; (b) FDTD result in XY plane; (c) Analytical solution in XZ plane ; (d) FDTD result in XZ plane; (e) Analytical solution in YZ plane ; (f) FDTD result in YZ plane. The unit is V/m.

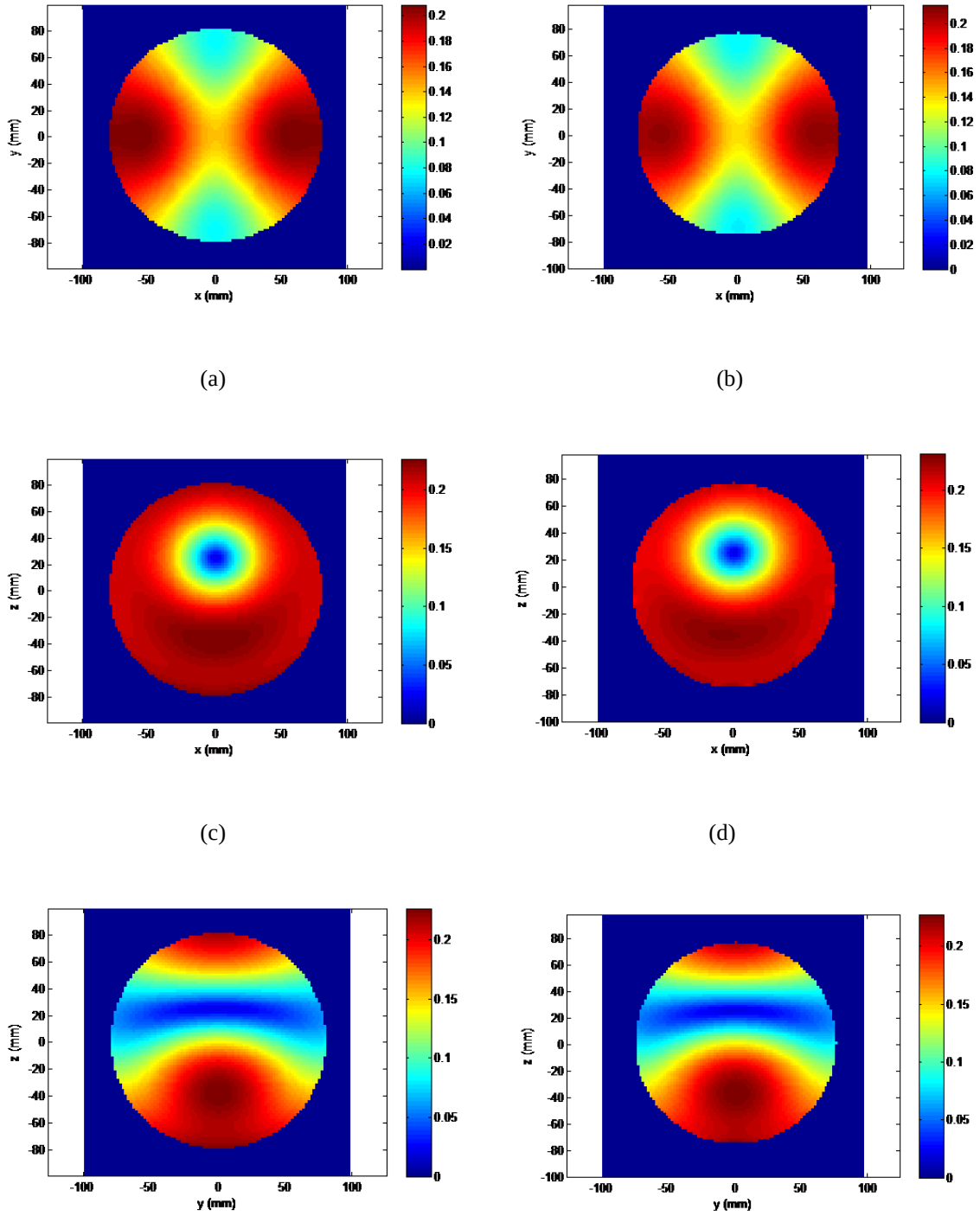

(a) (b)

(c) (d)

(e) (f)

Figure 2.16 The electric field distribution in a dielectric sphere laminated by a plane wave at 300MHz. (a) Analytical solution in XY plane ; (b) FDTD result in XY plane; (c) Analytical solution in XZ plane ; (d) FDTD result in XZ plane; (e) Analytical solution in YZ plane ; (d) FDTD result in YZ plane. The unit is V/m.

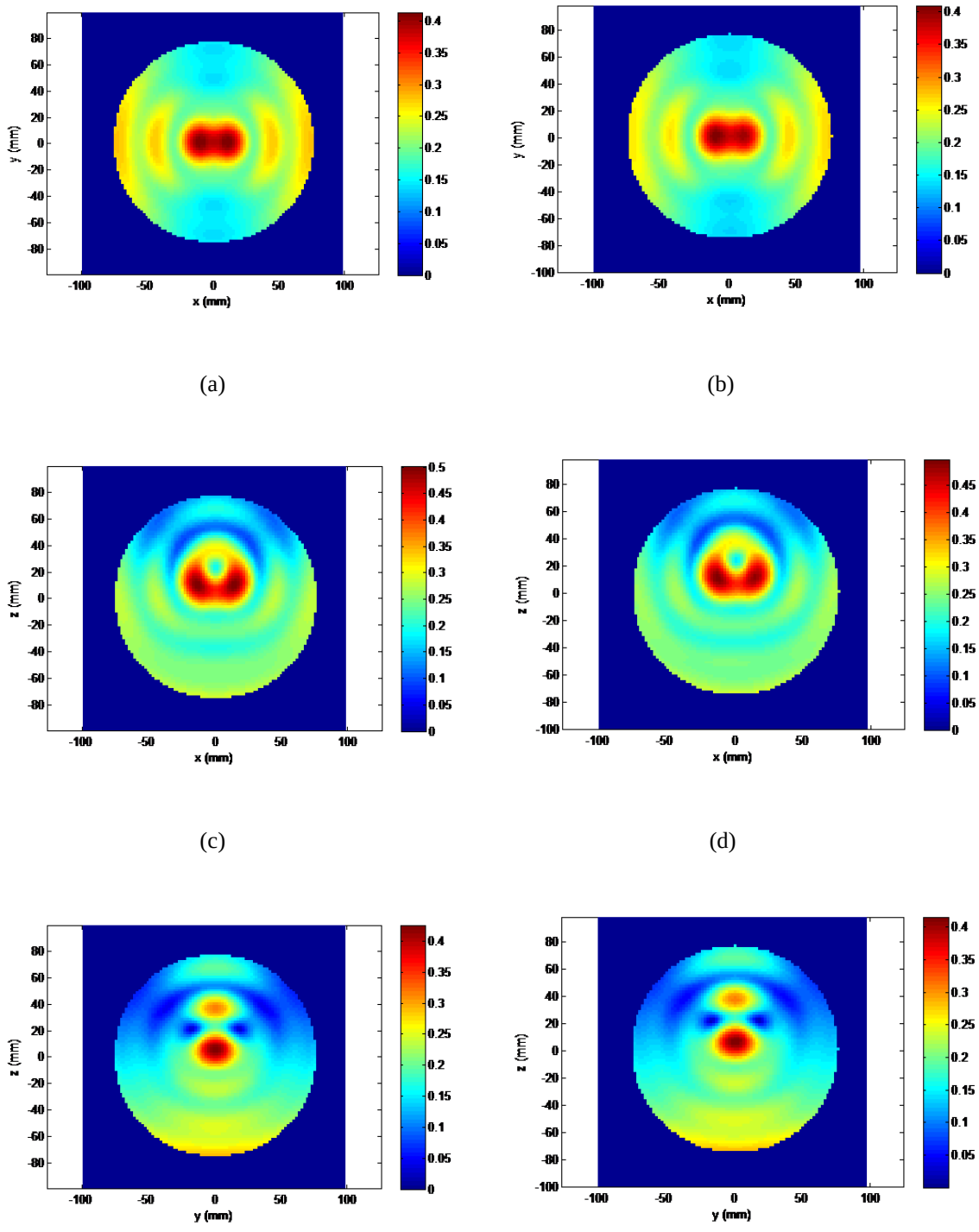

(a) (b)

(c) (d)

(e) (f)

Figure 2.17 The electric field distribution in a dielectric sphere laminated by a plane wave at 1GHz. (a) Analytical solution in XY plane ; (b) FDTD result in XY plane; (c) Analytical solution in XZ plane ; (d) FDTD result in XZ plane; (e) Analytical solution in YZ plane ; (d) FDTD result in YZ plane. The unit is V/m.

Chapter 3 GPU Acceleration of FDTD

FDTD is the algorithm which utilizes volume mesh to discretize the whole computational space and iterates the computation for many times. So it can be very time-consuming when it is performed on a general-purpose central processing unit (CPU). The modern graphics processing unit (GPU) with high parallel computing performance can be used to accelerate the FDTD algorithm. Compared to CPU, GPU is a massively multithreaded many-core chip which consists hundreds of smaller cores. GPU has high memory bandwidth and is optimized to execute a massive number of threads with latency hiding. It offers a good computational performance with low cost.

3.1 GPU Architecture

GPU is composed of several streaming multiprocessors (SM) as shown in Figure 3.1(a). Each SM contains 32 cores, 16 load/store units, four special function units, 64KB shared memory/L1 cache, and warp scheduler, as shown in Figure 3.1(b). This is the so-called "Fermi Architecture" [36].

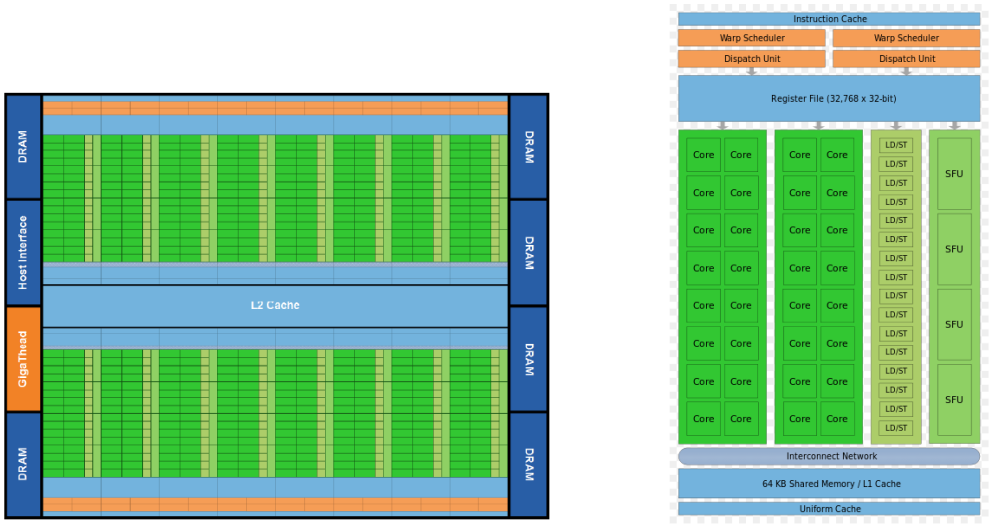

(a) (b)

Figure 3.1 (a) Nvidia Fermi GPU architecture [36]; (b) Structure of streaming multiprocessor [36].

Threads run in a group of 32 are called a warp. Each core in SM executes threads, a SM executes one or more thread blocks and a GPU executes one or more kernel grids. The concept of thread block and kernel grid will be discussed in the next section.

3.2 GPU memory hierarchy

The function executed on GPU is called kernel. The kernel is executed in parallel by many device threads (here device means GPU). Threads are grouped into blocks, and blocks are grouped into grid. The maximum number of threads in a block is 1024 in Fermi architecture. The thread, block and grid hierarchy is shown in Figure 3.2(a), the "host" in the figure means CPU [37].

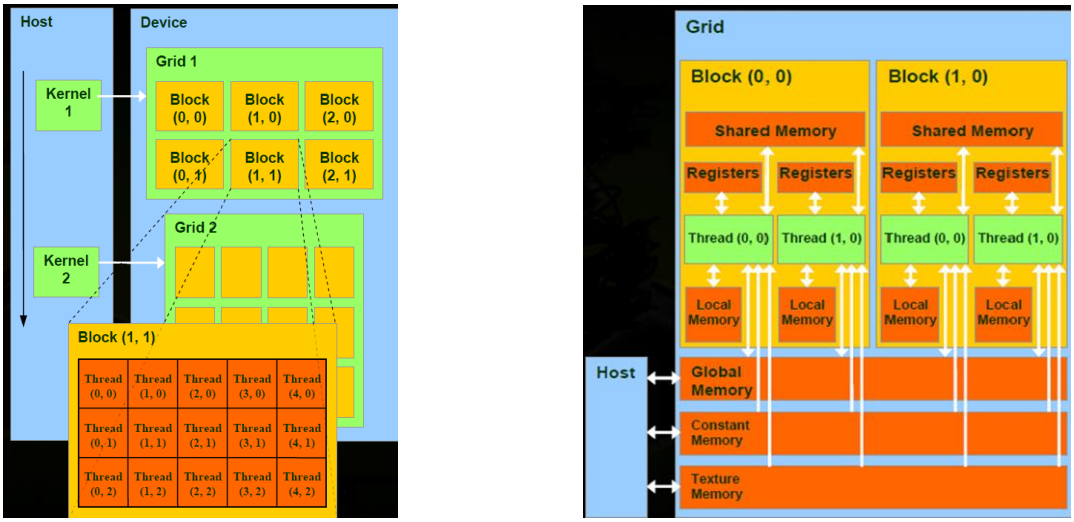

(a) (b)

Figure 3.2 (a) Demonstration of thread, block and grid hierarchy [37]. A kernel is executed by a grid. Grid is divided into blocks. Each block consists of many threads; (b) GPU memory model [37]. GPU memory consists of register, local memory, shared memory, global memory, constant memory and texture memory.

The GPU memory hierarchy is shown in Figure 3.2(b). There are six types of memory in GPU: register, local memory, shared memory, global memory, constant memory and texture memory. The device can [37]: (1) Read and write per-thread registers and local memory; (2) Read and write per-block shared memory; (3) Read and write per-grid global memory; (4) Read only per-grid constant and texture memory. The host can transfer data to or from global, constant and texture memory. The global memory is large, but it is not cached, so it is the

slowest memory. The shared memory is on-chip, so it is much faster than global memory. However the space of shared memory is limited (48KB per streaming multiprocessor in our case). Utilizing shared memory properly can improve the efficiency of program.

The GPU used in this dissertation is NVIDIA Tesla C2050, the main parameters of this GPU are shown as following:

Number of streaming multiprocessors: 14;

Total number of cores: 448;

GPU clock speed: 1.15 GHz;

Total amount of global memory: 3 GB;

Total amount of constant memory: 64 KB;

Total amount of shared memory per block: 48 KB;

Maximum number of threads per block: 1024;

Maximum size of each dimension of block: 1024×1024×64;

Maximum size of each dimension of grid: 65535×65535×65535.

3.3 CUDA programming [38, 39]

Compute Unified Device Architecture (CUDA) is a new hardware and software architecture for managing computations on GPU. It is a set of C language extensions. CUDA provides high-level application program interface (API) for GPU programming, users can develop general application programs conveniently without much knowledge about the parallel library.

CUDA model is a heterogeneous programming. A CUDA program is divided into serial portion and parallel portion. The parallel portion run on GPU (device) is called kernel. The serial portion is executed on CPU (host). The model can be shown as Figure 3.3(a). The host sends data to the device and invokes a kernel. The device executes the kernel in parallel. The data is send back to host after finishing the kernel. The kernel is executed by many device

threads, and all threads execute the same code. This parallelism is so called SPMD (single program, multiple data). The typical structure of CUDA program is shown in Figure 3.2(b).

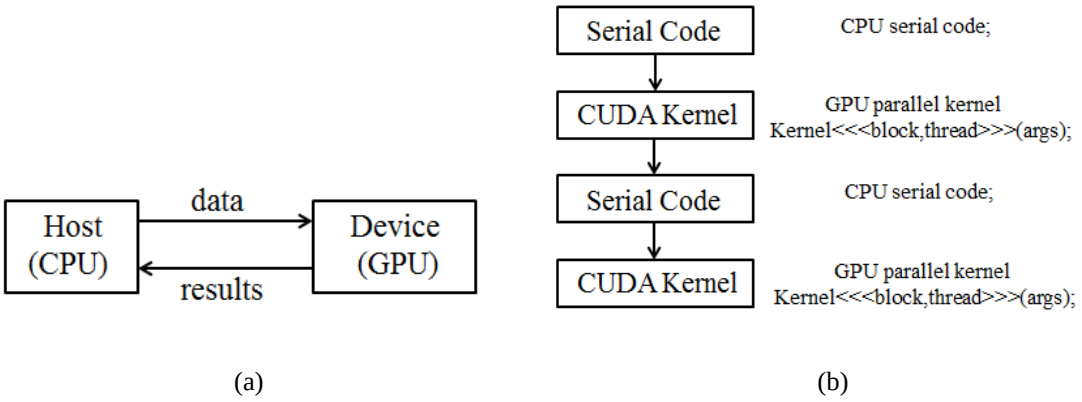

(a) (b)

Figure 3.3 (a) CUDA programming model. The host sends data to the device and invokes a kernel. The device sends results back to host after finishing the kernel; (b) Typical CUDA program structure. Serial portion is executed on CPU and parallel portion is run on GPU.

The block and grid can be one, two or three dimensional (1-D, 2-D or 3-D). For example, in Figure 3.2(a), the grid and block are two dimensional. Each block in grid or each thread in block has its own index. The built-in variables "gridDim" and "blockDim" are used to refer the dimension of grid and block, while "blockIdx" and "threadIdx" are used to refer the block and thread index in a grid and block. For example, the global index of arbitrary thread in x direction can be written as: Indx=blockIdx.x*blockDim.x+threadIdx.x.

Table 3.1 and 3.2 are the specification of several types of variable and function [38].

Table 3.1 Variable type specification in CUDA

Declaration	Memory	Scope	Lifetime
__shared__	Shared memory	Block	Kernel
__device__	Global memory	Grid	Application
__constant__	Constant memory	Grid	Application

Table 3.2 Function type specification in CUDA

Declaration	Executed on	Callable from
__global__	Device	Host
__host__	Host	Host
__device__	Device	Device

3.4 Implementation of FDTD based on GPU

Since its high computing performance, GPU has been a great interest of many researchers. In [40] Paulius described GPU parallelization of finite difference algorithm. [41] and [42] gave the implementation of FDTD using GPU and compared its performance. In [43], they implement FDTD on a multi-GPU cluster. PML based on GPU was discussed in [44]. We implement FDTD algorithm on GPU, the program flow chat is shown in Figure 3.4:

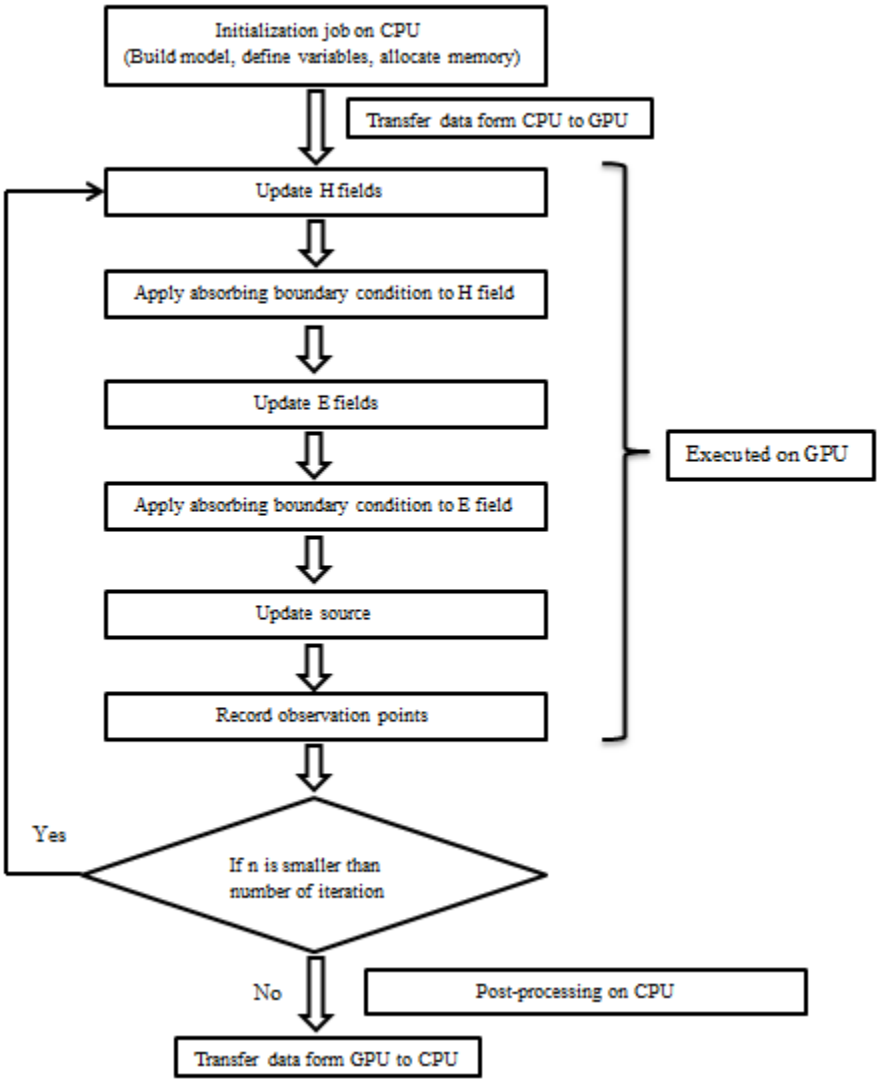

Figure 3.4 Flow chat of FDTD based on GPU.

3.4.1 GPU performance

Since CUDA grid and block can be 3-D organization, the 3-D FDTD space can be mapped to GPU conveniently. The kernel functions for updating E field and H field are shown in Figure 3.5 and 3.6. Since 3-D FDTD computational space is mapped to 3-D CUDA grid and block, we call this approach as 3-D mapping

```
__global__ void UpdateE()
{
    using namespace device;
    int i,j,k;

   i = blockIdx.x * blockDim.x + threadIdx.x;
   j = blockIdx.y * blockDim.y + threadIdx.y;
   k = blockIdx.z * blockDim.z + threadIdx.z;

   if (i>=0 && i<(Nx-1) && j>=1 && j<(Ny-1) && k>=1 && k<(Nz-1))
      Ex(i,j,k)=ce1[idxCe(i,j,k)]*Ex(i,j,k)+ce2[idxCe(i,j,k)]
                *((Hz(i,j,k)-Hz(i,j-1,k))/dy-(Hy(i,j,k)-Hy(i,j,k-1))/dz);
   if (i>=1 && i<(Nx-1) && j>=0 && j<(Ny-1) && k>=1 && k<(Nz-1))
      Ey(i,j,k)=ce1[idxCe(i,j,k)]*Ey(i,j,k)+ce2[idxCe(i,j,k)]
                *((Hx(i,j,k)-Hx(i,j,k-1))/dz-(Hz(i,j,k)-Hz(i-1,j,k))/dx);
   if (i>=1 && i<(Nx-1) && j>=1 && j<(Ny-1) && k>=0 && k<(Nz-1))
       Ez(i,j,k)=ce1[idxCe(i,j,k)]*Ez(i,j,k)+ce2[idxCe(i,j,k)]
                *((Hy(i,j,k)-Hy(i-1,j,k))/dx-(Hx(i,j,k)-Hx(i,j-1,k))/dy);
}
```

Figure 3.5 The kernel for updating E field based on 3-D mapping.

```
__global__ void UpdateH()
   {
      using namespace device;
      int i,j,k;

   i = blockIdx.x * blockDim.x + threadIdx.x;
   j = blockIdx.y * blockDim.y + threadIdx.y;
   k = blockIdx.z * blockDim.z + threadIdx.z;

   if (i>=1 && i<(Nx-1) && j>=0 && j<(Ny-1) && k>=0 && k<(Nz-1))
       Hx(i,j,k)=Hx(i,j,k)-ch_y*(Ez(i,j+1,k)-Ez(i,j,k))+ch_z*(Ey(i,j,k+1)-Ey(i,j,k));
   if (i>=0 && i<(Nx-1) && j>=1 && j<(Ny-1) && k>=0 && k<(Nz-1))
       Hy(i,j,k)=Hy(i,j,k)-ch_z*(Ex(i,j,k+1)-Ex(i,j,k))+ch_x*(Ez(i+1,j,k)-Ez(i,j,k));
   if (i>=0 && i<(Nx-1) && j>=0 && j<(Ny-1) && k>=1 && k<(Nz-1))
       Hz(i,j,k)=Hz(i,j,k)-ch_x*(Ey(i+1,j,k)-Ey(i,j,k))+ch_y*(Ex(i,j+1,k)-Ex(i,j,k));
   }
```

Figure 3.6 The kernel for updating H field based on 3-D mapping.

The performances (execution time) of GPU program with different block size are measured and compared with CPU, the results are shown in Table 3.3 and Figure 3.7. In Table 3.3, the unit of time is second; the number in parentheses is the speed up of GPU compared to CPU (CPU time/GPU time). Here we focus on the performance of updating E field and updating H field kernel and do not consider the performance of absorbing boundary.

Table 3.3 The execution time of GPU based on 3-D mapping. The unit of the execution time is second; the number in parentheses is the speed up of GPU compared to CPU.

Computation size (cells)	100×100×100	150×150×150	200×200×200	250×250×250	300×300×300
GPU block size: 4×4×4	5.07(12.82)	16.65(12.73)	38.75(12.49)	78.31(11.97)	126.82(12.65)
GPU block size: 8×8×8	3.65(17.81)	11.19(18.95)	27.32(17.72)	51.74(18.11)	87.91(18.25)
GPU block size: 8×8×16	4.45(14.61)	12.95(16.37)	30.36(15.94)	60.88(15.39)	99.11(16.18)
GPU block size: 16×8×8	3.12(20.83)	9.45(22.43)	21.58(22.42)	43.23(21.67)	68.19(23.52)
CPU	65	212	484	937	1604

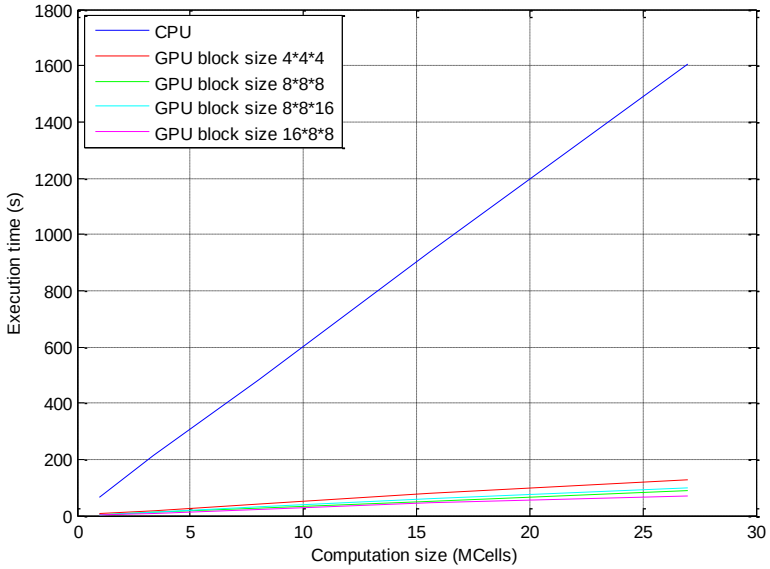

Figure 3.7 GPU execution time as a function of computation size with different block size based on 3D mapping.

As the block increasing, the occupancy increases and more latency can be hidden, so the program is more efficient. In 3-D mapping case, the block size 16×8×8 gives the optimal performance. We can also achieve parallelism by 2-D mapping. In 2-D mapping, we apply 2-D block to decompose the cells in X-Y plane, each thread compute the cells in Z direction using a for-loop. The performances of 2-D mapping are shown in Table 3.4 and Figure 3.8, here the CPU time is the same as before (shown in Table 3.3).

Table 3.4 The execution time of GPU based on 2-D mapping. The unit of the execution time is second; the number in parentheses is the speed up of GPU compared to CPU.

Computation size	100×100×100	150×150×150	200×200×200	250×250×250	300×300×300
GPU block size: 4×4	7.02(9.26)	22.56(9.40)	56.73(8.53)	108.53(8.63)	196.77(8.15)
GPU block size: 8×8	6.24(10.42)	21.83(9.71)	54.56(8.87)	114.31(8.20)	199.97(8.02)
GPU block size: 16×16	5.55(11.41)	18.71(11.33)	43.46(11.14)	86.82(10.79)	149.17(10.75)
GPU block size: 32×32	2.43(26.75)	7.02(30.20)	17.86(27.10)	32.70(28.65)	57.1(28.09)

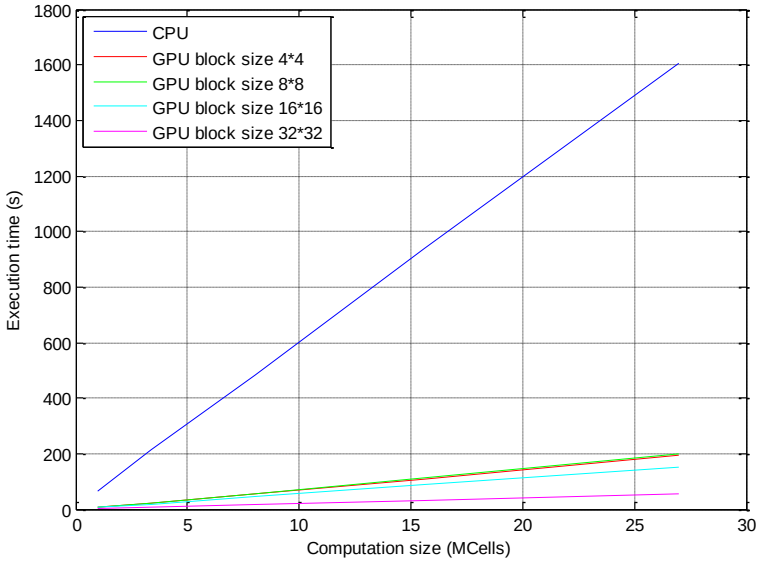

Figure 3.8 GPU execution time as a function of computation size with different block size based on 2D mapping.

To improve the GPU efficient, we should use shared memory as much as possible to avoid multiple transfers from global memory. In FDTD algorithm, each E field component is used four times when updating H field around it and each H field component is also used four times when updating E field around it, as shown in the Figure 3.9. So when updating E field, we can put H field into shared memory, and when updating H field, we can put E field into shared memory, so that accessing global memory just happen once for each field component. However, since per-block shared memory space is limited, so the block size is limited (in our case is 8×8×4). The execution time of shared memory is shown in Table 3.5.

Table 3.5 The execution time of GPU based on shared memory. The unit of the execution time is second; the number in parentheses is the speed up of GPU compared to CPU.

Computation size	100×100×100	150×150×150	200×200×200	250×250×250	300×300×300
GPU block size: 8×8×4	3.51(18.52)	10.69(19.83)	25.54(18.95)	50.50(18.55)	80.92(19.82)

(a) (b)

Figure 3.9 (a) Each E field component is used four times when updating H field around it; (b) Each H field component is used four times when updating E field around it.

3.4.2 Simulation example

In this section, we simulate a birdcage coil with 24 channels. The diameter of the coil is 280mm and the height is 190mm. In FDTD, the coil is represented by staircase grid which is shown in the Figure 3.10. There are 8 capacitors on each channel and there is a little gap between channels. All 24 channels couple together to produce a birdcage mode. The resonant frequency can be adjusted by tuning the capacitor. In Figure 3.11(a), the birdcage mode is tuned to 128MHz, and the B_1^+ distribution at 128MHz in a spherical phantom is shown in Figure 3.11(b). The relative permittivity of the phantom is 36 while the conductivity is 0.657S/m. As we can see the B_1^+ field in the sphere is very homogeneous.

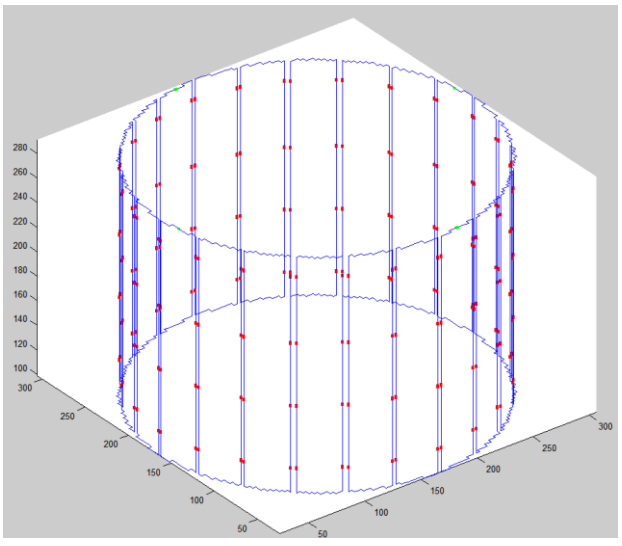

Figure 3.10 The staircase grid of 24 channel birdcage coil. The diameter of the coil is 280mm and the height is 190mm. Each channel has 8 capacitors (the red point in the figure). There is a little gap between channels.

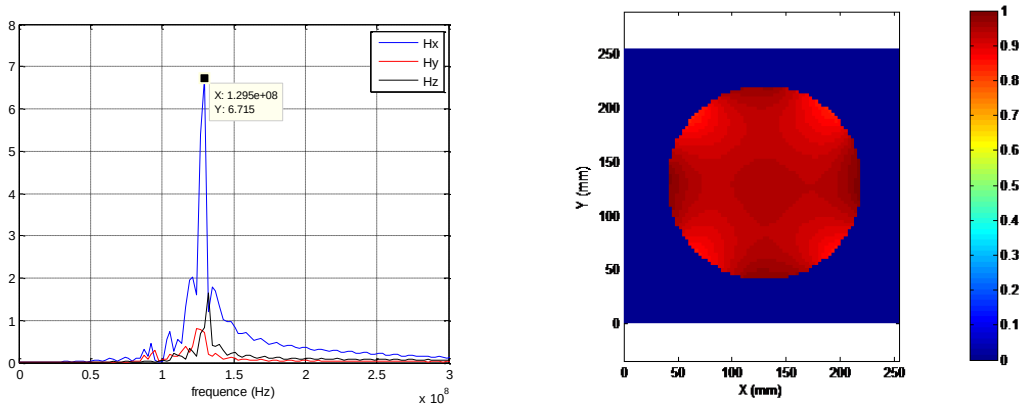

(a) (b)

Figure 3.11 (a) The birdcage coil is tuned to 128MHz. Observe the magnetic field in frequency domain on an arbitrary point, the peak of birdcage mode is tuned to 128MHz; (b) B_1^+ field distribution at 128MHz in a spherical phantom. The relative permittivity of the phantom is 36 and the conductivity is 0.657S/m.

In Figure 3.12, a human head model is placed at the center of the birdcage coil. The parameter of the human model will be discussed in detail in next chapter. There is a RF shield surrounding the coil. The spatial resolution is 3mm in the following simulation. 7 layers of 4th order PML are surrounding the computational space. The total number of cells of whole computational space is: $177 \times 127 \times 157$ (including PML). We simulate this coil at 64MHz(1.5T), 128MHz(3T), 298MHz(7T) and 498MHz(11.7T) respectively. Steady state electromagnetic fields are recorded at each frequency. This model is simulated with both CPU and GPU, the speed of GPU is about 12 times faster than CPU.

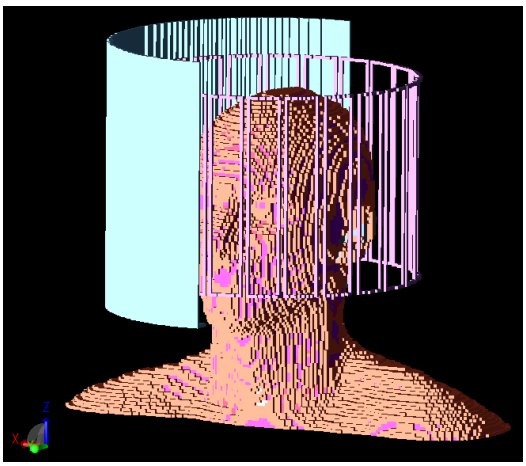

Figure 3.12 Human head model in the birdcage coil. The midpoint between the innermost points of the eyes aligns with the coil center in the longitudinal direction. There is a RF shield surrounding the coil (we just show half of it in the figure).

The B_1^+ field and E field distribution at each frequency are shown in Figure 3.13-3.16. At each frequency, B_1^+ field at the center of the head is scaled to 1.95μT, which produces a tip angle of 90 degree in 3ms. From the results we can see that, as the frequency increases, the B_1^+ field concentrates to the center of the head gradually and becomes more and more inhomogeneous. This is due to small wavelength effect and dielectric effect. The electric field also increases with frequency as we discussed in Chapter 1. The maximum E field value at each frequency is shown in Table 3.6.

Table 3.6 The maximum electric field value in the head at each frequency

Frequency(MHz)	64	128	298	498
E field (V/m)	322.3	430.8	465.9	508.8

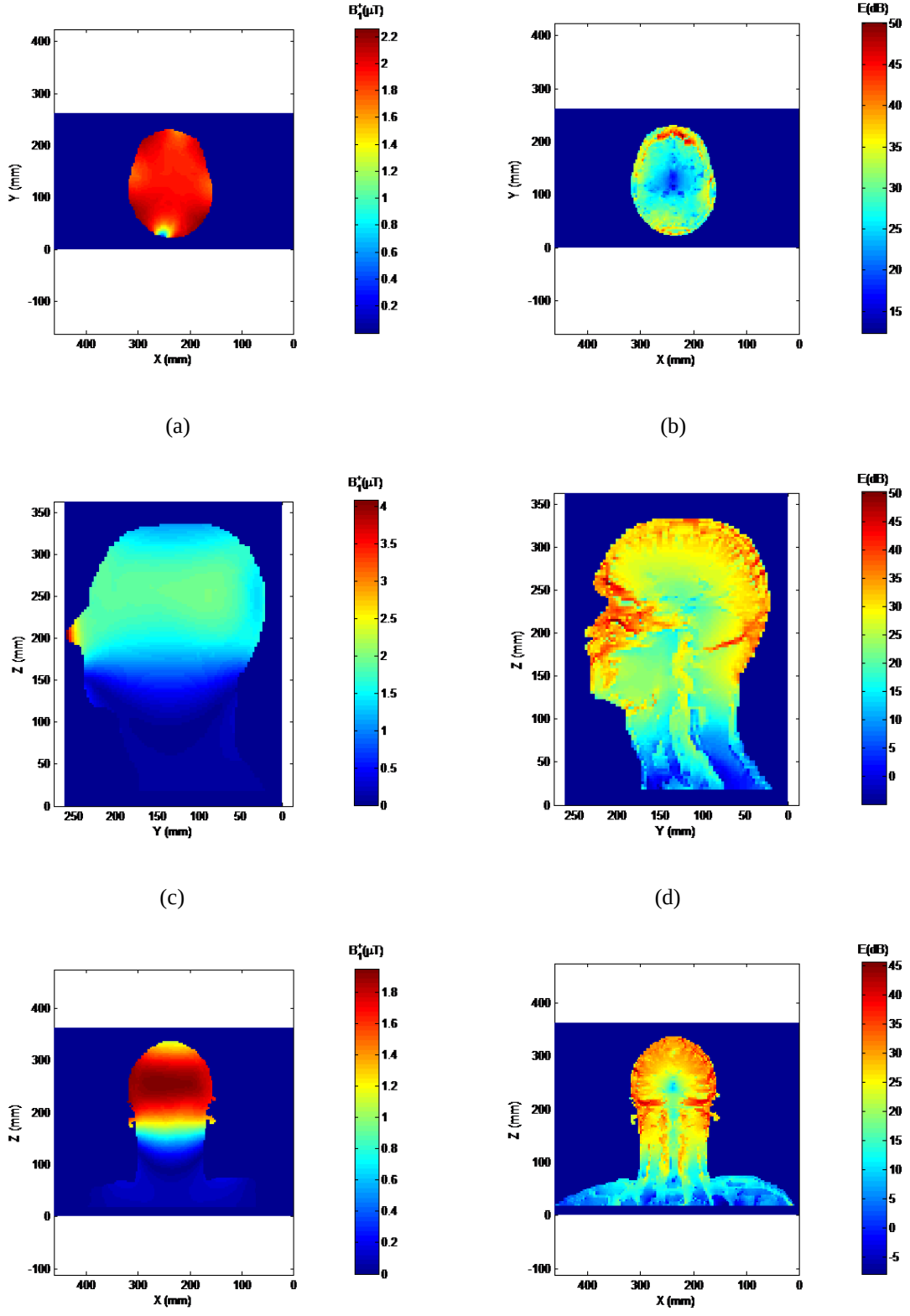

Figure 3.13 (a,b) B_1^+ field and E field distribution on transverse plane at 64MHz; (c,d) B_1^+ field and E field distribution on sagittal plane at 64MHz; (e,f) B_1^+ field and E field distribution on coronal plane at 64MHz. The unit for magnetic field is μT and for electric field is dB.

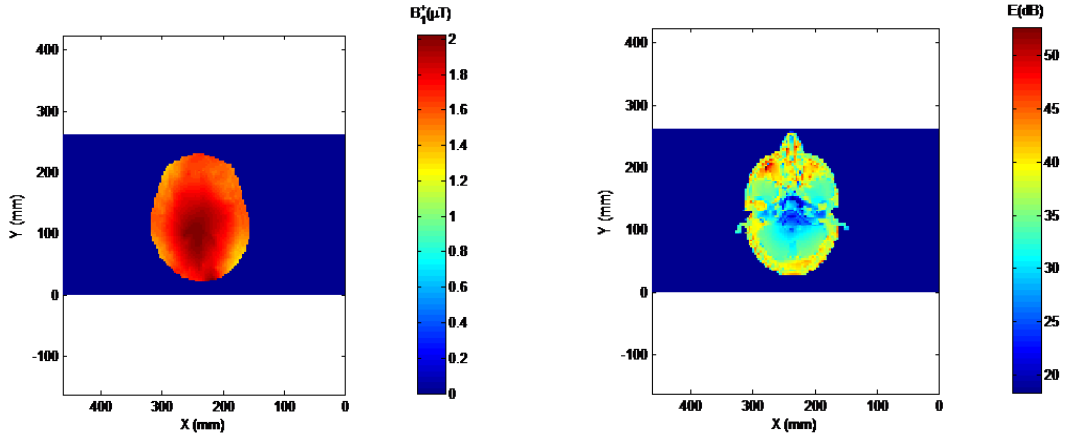

(a) (b)

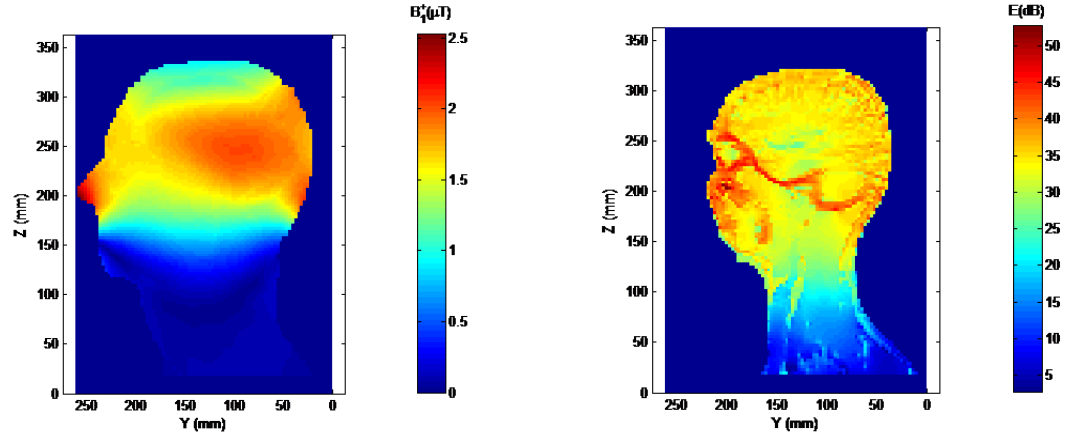

(c) (d)

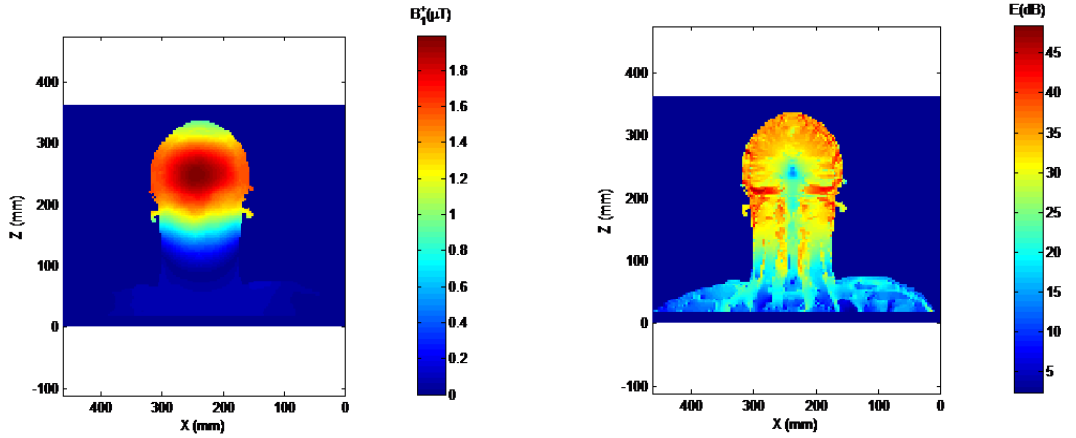

(e) (f)

Figure 3.14 (a,b) B_1^+ field and E field distribution on transverse plane at 128MHz; (c,d) B_1^+ field and E field distribution on sagittal plane at 128MHz; (e,f) B_1^+ field and E field distribution on coronal plane at 128MHz. The unit for magnetic field is μT and for electric field is dB.

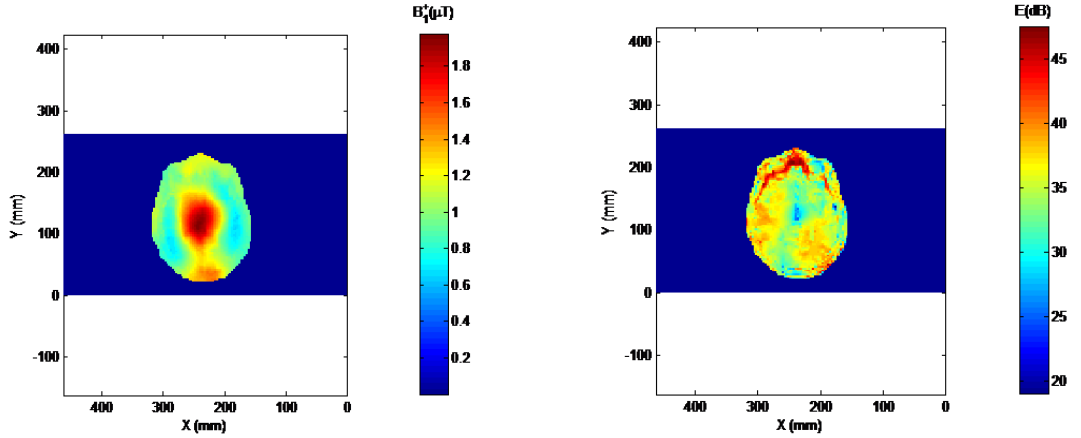

(a)

(b)

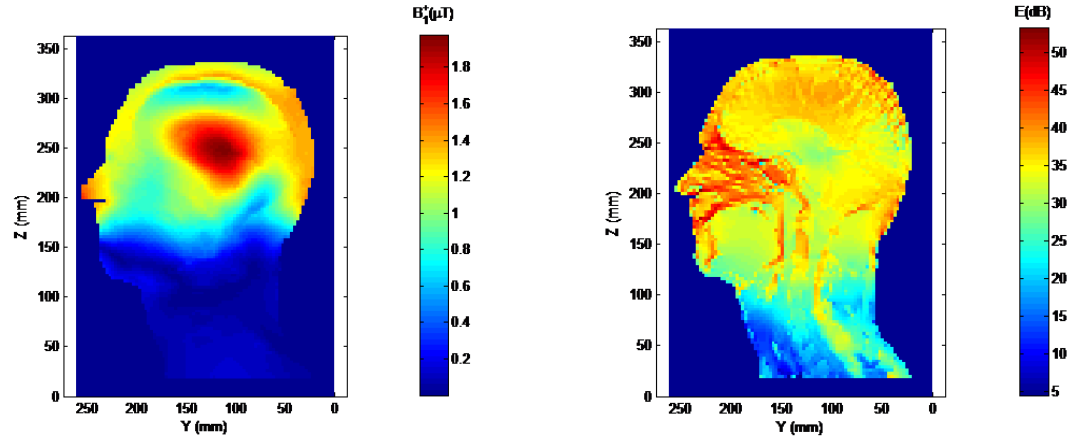

(c)

(d)

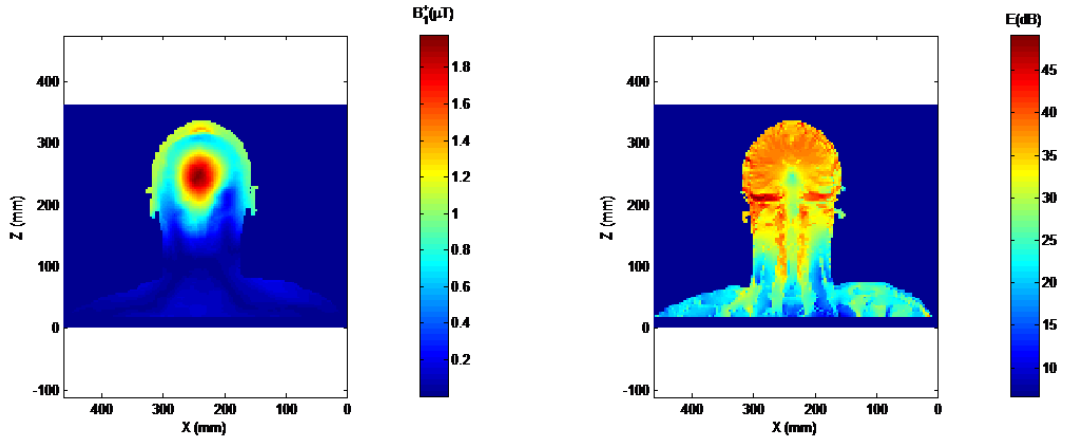

(e)

(f)

Figure 3.15 (a,b) B_1^+ field and E field distribution on transverse plane at 298MHz; (c,d) B_1^+ field and E field distribution on sagittal plane at 298MHz; (e,f) B_1^+ field and E field distribution on coronal plane at 298MHz. The unit for magnetic field is μT and for electric field is dB.

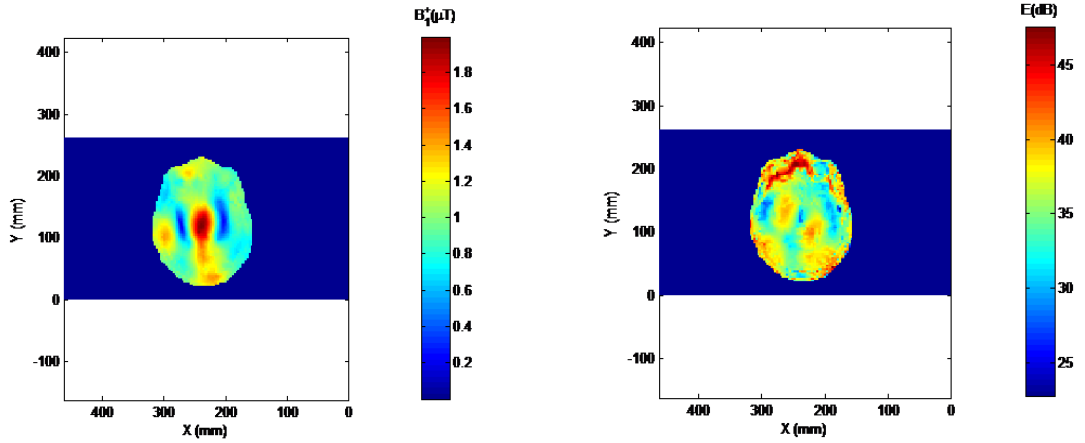

(a)

(b)

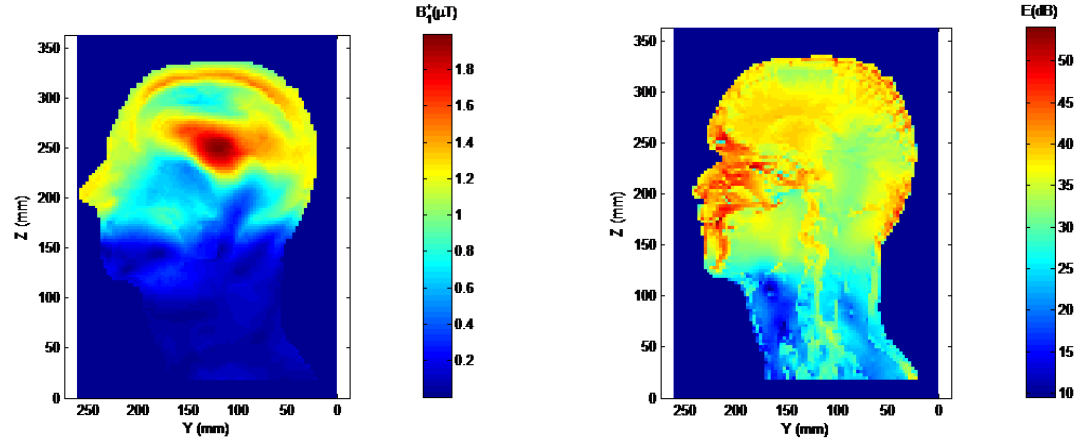

(c)

(d)

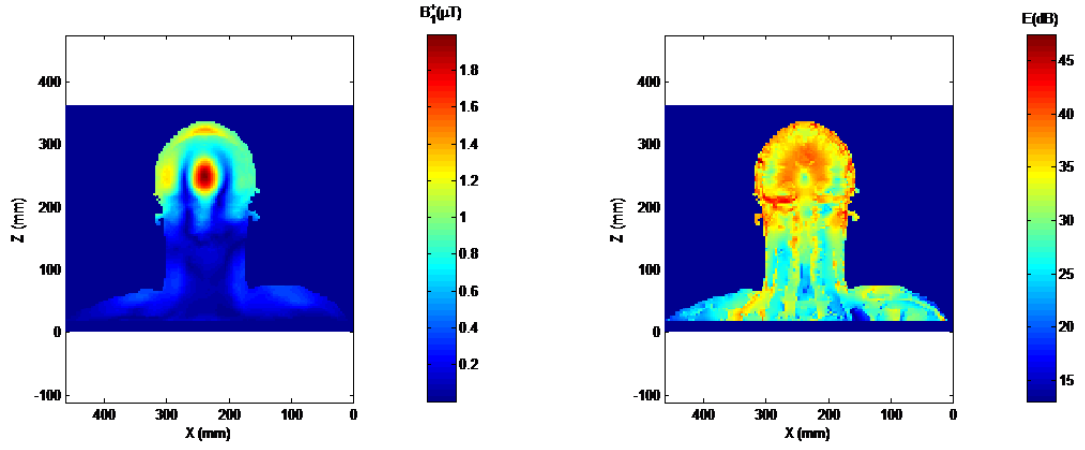

(e)

(f)

Figure 3.16 (a,b) B_1^+ field and E field distribution on transverse plane at 498MHz; (c,d) B_1^+ field and E field distribution on sagittal plane at 498MHz; (e,f) B_1^+ field and E field distribution on coronal plane at 498MHz. The unit for magnetic field is μT and for electric field is dB.

Chapter 4 SAR and Temperature Calculation In Human Model

4.1 SAR calculation

Specific absorption rate (SAR) is the RF power absorbed by per unit of mass of an object, and is measured in watts per kilogram (W/kg). It is a key safety constraint in MRI, especially in high field MRI.

4.1.1 Point SAR [45,46]

Point SAR is the average energy deposited at each voxel of human tissue over a period of time. It can be written as (4-1):

$$SAR(\vec{r}) = \frac{\sigma(\vec{r})}{\rho(\vec{r})}\frac{1}{L}\int_0^L \left\|\vec{E}(\vec{r},t)\right\|_2^2 dt \tag{4.1}$$

where $\vec{r}$ is the position vector, $\sigma(\vec{r})$ (S/m) is the conductivity, $\rho(\vec{r})$ (kg/m^3) is the density, $\vec{E}(\vec{r},t)(V/m)$ is the instantaneous field, L is the duration of the signal. If $\vec{E}(\vec{r},t)$ is sinusoid, L is the period of the wave, (4-1) becomes:

$$SAR(\vec{r}) = \frac{\sigma(\vec{r})}{2\rho(\vec{r})}\left|\vec{E}(\vec{r})\right|^2 = \frac{\sigma(\vec{r})}{2\rho(\vec{r})}\left(|E_x(\vec{r})|^2 + \left|E_y(\vec{r})\right|^2 + |E_z(\vec{r})|^2\right) \tag{4.2}$$

where $\left|\vec{E}(\vec{r})\right|$ is the magnitude of the sinusoid wave. $E_x(\vec{r})$, $E_y(\vec{r})$ and $E_z(\vec{r})$ are three components of $\vec{E}(\vec{r})$. In MRI simulation, the coil is tuned to Lamor frequency. When steady state is reached, the electric field is a sinusoid wave at Lamor frequency, so (4.2) is applied to calculate SAR in MRI. In FDTD, we calculate the electric field in time domain. To obtain the frequency domain results, we use Fourier transform. Take E_x component for example:

$$E_x(f) = \sum_{n=0}^{N} E(n\Delta t)\cos(2\pi f n\Delta t)\,\Delta t + j\sum_{n=0}^{N} E(n\Delta t)\sin(2\pi f n\Delta t)\,\Delta t \tag{4.3}$$

Here f is Lamor frequency. So in (4.2): $|E_x|^2 = (Re[E_x(f)])^2 + (Im[E_x(f)])^2$.

4.1.2 N-gram SAR [45,46]

Safety standards don't specify the point SAR but regulate the spatial-average SAR. The spatial-average SAR is usually averaged over a specified volume (1g or 10g). To calculate 1g or 10g SAR at each point, we first find a cube which is centered at that point and contains a mass of 1g or 10g within 5% error. Then we integrate the power density over this cube, the 1g or 10g SAR is calculated by dividing the integral power by cubic mass.

$$SAR(\vec{r}) = \frac{\iiint \frac{1}{2}\sigma(\vec{r})\left|\vec{E}(\vec{r})\right|^2 dv}{\iiint \rho(\vec{r}) dv} \tag{4.4}$$

The integrals in (4.4) are performed in a cube V which satisfies:

$$\sum_{\vec{r}\in V} mass(\vec{r}) \approx 1g \ or \ 10g \tag{4.5}$$

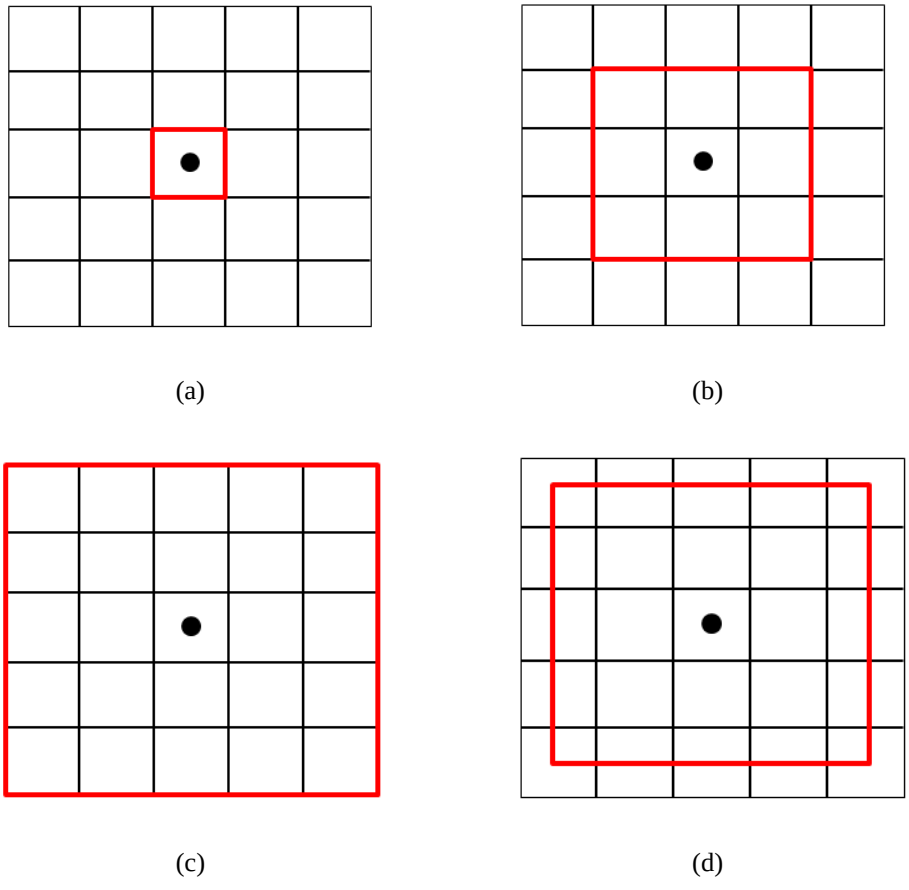

Figure 4.1 Region growth algorithm for N gram cube.

To find the N gram cube, a region growth algorithm is shown in Figure 4.1. Usually, the FDTD voxel in which the point locates is not exactly 1g or 10g cube, as shown in Figure

4.1(a), so we need to expand the cube in all directions (Figure 4.1(b)). This process continues until the mass within the cube is greater than the lower limit, here we use 5% limit which means 95%N gram (Figure 4.1(c)). If the mass contained in the cube is greater than the upper limit, here we use 5% limit which means 105%N gram, a reduction factor is multiplied to the outermost layer, the absorbing power in the outermost layer is also multiplied by this factor. We adjust this factor until the mass in the cube is less than upper limit, as shown in Figure 4.1(d).

4.1.3 Global SAR

The Food and Drug Administration and the International Electrotechnical Commission (IEC) also regulate the global SAR. Global SAR is the point SAR averaged over head or torso or even whole body. The global SAR can be calculated in the same way as N gram SAR except that the averaging volume is the head or torso or whole body instead of 1g or 10g cube.

4.1.4 SAR scaling

In FDTD simulation, the coil is driven by 1V voltage, so the SAR is for 1V voltage source. Since SAR increases with the square of electric field, so it is proportional to the square of driving voltage. The actual driving voltage is determined by the required B_1^+ field magnitude. For rectangular pulse, from (1.6) we can get:

$$B_1^+ = \frac{\alpha}{\gamma \tau_p} \tag{4.6}$$

where α is the tip angle, γ gyromagnetic ratio and τ_p is the duration of excitation pulse. Because B_1^+ magnitude is proportional to driving voltage, SAR is proportional to the square of B_1^+ magnitude. After getting the actual B_1^+ magnitude by (4.6), we can scale the SAR for 1V voltage to actual level:

$$SAR_{actual} = SAR_{1V}\left(\frac{B_{1\_actual}^+}{B_{1\_1V}^+}\right)^2 \tag{4.7}$$

4.2 Temperature calculation

The temperature distribution in the human body is evaluated by bio-heat equation developed by Pennes [47]. This equation can be solved by finite difference method [48, 49]. It has been used to calculate the temperature in human body exposed in the far field of RF electromagnetic wave [50] and predict the temperature increase in human eyes due to RF sources [51, 52]. The bio-heat equation is [50]:

$$\nabla \cdot (K(\vec{r})\nabla T) + A(\vec{r},T) + \rho(\vec{r})SAR(\vec{r}) - RL(\vec{r}) - B(\vec{r},T)(T - T_B) = C(\vec{r})\rho(\vec{r})\frac{\partial T}{\partial t} \quad (4.8)$$

In (4.8), T (℃) represents the tissue temperature which is a function of position vector $\vec{r}$ and time t. The left hand side of (4.8) represents the transferred, produced and lost heat. The five terms are as follows:

(1) $K(\vec{r})$ $[J/(s \cdot m \cdot ℃)]$ is the thermal conductivity; this term represents the heat transfer through thermal conduction;

(2) $A(\vec{r},T)[J/(s \cdot m^3)]$ represents the metabolic heat production;

(3) This term is the electromagnetic power deposition, $\rho(\vec{r})$ is the density, $SAR(\vec{r})$ is the point SAR defined in (4.2);

(4) $RL(\vec{r})$ $[J/(s \cdot m^3)]$ is the respiratory heat losses in the lungs;

(5) This term associates to the capillary blood perfusion mechanism, it is proportional to the difference between tissue temperature and blood temperature T_B, the scale factor is $(\vec{r},T)$ $[J/(s \cdot m^3 \cdot ℃)]$.

The right hand side of (4.8) is the amount of the heat required to raise the temperature. $C(\vec{r})$ $[J/(kg \cdot ℃)]$ is the specific heat capacity.

To solve equation (4.8), appropriate boundary condition must be imposed. The convective boundary condition is applied on the skin-air interface showing in (4.9) [50]:

$$-K(\vec{r})(\nabla T \cdot \hat{n})_S = H(T_s - T_A) + SW(T) \quad (4.9)$$

This boundary condition guarantees the continuity of heat flow perpendicular to the boundary surface. In (4.9), S is the boundary surface, $\hat{n}$ is the unit normal vector of the surface. The first term of right hand side represents the heat convection and radiation which is in proportion to the difference between surface temperature T_s and air temperature T_A. H $[J/(s \cdot m^2 \cdot ℃)]$ is the convection coefficient. SW(T) $[J/(s \cdot m^2)]$ stands for heat losses due to sweating. To solve bio-heat equation, we also need to know the initial condition which means the temperature distribution in human body without exposure to RF field. It can be obtained by the following steady state equation:

$$\nabla \cdot (K(\vec{r})\nabla T) + A(\vec{r},T) - RL(\vec{r}) - B(\vec{r},T)(T - T_B) = 0 \tag{4.10}$$

It is noted that in equation (4.8)-(4.9), the parameters $A(\vec{r},T)$, $B(\vec{r},T)$ and $SW(T)$ is related to temperature, in other words they are not constant. This is due to the thermoregulation mechanism of human body which regulates the body temperature to stay around 37℃ in its core. However, in our application the temperature increase is small, so thermoregulation mechanism can be ignored, and the sweating term in (4.9) is also ignored. We treat the thermal properties $A(\vec{r})$ and $B(\vec{r})$ as constant.

Now we derive the finite-difference scheme to solve equation (4.8). Take volume integral over the cell on both sides of (4.8):

$$\iiint \nabla \cdot (K(\vec{r})\nabla T)\, dv + \iiint (A(\vec{r}) - RL(\vec{r}))\, dv + \iiint \rho(\vec{r}) SAR(\vec{r})\, dv$$
$$- \iiint B(\vec{r})(T - T_B)\, dv = \iiint C(\vec{r})\rho(\vec{r}) \frac{\partial T}{\partial t} dv \tag{4.11}$$

Using divergence theorem to the first term of left hand side, we can get:

$$\oiint (K(\vec{r})\nabla T) \cdot ds + \iiint (A(\vec{r}) - RL(\vec{r}))\, dv + \iiint \rho(\vec{r}) SAR(\vec{r})\, dv$$
$$- \iiint B(\vec{r})(T - T_B)\, dv = \iiint C(\vec{r})\rho(\vec{r}) \frac{\partial T}{\partial t} dv \tag{4.12}$$

(4.12) is the thermal balance equation for each cell, the left hand side is the total heat accumulate or loss in the cell. Discretize each term respectively, we have:

(1) $\oiint(K(\vec{r})\nabla T)\cdot ds = K^{ex}_{(i,j,k)}\frac{T^n_{(i-1,j,k)}-T^n_{(i,j,k)}}{\Delta}\Delta^2 + K^{ex}_{(i+1,j,k)}\frac{T^n_{(i+1,j,k)}-T^n_{(i,j,k)}}{\Delta}\Delta^2 +$

$$K^{ey}_{(i,j,k)}\frac{T^n_{(i,j-1,k)}-T^n_{(i,j,k)}}{\Delta}\Delta^2 + K^{ey}_{(i,j+1,k)}\frac{T^n_{(i,j+1,k)}-T^n_{(i,j,k)}}{\Delta}\Delta^2 +$$

$$K^{ez}_{(i,j,k)}\frac{T^n_{(i,j,k-1)}-T^n_{(i,j,k)}}{\Delta}\Delta^2 + K^{ez}_{(i,j,k+1)}\frac{T^n_{(i,j,k+1)}-T^n_{(i,j,k)}}{\Delta}\Delta^2 \quad (4.13)$$

K^e is the equivalent average thermal conductivity, for example: $K^{ex}_{(i,j,k)} = \frac{2K_{(i-1,j,k)}K_{(i,j,k)}}{K_{(i-1,j,k)}+K_{(i,j,k)}}$,

$K^{ex}_{(i+1,j,k)} = \frac{2K_{(i+1,j,k)}K_{(i,j,k)}}{K_{(i+1,j,k)}+K_{(i,j,k)}}$, K^{ey} and K^{ez} can be derived similarly [50]. If the surface is the air-tissue interface, then the boundary condition (4.9) is applied:

$$\iint(K(\vec{r})\nabla T)\cdot ds = K(\vec{r})(\nabla T\cdot\hat{n})\Delta^2 = H(T_A - T_{(i,j,k)})\Delta^2 \quad (4.14)$$

The sweating term SW has been ignored. According to [50], if the air temperature is 30℃, the convection coefficient H is 8.3 $W/m^2\cdot$℃; according to [52], if the air temperature is 23℃, the convection coefficient H is 10.5 $W/m^2\cdot$℃.

(2) $\iiint(A(\vec{r}) - RL(\vec{r}))\,dv = (A_{(i,j,k)} - RL_{(i,j,k)})\Delta^3$ (4.15)

RL is equal to zero except in the lung.

(3) $\iiint \rho(\vec{r})SAR(\vec{r})\,dv = \rho_{(i,j,k)}SAR_{(i,j,k)}\Delta^3$ (4.16)

(4) $\iiint B(\vec{r})(T - T_B)\,dv = B_{(i,j,k)}(T_{(i,j,k)} - T_B)\Delta^3$ (4.17)

The right hand side of (4.12) can be written as:

$$\iiint C(\vec{r})\rho(\vec{r})\frac{\partial T}{\partial t}dv = C_{(i,j,k)}\rho_{(i,j,k)}\frac{T^{n+1}_{(i,j,k)}-T^n_{(i,j,k)}}{dt}\Delta^3 \quad (4.18)$$

Insert (4.13)-(4.18) into (4.12), we can get the updating equation of temperature:

$$T^{n+1}_{(i,j,k)} = \frac{K^{ex}_{(i,j,k)}dt}{C_{(i,j,k)}\rho_{(i,j,k)}\Delta^2}T^n_{(i-1,j,k)} + \frac{K^{ex}_{(i+1,j,k)}dt}{C_{(i,j,k)}\rho_{(i,j,k)}\Delta^2}T^n_{(i+1,j,k)} + \frac{K^{ey}_{(i,j,k)}dt}{C_{(i,j,k)}\rho_{(i,j,k)}\Delta^2}T^n_{(i,j-1,k)} +$$

$$\frac{K^{ey}_{(i,j+1,k)}dt}{C_{(i,j,k)}\rho_{(i,j,k)}\Delta^2}T^n_{(i,j+1,k)} + \frac{K^{ez}_{(i,j,k)}dt}{C_{(i,j,k)}\rho_{(i,j,k)}\Delta^2}T^n_{(i,j,k-1)} + \frac{K^{ez}_{(i,j,k+1)}dt}{C_{(i,j,k)}\rho_{(i,j,k)}\Delta^2}T^n_{(i,j,k+1)} + (1 - \frac{K^{ex}_{(i,j,k)}dt}{C_{(i,j,k)}\rho_{(i,j,k)}\Delta^2} -$$

$$\frac{K^{ex}_{(i+1,j,k)}dt}{C_{(i,j,k)}\rho_{(i,j,k)}\Delta^2} - \frac{K^{ey}_{(i,j,k)}dt}{C_{(i,j,k)}\rho_{(i,j,k)}\Delta^2} - \frac{K^{ey}_{(i,j+1,k)}dt}{C_{(i,j,k)}\rho_{(i,j,k)}\Delta^2} - \frac{K^{ez}_{(i,j,k)}dt}{C_{(i,j,k)}\rho_{(i,j,k)}\Delta^2} - \frac{K^{ez}_{(i,j,k+1)}dt}{C_{(i,j,k)}\rho_{(i,j,k)}\Delta^2} - N_{EXT}\frac{Hdt}{C_{(i,j,k)}\rho_{(i,j,k)}\Delta}$$

$$-\frac{B_{(i,j,k)}dt}{C_{(i,j,k)}\rho_{(i,j,k)}})T^{n}_{(i,j,k)} + N_{EXT}\frac{Hdt}{C_{(i,j,k)}\rho_{(i,j,k)}\Delta}T_A + \frac{dt}{C_{(i,j,k)}\rho_{(i,j,k)}}(A_{(i,j,k)} - RL_{(i,j,k)} + \rho_{(i,j,k)}SAR_{(i,j,k)})$$

$$+\frac{B_{(i,j,k)}dt}{C_{(i,j,k)}\rho_{(i,j,k)}}T_B \tag{4.19}$$

where N_{EXT} is the number of faces of the cell in contact with air. To keep stable, the time step dt must satisfy the following condition [53]:

$$dt \leq \frac{1}{(6-N_{EXT})\frac{K}{C\rho\Delta^2}+N_{EXT}\frac{H}{C\rho\Delta}+\frac{B}{C\rho}} \tag{4.20}$$

4.3 Human model

The human model "Duke" from the Virtual Family dataset (IT'IS Foundation, Zurich, Switzerland) [54] is applied in the following simulation. It is a 1mm resolution model and has a total of 610×310×1860 voxels. It can be downsampled to obtain 2mm, 3mm or 5mm resolutions. The model is shown in the following figures, different tissue is represented by different color.

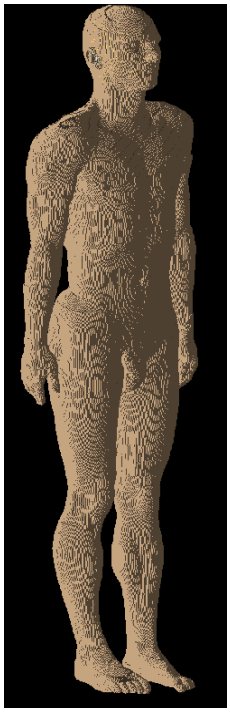

(a)

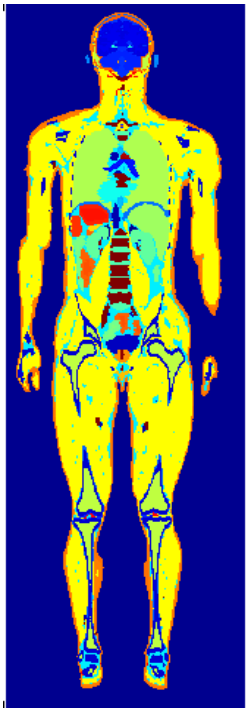

(b)

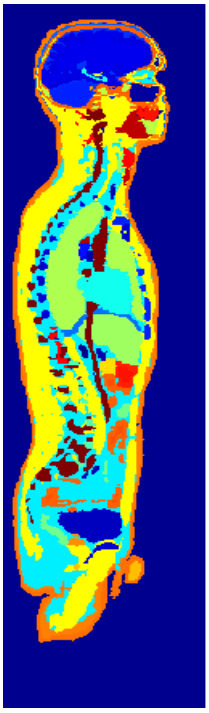

(c)

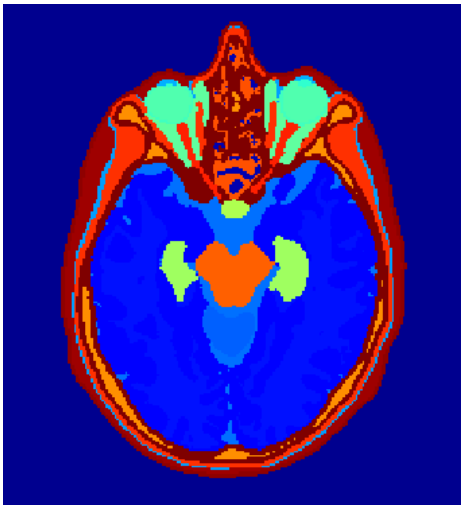

(d)

Figure 4.2 (a) 3D view of the human body model; (b) Coronal plane view; (c) Sagittal plane view; (d) Transverse plane view.

4.4 SAR and temperature calculation for head model in birdcage coil

In this section, we calculate the SAR and temperature inside human head within birdcage coil. The birdcage coil is the same as last chapter which works at 64MHz, 128MHz, 298MHz and 498MHz respectively. At each frequency, B_1^+ field at the center of the head is scaled to 1.95μT, which produces a tip angle of 90 degree in 3ms. 10g averaged SAR, 1g averaged SAR and non-averaged SAR are all calculated and scaled using (4.7). In temperature simulation, the blood temperature T_B is set to be 37℃, air temperature T_A is set to be 25℃, the convection coefficient H is 10.5 $J/(s \cdot m^2 \cdot ℃)$, and the SAR is the non-averaged SAR. At first, the temperature in the body is set to be 37℃ and (4.19) is solved without SAR term. After reaching a steady state which means the temperature does not change with time, SAR is exerted in (4.19). The total heating time is 30min, which is a quite long time for practical MRI scan. Then the temperature increase is recorded. The SAR and temperature results at each frequency are shown in Figure 4.3- 4.10. The human model is composed of 42 tissues whose electromagnetic and thermal properties at each frequency are shown in the Table 4.1-4.5. [55, 50]

Table 4.1 Relative permittivity and conductivity of human tissues at 64MHz.

Tissue	ε_r	σ
Air.(external)	1.0000000000000	0.00000000000000
Air.(internal)	1.0000000000000	0.00000000000000
Bile	105.4488919058940	1.48177962825166
Bladder	24.5943159110406	0.28735028585984
Blood	86.4441055086138	1.20666074232593
Blood vessel	68.6361788267625	0.42932184221958
Body fluid	69.1264100809191	1.50315197285649
Bone (cancellous)	30.8684307698953	0.16084574700537
Bone (cortical)	16.6811527519973	0.05952442822748
Bone marrow	7.2106707847829	0.02109725176567
Cartilage	62.9145047383907	0.45209480019171
Cerebrospinal fluid	97.3170589648346	2.06595797568467
Eye (cornea)	87.3772064084778	1.00055828255414
Eye (lens)	60.5335375842012	0.58582073154346
Eye (retina)	75.2997803464977	0.88266398247071
Eye (sclera/wall)	75.2997803464977	0.88266398247071
Eye (aqueous humor)	69.1264100809191	1.50315197285649
Fat	6.5063251622261	0.03527561043696
Gall bladder	87.4025522135963	0.96594490283030
Glands	73.9471742775246	0.77829778035665
Heart	106.5135678214960	0.67840442932998
Intestine (large)	94.6638711100021	0.63820128771871
Intestine (small)	118.3628023531230	1.59142823643623
Kidneys	118.5563908833340	0.74129552316733
Ligaments	59.4888138508120	0.47429522760532
Liver	80.5593217534498	0.44797150704298
Lung (inner)	37.1021871632134	0.28897301051074
Lung (outer)	75.2793511738438	0.53101756012910
Lymph	73.9471742775246	0.77829778035665
Mucous membrane	76.7314248103419	0.48813616635185
Muscle	72.2347570564184	0.68821797236560
Nails (toe and finger)	16.6811527519973	0.05952442822748
Nerve	55.0615538311244	0.31216043617847
Gray matter	97.4282782687255	0.51084823525054
White matter	67.8364849953373	0.29150189869282
Cerebellum	116.3477821546070	0.71897550011817
Pancreas	73.9471742775246	0.77829778035665
Skin	92.1685259703668	0.43574417441894
Spleen	110.5588089670780	0.74389578838446
Stomach	85.8203124828719	0.87783118362932
Testicles	84.5271879421094	0.88485931476361
Tooth	16.6811527519973	0.05952442822748

Table 4.2 Relative permittivity and conductivity of human tissues at 128MHz.

Tissue	ε_r	σ
Air.(external)	1.0000000000000	0.00000000000000
Air.(internal)	1.0000000000000	0.00000000000000
Bile	89.8543794004506	1.57087068778520
Bladder	21.9775976646693	0.29732788770203
Blood	73.6883628548157	1.24603182104788
Blood vessel	56.5447433493957	0.47622302010317
Body fluid	69.0646100403398	1.50514238662011
Bone (cancellous)	26.4833854493094	0.17862859266892
Bone (cortical)	14.8004727671009	0.06683538384703
Bone marrow	6.2696318523623	0.02349069325819
Cartilage	53.3388651320602	0.48605508589034
Cerebrospinal fluid	84.8073753423657	2.13845245256771
Eye (cornea)	72.1304045999583	1.05508559037752
Eye (lens)	53.3592652210107	0.60743696114973
Eye (retina)	65.4196940390799	0.91547446718967
Eye (sclera/wall)	65.4196940390799	0.91547446718967
Eye (aqueous humor)	69.0646100403398	1.50514238662011
Fat	5.9430999854781	0.03677485639096
Gall bladder	74.9082629905412	1.03736705384686
Glands	67.0791065366447	0.80250096229412
Heart	85.2310366456730	0.76058698794314
Intestine (large)	77.3425431160708	0.70108944590110
Intestine (small)	89.2245106253724	1.68667061176661
Kidneys	90.8723598823778	0.84538666806009
Ligaments	52.1504707676845	0.49730208774931
Liver	64.9569007296421	0.50695195366978
Lung (inner)	29.7860452821156	0.31397038306477
Lung (outer)	64.2404773563235	0.57290191431235
Lymph	67.0791065366447	0.80250096229412
Mucous membrane	62.2359497993900	0.54083360402727
Muscle	63.8569916034157	0.71730454728968
Nails (toe and finger)	14.8004727671009	0.06683538384703
Nerve	44.5382792609203	0.35119855620349
Gray matter	74.4774515851529	0.58226136946009
White matter	53.1522478181953	0.33919668157917
Cerebellum	81.1813231194357	0.82304340439869
Pancreas	67.0791065366447	0.80250096229412
Skin	66.5270603914673	0.51756081891714
Spleen	84.0235309852736	0.82963634747237
Stomach	75.3295641590619	0.91061265242461
Testicles	72.6325876831746	0.92381614525551
Tooth	14.8004727671009	0.06683538384703

Table 4.3 Relative permittivity and conductivity of human tissues at 298MHz.

Tissue	ε_r	σ
Air.(external)	1.0000000000000	0.00000000000000
Air.(internal)	1.0000000000000	0.00000000000000
Bile	74.9496201538353	1.66909431949412
Bladder	20.1029397704401	0.31664401620558
Blood	65.6888782735744	1.31544086769182
Blood vessel	48.3567845208585	0.53653458482315
Body fluid	69.0169164970006	1.51750206599321
Bone (cancellous)	23.1809408461512	0.21517549214108
Bone (cortical)	13.4463024764528	0.08249086350030
Bone marrow	5.7609138728595	0.02734149786639
Cartilage	46.8078810052352	0.55182459097871
Cerebrospinal fluid	72.7862114500322	2.22397196625196
Eye (cornea)	61.4304854583667	1.14992989998971
Eye (lens)	48.9722822006964	0.64741016596116
Eye (retina)	58.9338996886641	0.97483228311457
Eye (sclera/wall)	58.9338996886641	0.97483228311457
Eye (aqueous humor)	69.0169164970006	1.51750206599321
Fat	5.6353922161510	0.03953869954357
Gall bladder	62.9689013161890	1.11657555445968
Glands	62.4717054309712	0.85072446727147
Heart	69.3906421463207	0.90289224878931
Intestine (large)	65.0740275018877	0.80954461818007
Intestine (small)	69.8627954118951	1.83927322631589
Kidneys	70.5905209503022	1.02086253853912
Ligaments	48.0007289247070	0.53655808457657
Liver	53.5712423545468	0.60891434744861
Lung (inner)	24.7977935386776	0.35598928081468
Lung (outer)	56.2308182489872	0.64820500436258
Lymph	62.4717054309712	0.85072446727147
Mucous membrane	51.9589276868279	0.63008263403812
Muscle	58.2291035278374	0.77001135260581
Nails (toe and finger)	13.4463024764528	0.08249086350030
Nerve	36.9510266959299	0.41776094994507
Gray matter	60.0899795002142	0.69142050812482
White matter	43.8209987056863	0.41269810423036
Cerebellum	59.8184473443597	0.97194439876817
Pancreas	62.4717054309712	0.85072446727147
Skin	49.9016892366738	0.64038373311684
Spleen	66.5769733027606	0.96783347202509
Stomach	68.7433215063321	0.97141035408921
Testicles	64.8750795811443	0.99309532533920
Tooth	13.4463024764528	0.08249086350030

Table 4.4 Relative permittivity and conductivity of human tissues at 498MHz.

Tissue	ε_r	σ
Air.(external)	1.0000000000000	0.00000000000000
Air.(internal)	1.0000000000000	0.00000000000000
Bile	71.7211536045290	1.71970968272010
Bladder	19.4679808209466	0.33666054180450
Blood	63.2572668690599	1.38337712265586
Blood vessel	46.2292863664238	0.58558850173740
Body fluid	68.9843112721640	1.54413521230648
Bone (cancellous)	21.9496955403164	0.25396811185442
Bone (cortical)	12.9457079419806	0.10046964085587
Bone marrow	5.6190376234561	0.03122760705384
Cartilage	44.6046122094033	0.62131128777330
Cerebrospinal fluid	70.0915291640119	2.27772289340920
Eye (cornea)	57.9385191184651	1.23243051227474
Eye (lens)	47.6426252059479	0.68995524702205
Eye (retina)	56.8914350304150	1.03350428327244
Eye (sclera/wall)	56.8914350304150	1.03350428327244
Eye (aqueous humor)	68.9843112721640	1.54413521230648
Fat	5.5443724262110	0.04279262865939
Gall bladder	60.3787199132617	1.15824500514251
Glands	60.9636377018213	0.90462412245934
Heart	64.0385586359126	1.01995176784899
Intestine (large)	61.0505927790492	0.90229322185611
Intestine (small)	63.8762327329917	1.95798995114761
Kidneys	63.8297673029984	1.15894015604622
Ligaments	46.8480322551042	0.58504424121197
Liver	49.7763939050700	0.69471701513991
Lung (inner)	23.2066661731445	0.39100678489026
Lung (outer)	53.5501045331960	0.71686351295065
Lymph	60.9636377018213	0.90462412245934
Mucous membrane	48.6225850198223	0.70458922616936
Muscle	56.4454769890393	0.82246528009738
Nails (toe and finger)	12.9457079419806	0.10046964085587
Nerve	34.4489055347336	0.47278014688401
Gray matter	55.8324393738322	0.77905369759725
White matter	41.0038038278545	0.47391772263301
Cerebellum	53.7219524009872	1.08078726455995
Pancreas	60.9636377018213	0.90462412245934
Skin	44.9150496024288	0.72840426847579
Spleen	61.1760714376323	1.07751154525432
Stomach	66.7055261215978	1.03501880645834
Testicles	62.4526675906472	1.06004987605412
Tooth	12.9457079419806	0.10046964085587

Table 4.5 Thermal properties of human tissues

Tissue	C$[J/(kg\cdot℃)]$	K$_{[J/(s\cdot m\cdot℃)]}$	A$[J/(s\cdot m^3)]$	B$_{[J/(s\cdot m^3\cdot℃)]}$	ρ$[kg/m^3]$
Air.(external)	1000	0.03	0	0	1.30
Air.(internal)	1000	0.03	0	0	1.30
Bile	3900	0.55	0	0	1010.00
Bladder	3300	0.43	1600	9000	1030.00
Blood	3900	0	0	0	1058.00
Blood vessel	3500	0.47	1600	9000	1040.00
Body fluid	4000	0.6	0	0	1010.00
Bone (cancellous)	1300	0.4	590	3300	1920.00
Bone (cortical)	1300	0.4	610	3400	1990.00
Bone marrow	2700	0.22	5700	32000	1040.00
Cartilage	3500	0.47	1600	9000	1097.00
Cerebrospinal fluid	4200	0.62	0	0	1007.20
Eye (cornea)	4200	0.58	0	0	1076.00
Eye (lens)	3000	0.4	0	0	1053.00
Eye (retina)	4200	0.58	0	13500	1026.00
Eye (sclera/wall)	4200	0.58	0	0	1026.00
Eye (aqueous humor)	4000	0.6	0	0	1008.90
Fat	2500	0.25	300	1700	916.00
Gall bladder	3500	0.47	1600	9000	1030.00
Glands	3600	0.53	64000	360000	1050.00
Heart	3700	0.54	9600	54000	1029.80
Intestine (large)	3600	0.53	5200	29000	1042.50
Intestine (small)	3700	0.56	13000	71000	1042.50
Kidneys	3900	0.54	48000	270000	1050.00
Ligaments	3500	0.47	1600	9000	1220.00
Liver	3600	0.51	12000	68000	1030.00
Lung (inner)	3600	0.14	1700	9500	260.00
Lung (outer)	3600	0.14	1700	9500	1050.00
Lymph	3600	0.53	64000	360000	1040.00
Mucous membrane	3300	0.43	1600	9000	1040.00
Muscle	3600	0.5	480	2700	1046.85
Nails	1300	0.4	610	3400	1030.00
Nerve	3500	0.46	7100	40000	1038.00
Gray matter	3700	0.57	7100	40000	1038.00
White matter	3600	0.5	7100	40000	1038.00
Cerebellum	3700	0.57	7100	40000	1038.00
Pancreas	3500	0.54	7300	41000	1045.00
Skin	3500	0.42	1620	9100	1125.00
Spleen	3700	0.54	15000	82000	1054.10
Stomach	3600	0.53	5200	29000	1050.00
Testicles	3800	0.53	64000	360000	1044.00
Tooth	1300	0.4	610	3400	2160.00

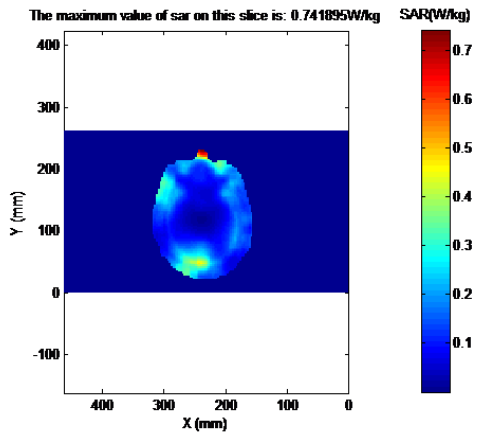

(a)

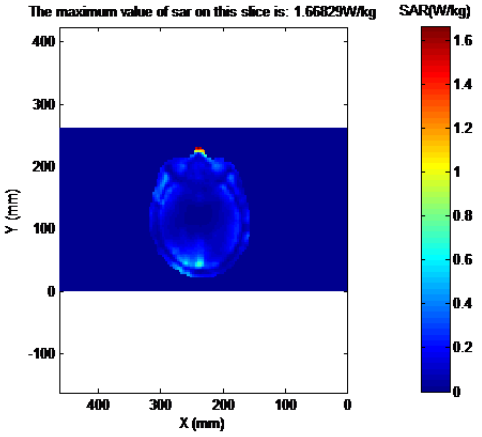

(b)

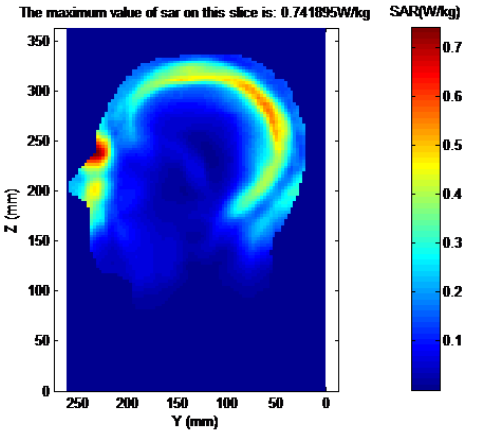

(c)

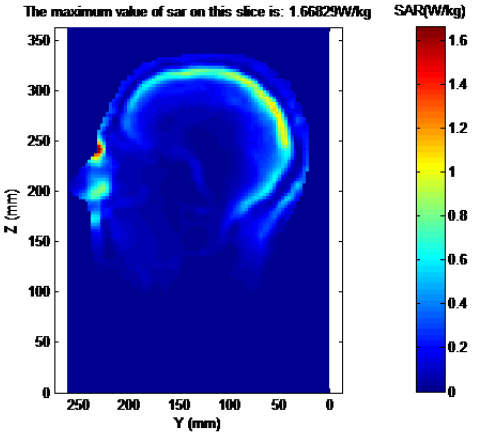

(d)

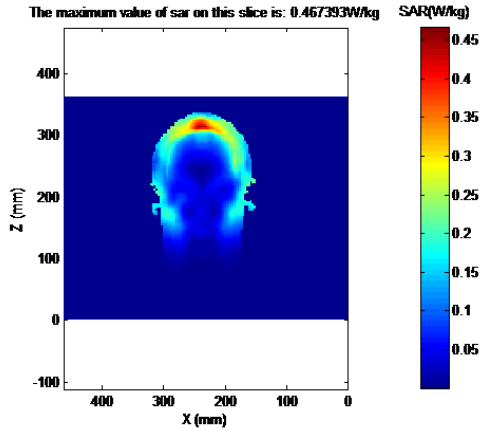

(e)

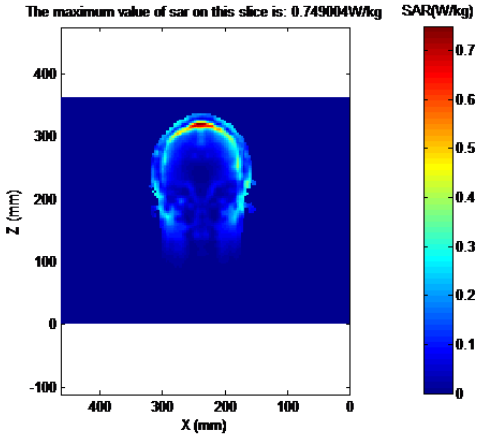

(f)

Figure 4.3 (a,b) 10g SAR and 1g SAR distribution on transverse plane at 64MHz; (c,d) 10g SAR and 1g SAR distribution on sagittal plane at 64MHz; (e,f) 10g SAR and 1g SAR distribution on coronal plane at 64MHz. The unit is W/kg.

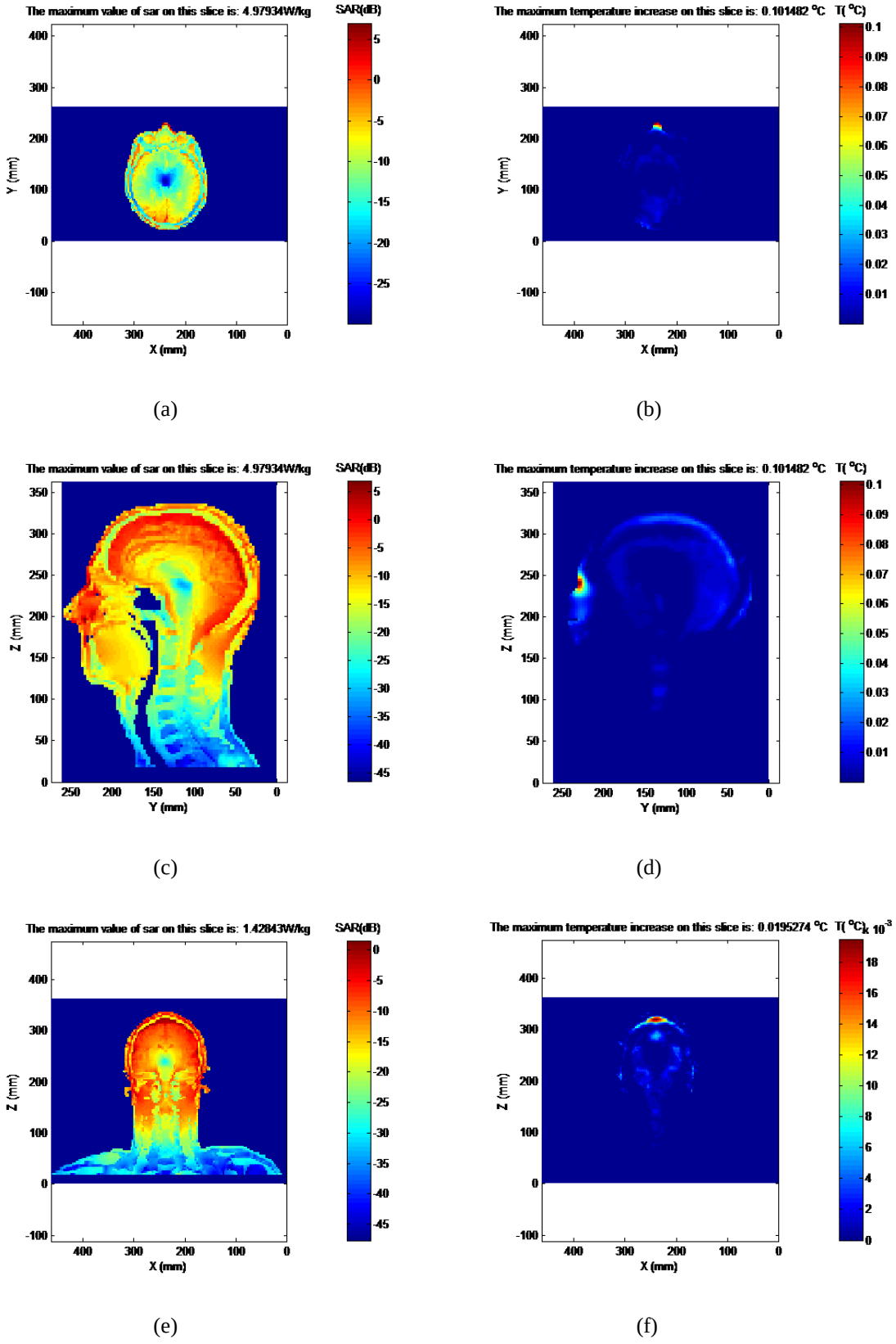

Figure 4.4 (a,b) Non-averaged and temperature distribution on transverse plane at 64MHz; (c,d) Non-averaged and temperature distribution on sagittal plane at 64MHz; (e,f) Non-averaged and temperature distribution on coronal plane at 64MHz; The unit of temperature is degree Celsius.

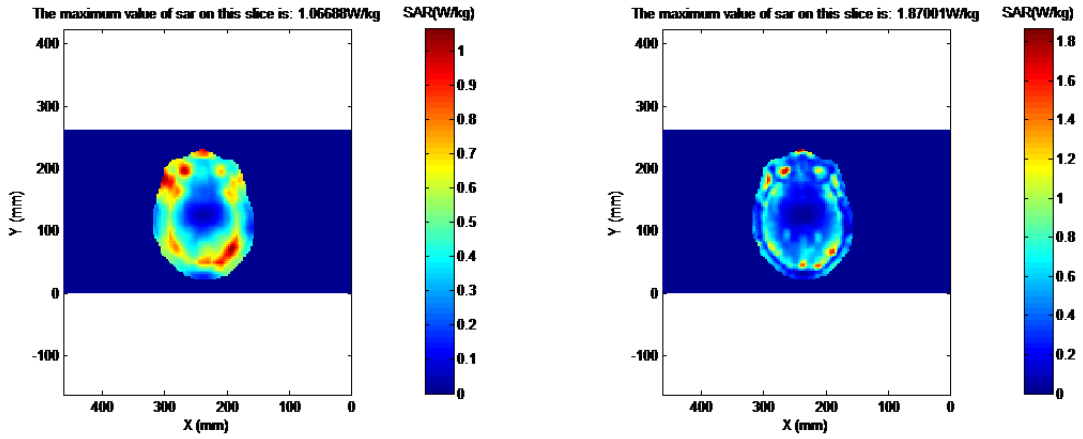

(a)

(b)

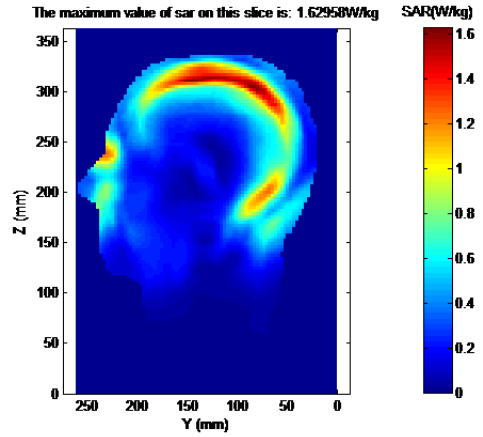

(c)

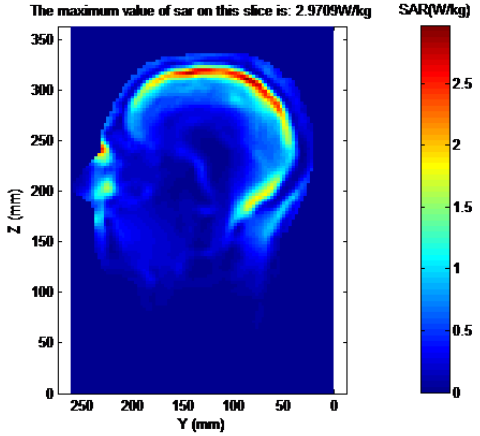

(d)

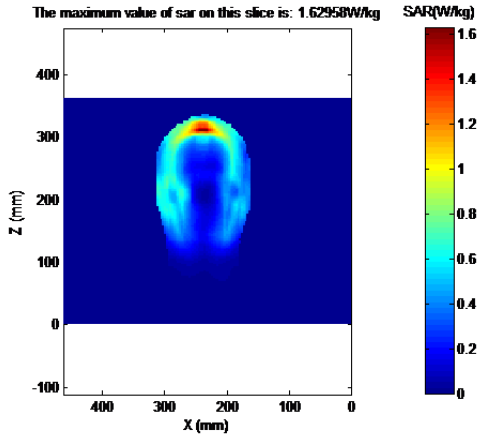

(e)

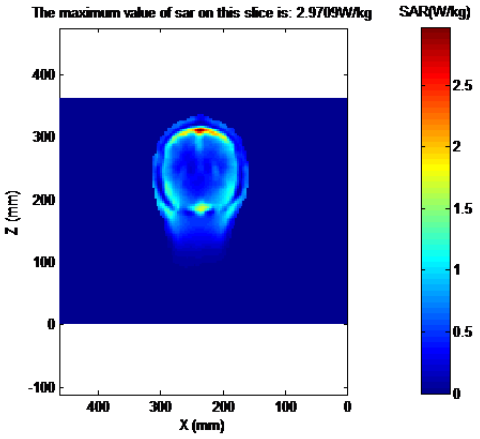

(f)

Figure 4.5 (a,b) 10g SAR and 1g SAR distribution on transverse plane at 128MHz; (c,d) 10g SAR and 1g SAR distribution on sagittal plane at 128MHz; (e,f) 10g SAR and 1g SAR distribution on coronal plane at 128MHz. The unit is W/kg.

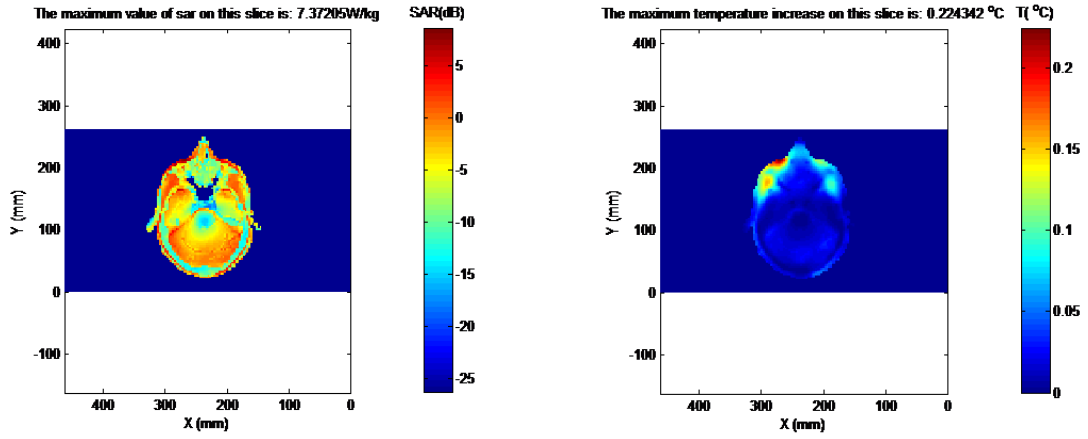

(a)

(b)

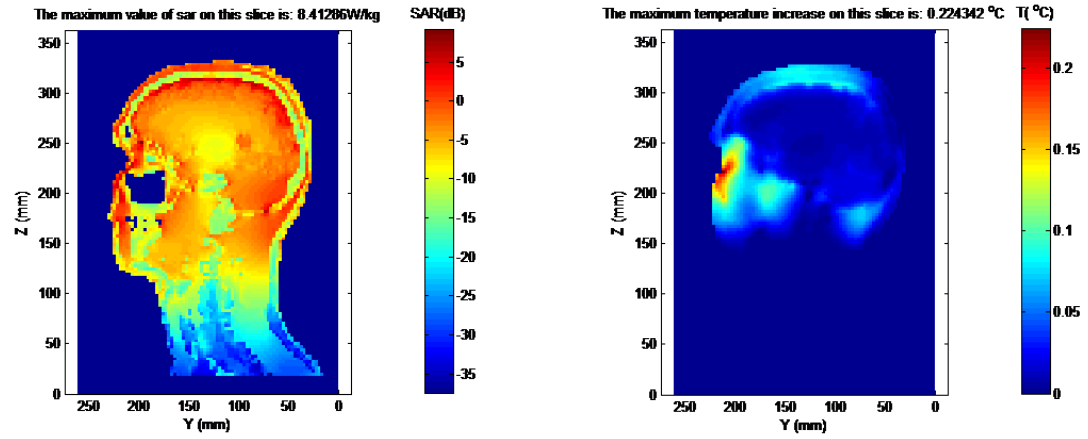

(c)

(d)

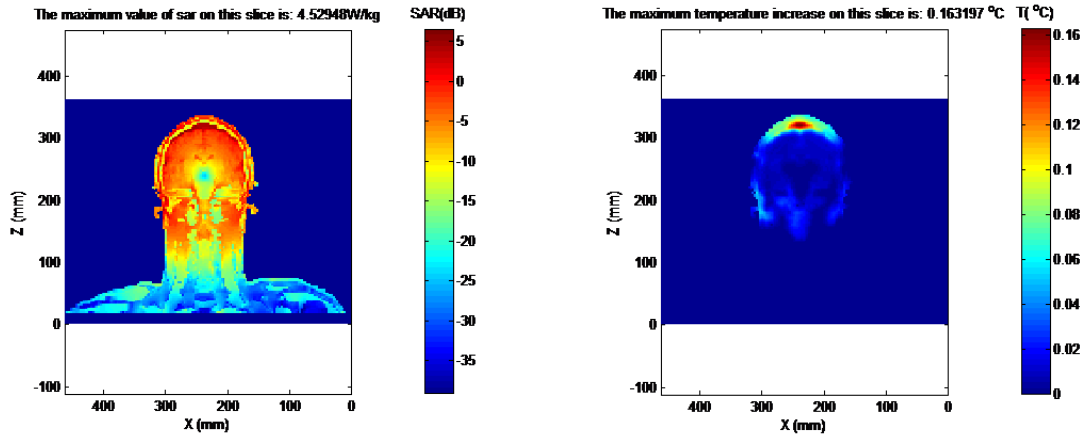

(e)

(f)

Figure 4.6 (a,b) Non-averaged and temperature distribution on transverse plane at 128M; (c,d) Non-averaged and temperature distribution on sagittal plane at 128MH; (e,f) Non-averaged and temperature distribution on coronal plane at 128MHz. The unit of temperature is degree Celsius.

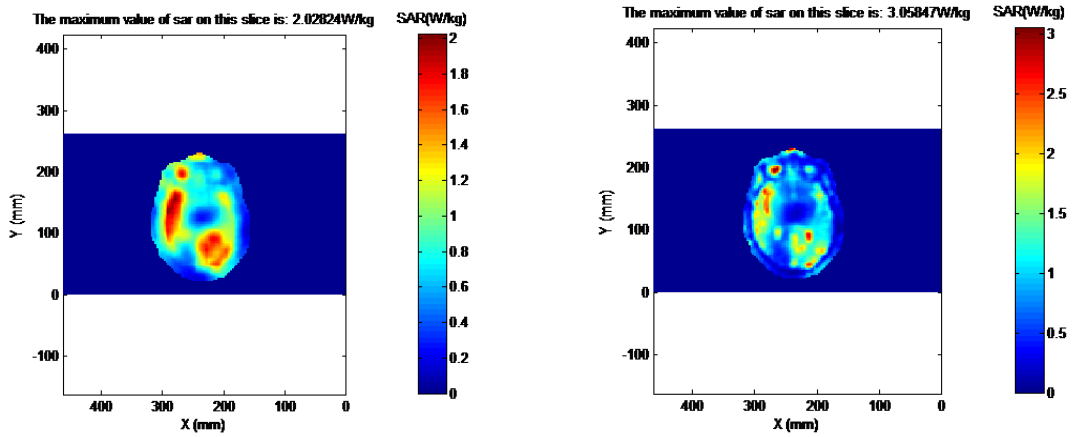

(a)

(b)

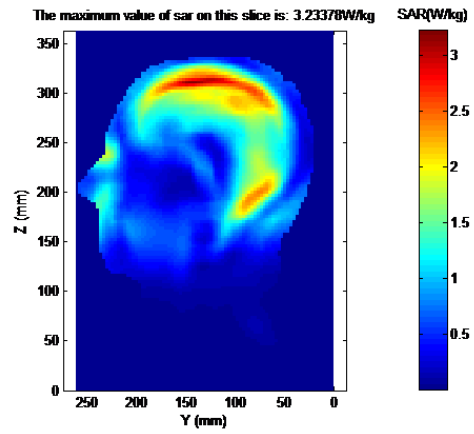

(c)

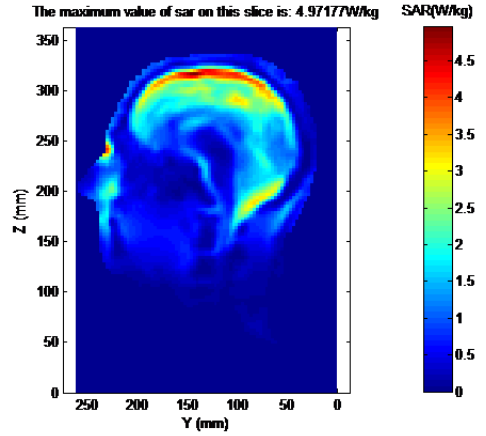

(d)

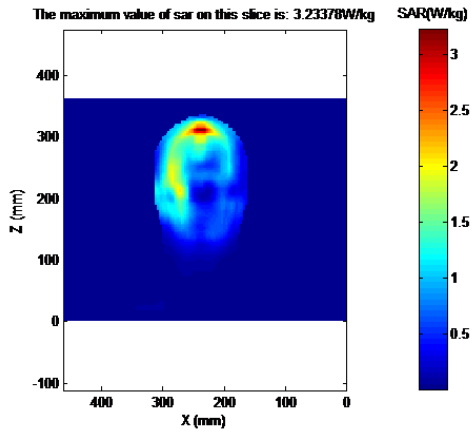

(e)

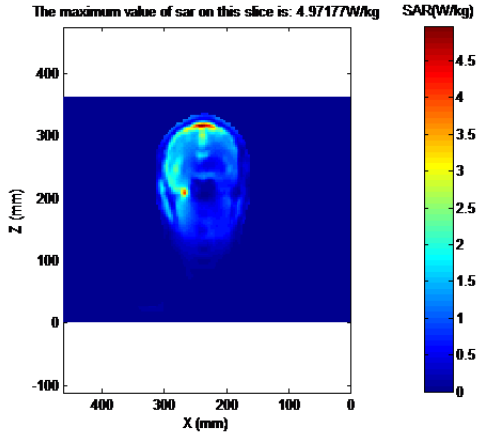

(f)

Figure 4.7 (a,b) 10g SAR and 1g SAR distribution on transverse plane at 298MHz; (c,d) 10g SAR and 1g SAR distribution on sagittal plane at 298MHz; (e,f) 10g SAR and 1g SAR distribution on coronal plane at 298MHz. The unit is W/kg.

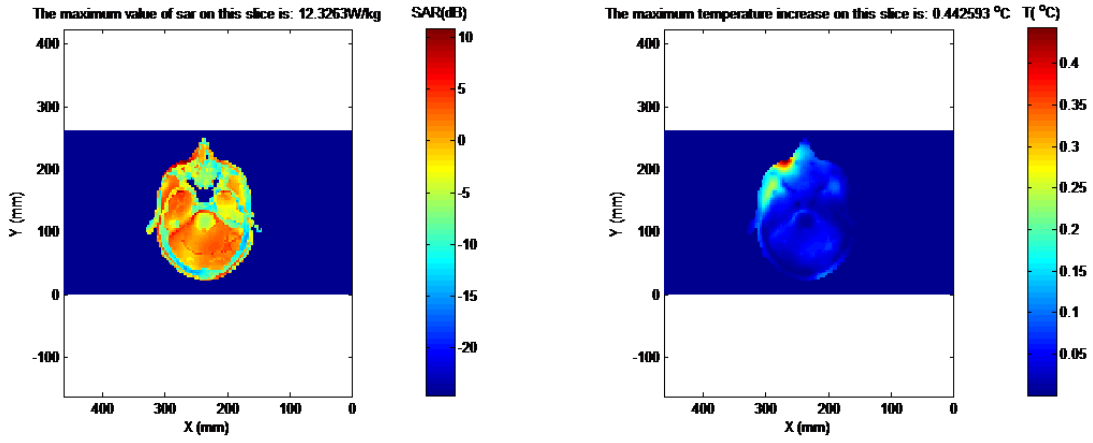

(a)

(b)

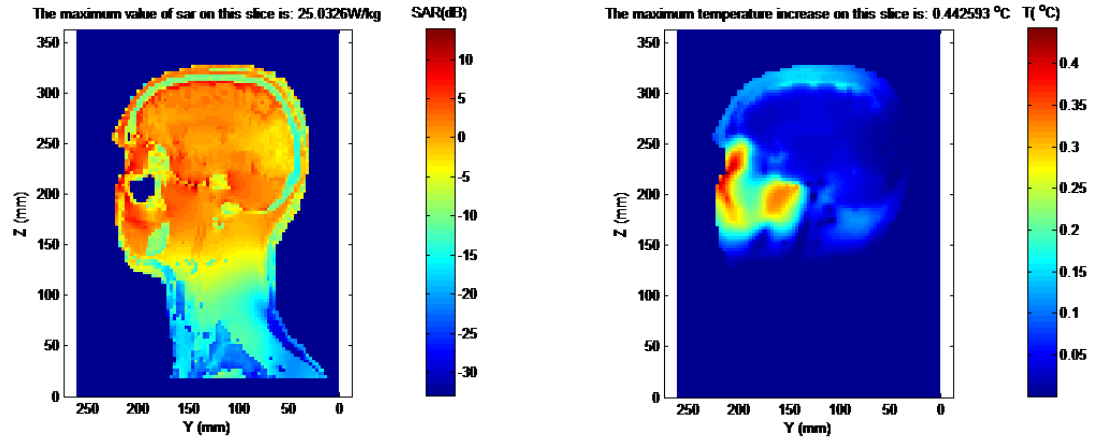

(c)

(d)

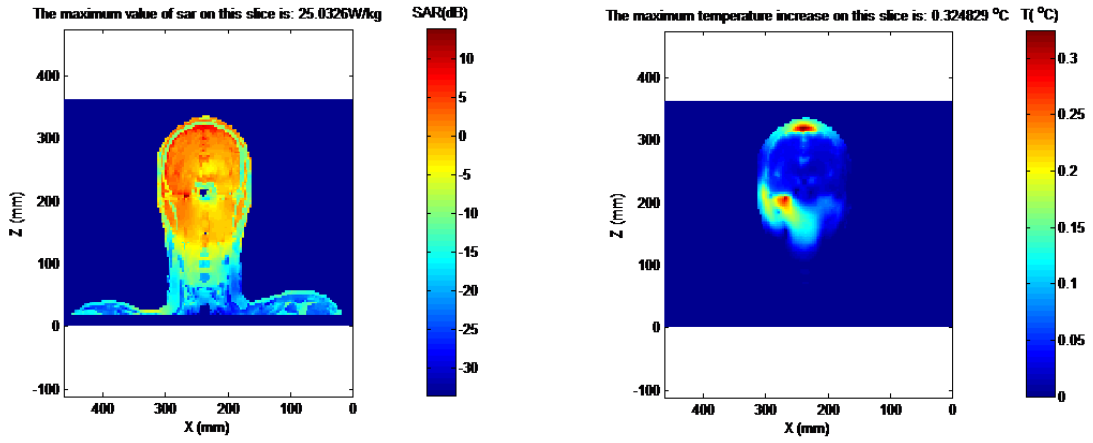

(e)

(f)

Figure 4.8 (a,b) Non-averaged and temperature distribution on transverse plane at 298MHz; (c,d) Non-averaged and temperature distribution on sagittal plane at 298MHz; (e,f) Non-averaged and temperature distribution on coronal plane at 298MHz. The unit of temperature is degree Celsius.

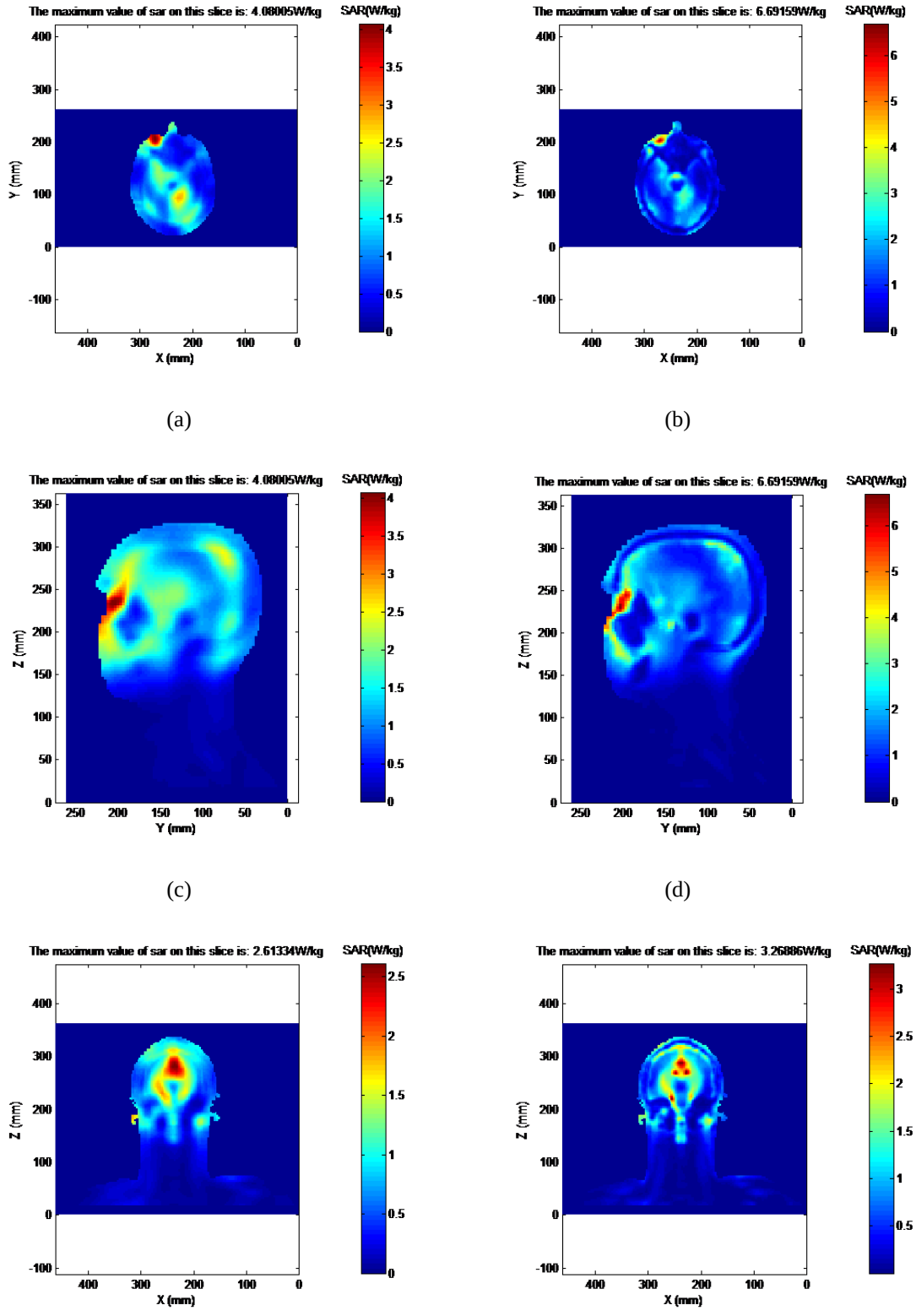

Figure 4.9 (a,b) 10g SAR and 1g SAR distribution on transverse plane at 498MHz; (c,d) 10g SAR and 1g SAR distribution on sagittal plane at 498MHz; (e,f) 10g SAR and 1g SAR distribution on coronal plane at 498MHz. The unit is W/kg.

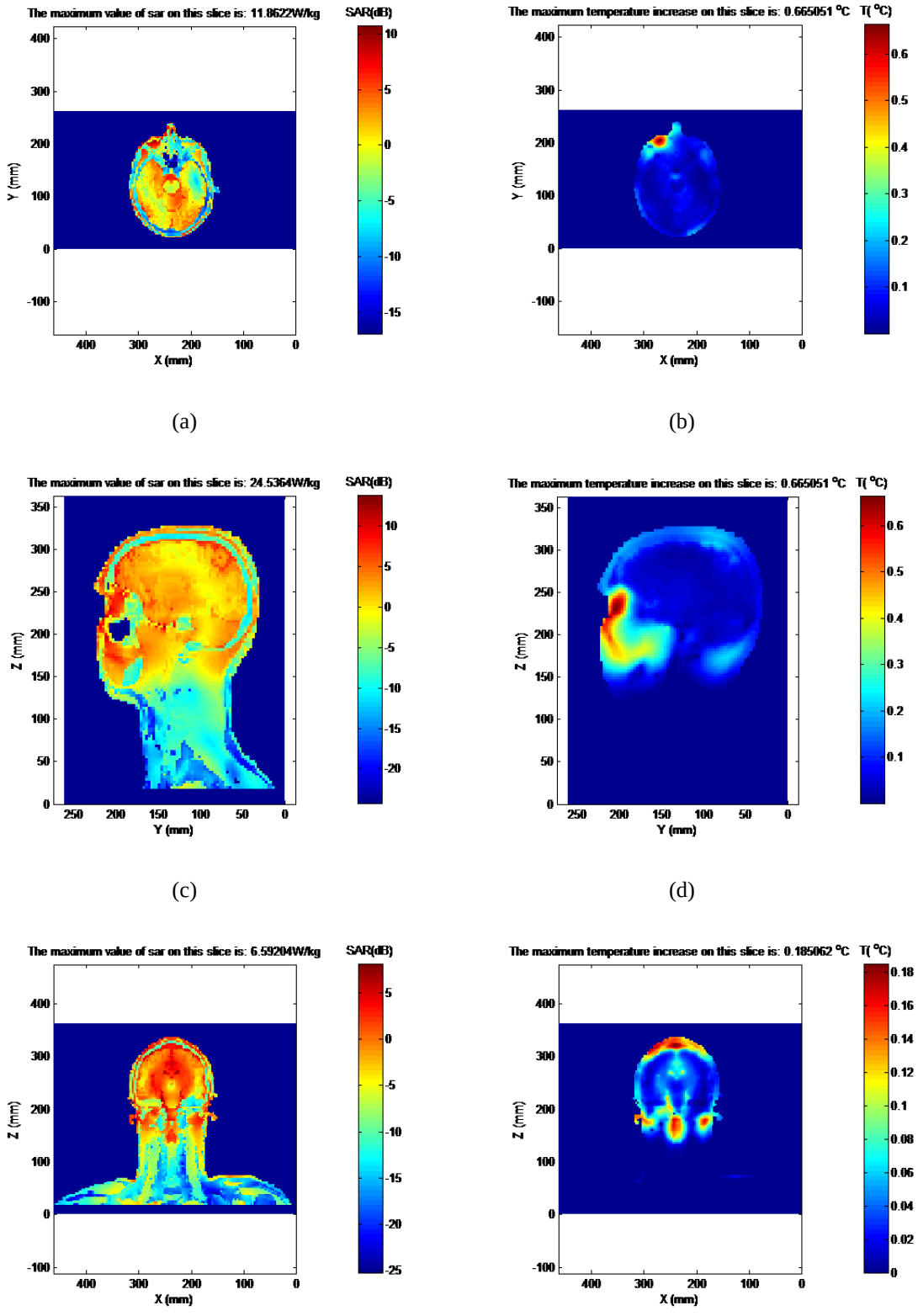

Figure 4.10 (a,b) Non-averaged and temperature distribution on transverse plane at 498MHz; (c,d) Non-averaged and temperature distribution on sagittal plane at 498MHz; (e,f) Non-averaged and temperature distribution on coronal plane at 498MHz. The unit of temperature is degree Celsius.

Table 4.6 Maximum value of 10g SAR, 1g SAR, non-averaged SAR and temperature increase at each frequency

	64 MHz	128 MHz	298 MHz	498 MHz
10g SAR(W/kg)	0.74	1.64	3.23	4.08
1g SAR (W/kg)	1.67	2.97	4.97	6.69
Non-averaged SAR (W/kg)	4.98	8.41	25.03	24.54
Temperature increase (℃)	0.10	0.22	0.44	0.67

In above figures, the non-averaged SAR is the point SAR defined by (4.2) and we show it in decibel value. The 10g and 1g SAR are defined as (4.4) and (4.5). From figure 4.3-4.10, we can see that the maximum SAR and temperature occur near the eye, so SAR supervision is important to avoid heating damage to the eye. Table 4.6 shows the maximum value of SAR and temperature increase at each frequency. As we discussed in Chapter 1, the SAR and temperature increase with frequency.

Chapter 5 Rapid Local SAR Estimation for MRI by A Hybrid Technique

5.1 Introduction

Multichannel radio frequency (RF) transmission appears to become necessary for mitigating RF field inhomogeneity caused by destructive wave interferences in high-field MRI [56]. By adjusting the phase, magnitude and RF pulse shape of each coil in a subject-specific manner, either uniform or focused RF magnetic field patterns can be generated. Although effective, the dynamic adjustment of RF transmission makes the electric fields and therefore the local SAR, also subject dependent [57, 58]. It is imperative to evaluate the local SAR in real subjects and in real time in order to ensure the safe operations of multichannel RF transmission.

In general, the local SAR is a concern to the electromagnetic compatibility of RF devices operating near the human body, e.g., cell phones, medical implants, and etc. [59, 60]. In its numerical assessment by the FDTD method [29], simulation efficiency frequently becomes a concern due to the disparate mesh size required by modeling the human body and by modeling RF devices. For instance, the local SAR obtained by using 5-mm human models only differ by less than 0.5 dB compared to the use of 1-mm human models [59]. But 5-mm mesh size is coarse for modeling fine features of many RF devices [60].

A popular approach for improving the simulation efficiency of the FDTD is the Huygens' box technique. It computes the electromagnetic fields radiated by RF devices alone and then injects the results into FDTD simulations of the human body via the total-field scattered-field (TFSF) formulation [29, 60, 62, 63]. This approach can yield accurate results if the device and the human body are weakly coupled. For strong mutual coupling, an iterative approach that applies the FDTD multiple times becomes necessary. It was demonstrated in [61] that as

many as 11 iterations could be required for simulating a 900 MHz antenna array positioned 12-inch away from the human body. Since typical RF transmits coils in high-field MRI are a few inches away from the human body, more iterations are expected and the practicality of this iterative approach for real-time local SAR estimation may be limited.

We present a hybrid local SAR simulation technique that has demonstrated real-time simulation speed with good numerical accuracy for high-field MRI coil arrays [64]. It applies fast direct method of moments (MoM) to solve the strong coil/body coupling in the frequency domain [65]. The resulting electric fields on an imaginary surface surrounding the human body are coupled into subsequent FDTD simulations of the electric fields inside the body via the Dirichlet boundary condition. Since the coil/body interaction has been resolved in MoM, it does not require iterative steps and therefore renders high efficiency.

5.2 MoM/FDTD hybrid method

The hybrid method is based on the uniqueness theorem [35]. If a human body model is enclosed inside a bounding surface and the exact tangential electric field, or magnetic field, or a mixture of both on the surface is known, the electromagnetic field inside the human body model is uniquely determined. However, the exact tangential boundary field is never known until the problem is solved. Thus, some approximation is required if one wants to utilize the uniqueness theorem to improve simulation efficiency.

The key is to realize that the bounding box is outside or on the human body, where coil/human interaction can be well resolved by treating the human body as a uniform dielectric phantom. As a result, the tangential fields on the bounding surface can be approximated by applying simulation techniques that are more efficient with uniform phantoms, e.g., the MoM. In the proposed method, the bounding surface can be either as the surface of the human body or an imaginary rectangular box outside the human body.

The former approach is more general in the sense that it can be applied if RF coils are extremely close to the human body, although this is seldom the case due to safety concerns. On the contrary, the latter is more convenient for numerical implementation and applicable to typical RF coil design, so in this approach is used in this dissertation.

After solving the tangential electric field on the bounding surface via the MoM, the solution can be enforced as the Dirichlet boundary condition in subsequent FDTD computation of the electric field inside the human body model with anatomical details. This approach will be denoted as the Dirichlet approach. Alternatively, one may also inject the tangential electromagnetic fields on the bounding surface as the incident field via the TF/SF formulation [35, 29]. As the consequence, the actual field will be the superposition of this incident field and the field scattered by internal organs. This approach will be denoted as the TF/SF approach.

In comparison, the Dirichlet approach is more efficient because the FDTD domain is restricted inside the bounding box. It eliminates the needs of computationally expensive absorbing boundary conditions, e.g., the perfectly matched layers (PML), and the associated buffer zones. Consider a human head model with 5-mm uniform spatial resolution, the Dirichlet approach would only require at most 50 Yee's cells in each dimension.

On the other hand, the TF/SF approach should be more accurate because the field scattered by internal organs will not be bounced back by the Dirichlet boundary. But it requires more computational resource. Consider the above model, the TS/FS approach would typically require at least 90 Yee's cells in each dimension. This includes ten layers PML and a ten-cell buffer zone between the PML and the TF/SF box. Since the priority of this study is simulation speed, the Dirichlet approach is applied, but we will also demonstrate the accuracy of TS/FS approach.

5.2.1 Fast direct method of moments

The conventional MoM is superior at modeling accuracy but requires relatively large computational resources. The efficiency of the MoM is significantly improved in this study by applying two techniques, i.e., the Schur complement and the fast direct MoM based on dynamic matrix compression [66, 67]. Consider the simulation of one coil with a dielectric phantom (or human body), the following linear system of equations can be established after applying Galerkin's approach to the Poggio–Miller–Chang–Harrington–Wu–Tsai (PMCHWT) formulation [64]:

$$\begin{bmatrix} [Z_{dd}] & [Z_{dc}] \\ [Z_{cd}] & [Z_{cc}] \end{bmatrix} \begin{bmatrix} \vec{X}_d \\ \vec{J}_c \end{bmatrix} = \begin{bmatrix} 0 \\ -\vec{E}^{inc} \end{bmatrix} \tag{5.1}$$

where $[Z_{dd}] = \begin{bmatrix} [Z_{dd}^{JJ}] & [Z_{dd}^{JM}] \\ -[Z_{dd}^{JM}]^T & [Z_{dd}^{MM}] \end{bmatrix}$, $[Z_{dc}] = \begin{bmatrix} [Z_{dc}^{JJ}] \\ [Z_{dc}^{JM}] \end{bmatrix}$, $[Z_{cd}] = [[Z_{dc}^{JJ}]^T \quad -[Z_{dc}^{MJ}]^T$,

$\vec{X}_d = \begin{bmatrix} \vec{J}_d \\ \vec{M}_d \end{bmatrix}$. In the above, $\vec{J}$ and $\vec{M}$ represent the equivalent surface electric and magnetic currents, superscript T represents matrix transposition, subscripts d and c denote dielectric and conductor, respectively. The format of each matrix block can be found in [68]. The surface equivalent current can be obtained by solving equation (5.1).

5.2.2 FDTD simulation with Dirichlet boundary condition

The MoM outputs equivalent currents on the surface of the human body. The tangential electric field on the Dirichlet boundary of the FDTD is evaluated from these currents via Green's function. In order to calculate the local SAR of RF arrays with certain phase/magnitude combination, the equivalent currents generated by different coils can be combined into one set of equivalent currents and the FDTD only needs to be applied once.

The Dirichlet boundary can be anywhere between the body surface and RF coils. If RF coils are not too close to the body, a regularly shaped Dirichlet boundary, such as a rectangular box, can be set and the computation of the tangential electric field on the surface does not involve much difficulty. In this dissertation, we will concentrate on this scenario. If

RF coils are extremely close to the body, choosing the surface of the human body as the Dirichlet boundary will become necessary. Two issues may arise in this scenario. First of all, the singularity of Green's function occurs when source and observation points collocate. This problem can be tackled by applying the singularity extraction technique [69].

The second problem is the mismatch between the different meshing techniques in MoM and the FDTD. The body surface is modeled in MoM by triangular patches and approximated in FDTD by stair-casing. As the result, the Dirichlet boundary will zigzag in-and-out of the MoM surface and a point that should be outside the body can appear inside the body. This ambiguity can be eliminated by exploding the MoM triangular model by 1% to include all Dirichlet boundary inside. This approximation introduces additional errors and its accuracy is studied in reference [64].

At each time step of the FDTD, the magnitude of the electric field at each Dirichlet boundary point is calculated from its phasor and enforced as a "hard" source [29]. For example:

$$E^n(i,j,k) = A(i,j,k)\cos[\omega n\Delta t + \varphi(i,j,k)] \tag{5.2}$$

where $E(i,j,k)$ is electric field component at one Dirichlet boundary point, (i,j,k) is the position index, n is the time step index, $A(i,j,k)$ and $\varphi(i,j,k)$ are the magnitude and phase of the electric filed on that point respectively. The convergence of FDTD simulation is determined via conventional procedures [29].

5.3 Accuracy of the hybrid method

In order to get a good approximation, permittivity and conductivity of the uniform phantom should be selected carefully. In this section, we will compare the results of different parameter combinations and verify the validity of this method.

5.3.1 Single loop coil with Dirichlet boundary

The local SAR induced by a 9-cm×9-cm square loop coil positioned in the front (see Figure 5.1) and on the back of the "Duke" head model are simulated [54]. The "Duke" head model consists of 12 different tissues and the electric properties of each tissue are specified according to the literature [71]. The coil center aligns with the tip of the nose. The distances between the anterior coil surface and the tip of the nose and that between the posterior coil surface and the closest point on the back of the head are 3 cm. Four capacitors were applied to numerically tune the coil to 298 MHz for each coil position. The conventional FDTD method is applied to calculate the reference local SAR results in each case. In the hybrid approach, the 12 different tissues were replaced by an equivalent medium and the tangential electric fields on a rectangular Dirichlet boundary is simulated by the conventional FDTD method. The Dirichlet boundary was 2-cm away from the head model in all directions. The use of conventional FDTD to obtain Dirichlet boundary values help isolate errors associated with equivalent medium itself, not the hybridization of different methods. Finally, the FDTD method applied with the Dirichlet boundary and the 12-tissue head model to compute the internal electric field. The spatial resolution was 3-mm uniformly in all simulations.

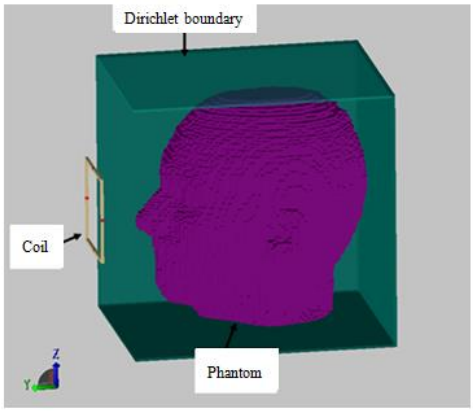

Figure 5.1 A square loop coil is positioned in front of the "Duke" head model.

Three different equivalent media have been tested. The first one has relative permittivity ε_r = 50 and conductivity σ = 0.56 S/m, which correspond to the volume-averaged properties of brain white matter and gray matter. The second one has the same relative permittivity but its

conductivity is σ = 0.657 S/m, which corresponds to 55 mM NaCl solution. The third one has relative permittivity ε_r= 36 and conductivity σ = 0.657 S/m. The permittivity is derived in such a way that the electrical size of the cross section of the head model is similar to that of the white matter region (ε_r = 43 at 298 MHz) in terms of wavelength. It has been demonstrated that this equivalent medium yields more accurate B_1^+ simulation results than other alternatives [70].

Figure 5.2 compares the convergence of the FDTD in the proposed hybrid method and that of the conventional FDTD method. In conventional FDTD, the number of time periods required for convergence is roughly proportional to the quality factor (Q-factor) of the resonant coil [29]. Since the fields on the Dirichlet boundary is the result of coil resonance (with the head) resolved through the MoM, it no longer requires as many iterations as the conventional FDTD does. It was observed that two to three time periods can provide stable results for Fourier transform [29]. Based on this figure, three time periods were applied throughout in the following simulations. In addition, the Dirichlet boundary eliminates the PML absorbing boundary. In our problem, it takes about 1.2 min. In comparison, the conventional FDTD requires at least 11 time periods which takes about 34 min.

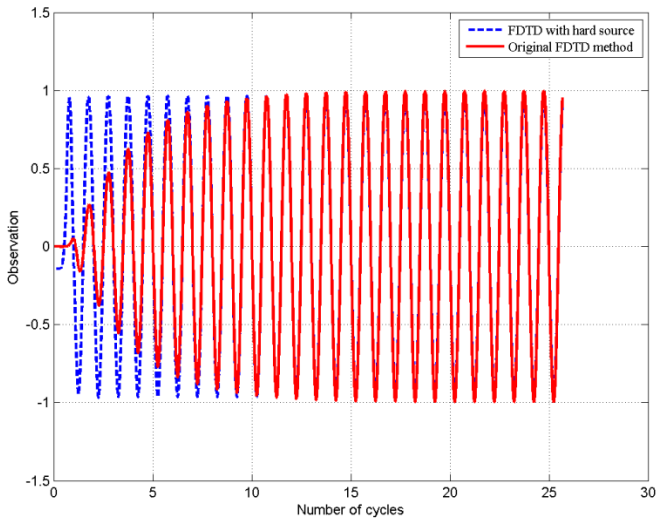

Figure 5.2 Comparison of the convergence behavior of the proposed method and the conventional FDTD method. The observation is at an arbitrary location inside the head mode and its value has been normalized to the its maximum.

Figure 5.3 shows the 10g SAR distribution on a transverse plane in human head when the coil is placed in front of the head. Figure 5.3 (a) is the result comes from real head model calculated by conventional FDTD method, this is reference result without approximation; Figure 5.3 (b) –(d) are the results calculated by the hybrid method. The equivalent media in Figure 5.3 (b), (c) and (d) are (ε=36, σ=0.657), (ε=50, σ=0.56) and (ε=50, σ=0.657) respectively. From this figure, we can see the SAR distribution pattern is almost the same among (a) – (d), the difference exists in maximum value.

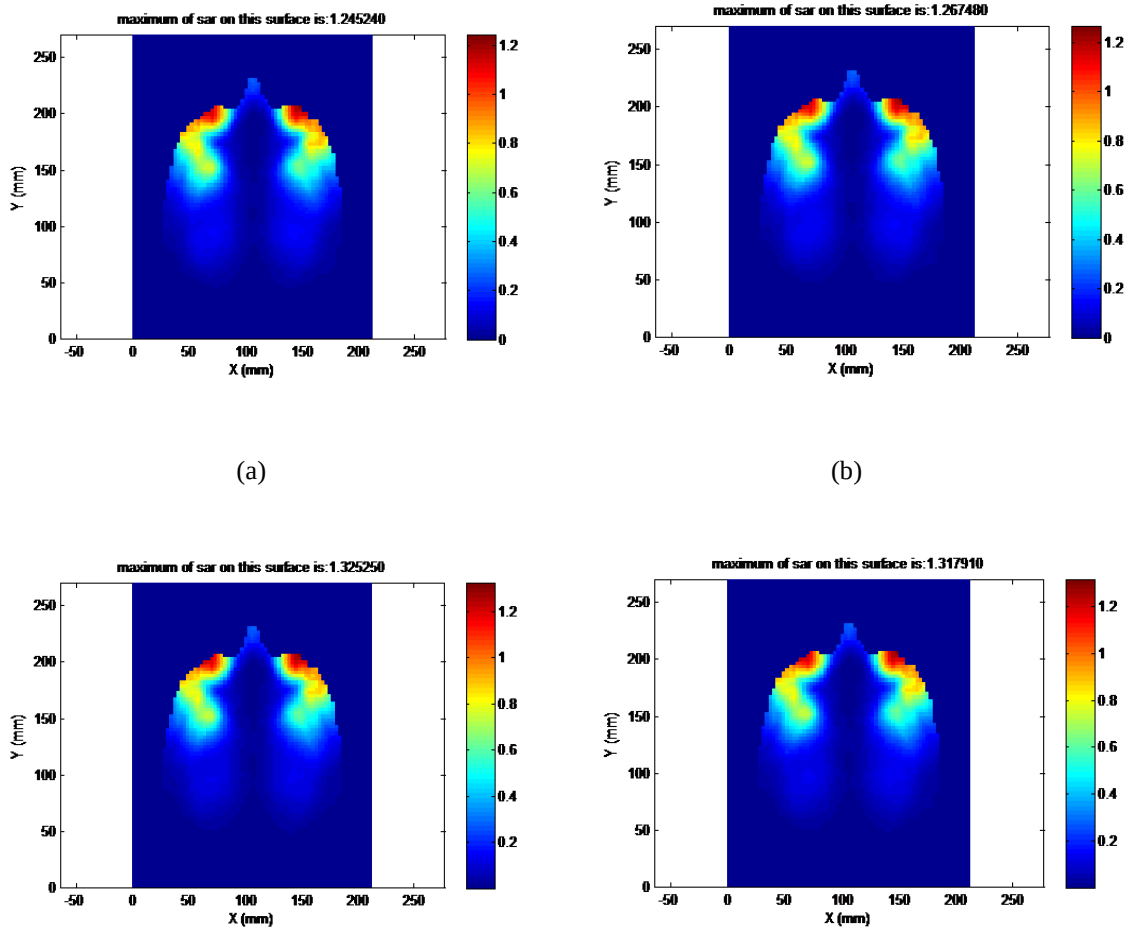

(a) (b)

(c) (d)

Figure 5.3 10g SAR distribution in human head (coil is in front of the head). (a) Reference results; (b) Results of hybrid method with equivalent medium of (ε=36, σ=0.657); (c) Results of hybrid method with equivalent medium of (ε=50, σ=0.56); (d) Results of hybrid method with equivalent medium of (ε=50, σ=0.657). The transverse views are cut through the peak local SAR position. The color bar shows the 10-g averaged local SAR as the result of 1 Watt RF power deposited in the human model. The unit is Watt/kg/Watt.

Table 5.1 shows the positions and values of global maximum SAR calculated by using different media to obtain the Dirichlet boundary. The positions of maximum SAR predicted by different media are exactly the same with reference; the maximum value is somewhat different. When ε=36, σ=0.657, the result is closest to the reference, the relative error is 1.79%.

Table 5.1 Global peak 10g averaged local SAR position and value of anterior single loop coil simulated by using different media to obtain the Dirichlet boundary. The number in the parenthesis is the relative error.

	Reference	Medium 1 ε=36, σ=0.657	Medium 2 ε=50, σ=0.56	Medium 3 ε=50, σ=0.657
Maximum SAR position (x,y,z) (mm)	(147,204,147)	(147,204,147)	(147,204,147)	(147,204,147)
Maximum SAR value (W/kg)	1.245240	1.267480 (1.79%)	1.325250 (6.43%)	1.317910 (5.84%)

The local SAR values on difference transversal slices through the head model are computed. Figure 5.4 compares the relative errors between the conventional FDTD results and those obtained by the hybrid approach. When ε=36, σ=0.657, the relative error is smaller than 5% on most slices.

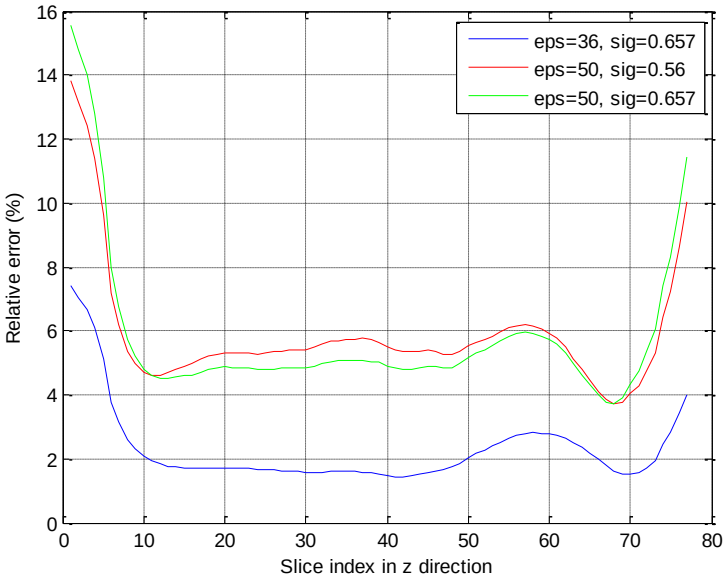

Figure 5.4 Relative error of local SAR of the anterior single coil on different transversal slices computed by using different media to provide the Dirichlet boundary. The slice indexed by 40 corresponds to the coil center.

Figure 5.5 shows the 10g SAR distribution on a transverse plane in head when the coil is placed on the back of the head. Table 5.2 indicates the positions and values of global maximum SAR. Figure 5.6 is the relative error on each slice. We can get similar conclusion as before, the phantom whose ε_r is 36 and σ is 0.657 gives the best approximation to the real head, the relative error is smaller than 5%.

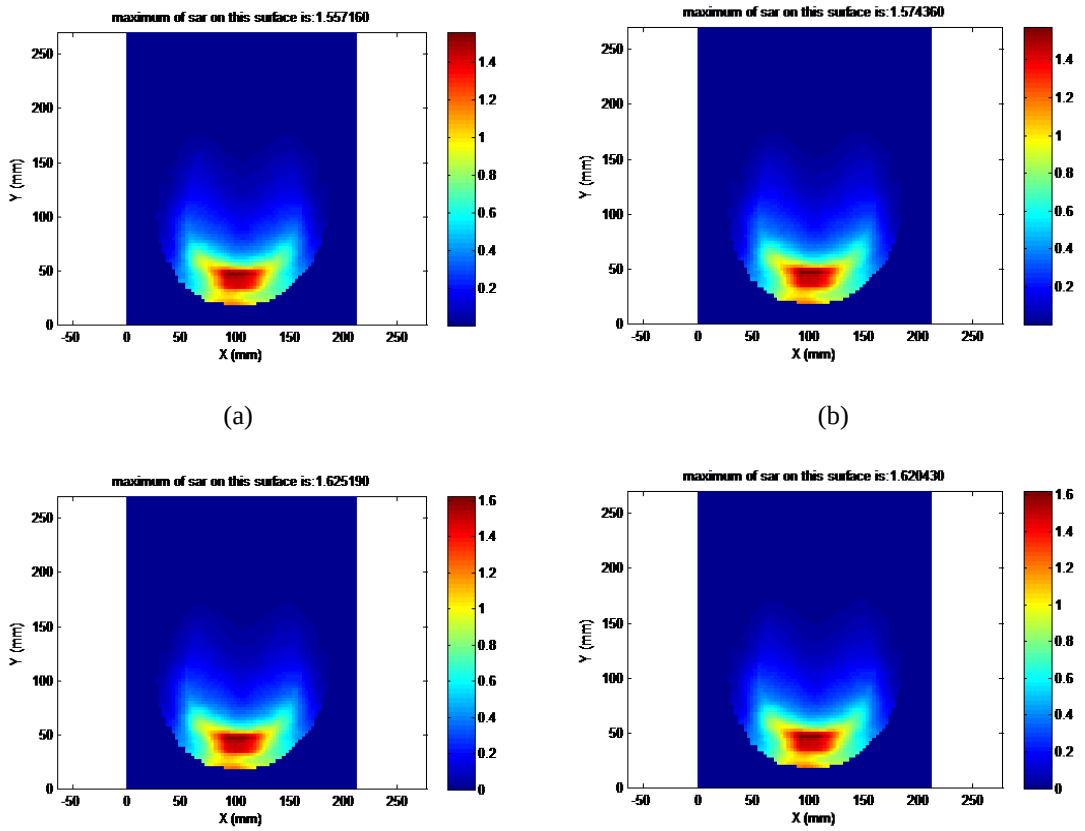

(a) (b)

(c) (d)

Figure 5.5 10g SAR distribution in human head (coil is on the back of the head). (a) Reference results; (b) Results of hybrid method with equivalent medium of (ε=36, σ=0.657); (c) Results of hybrid method with equivalent medium of (ε=50, σ=0.56); (d) Results of hybrid method with equivalent medium of (ε=50, σ=0.657). The transverse views are cut through the peak local SAR position. The color bar shows the 10g averaged local SAR as the result of 1 Watt RF power deposited in the human model. The unit is Watt/kg/Watt.

Table 5.2 Global peak 10g averaged local SAR position and value of posterior single loop coil simulated by using different media to obtain the Dirichlet boundary. The number in the parenthesis is the relative error.

	Reference	Medium 1 ε=36, σ=0.657	Medium 2 ε=50, σ=0.56	Medium 3 ε=50, σ=0.657
Maximum SAR position (x, y, z) (mm)	(93,45,183)	(93,45,183)	(93,45,183)	(93,45,183)
Maximum SAR value (W/kg)	1.557160	1.574360 (1.1%)	1.625190 (4.37%)	1.620430 (4.06%)

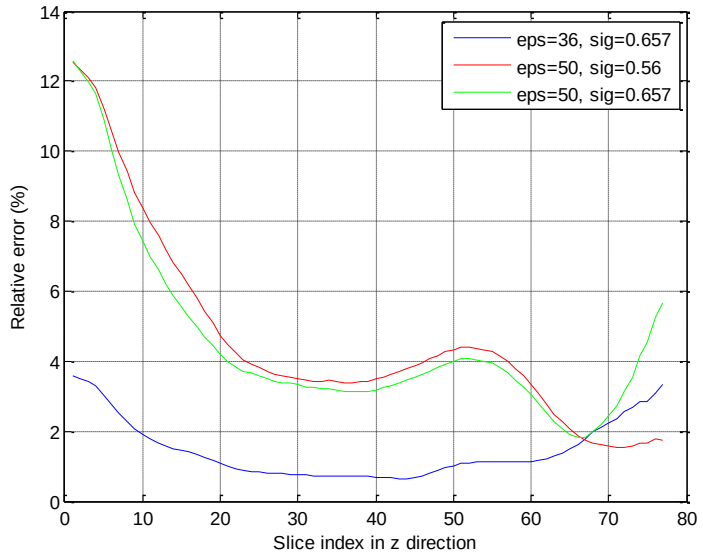

Figure 5.6 Relative error of local SAR of the posterior single coil on different transversal slices computed by using different media to provide the Dirichlet boundary. The slice indexed by 40 corresponds to the coil center.

5.3.2 Coil array with Dirichlet boundary

The accuracy for simulating an array of coils is studied by including two additional coils, one 7.8-cm above and the other 7.8-cm below the center coil, into the simulations. This three-loop array is positioned in the anterior and the posterior, respectively. Three different sets of phases are tested in each case. The phase shift between consecutive elements is 45°, 60°, and 90°, respectively. The equivalent medium used to provide the Dirichlet boundary has $\varepsilon_r = 36$ and $\sigma = 0.657$ S/m, which is the optimum value according to previous results.

The peak local SAR values of these phase-combined arrays on difference transversal slices are computed. Figure 5.7 (anterior) and Figure 5.8 (posterior) compare the relative errors between the conventional FDTD results and those obtained by using the equivalent medium and the Dirichlet boundary. The error is less than 5% on most slices. The global peak local SAR values and positions are compared in Table 5.3 (anterior) and Table 5.4 (posterior). It is observed that the relative error is consistently less than 2% in all cases. It is also observed

that the global peak SAR locations predicted by using different approaches are exactly the same for both the anteriorly and the posteriorly positioned array.

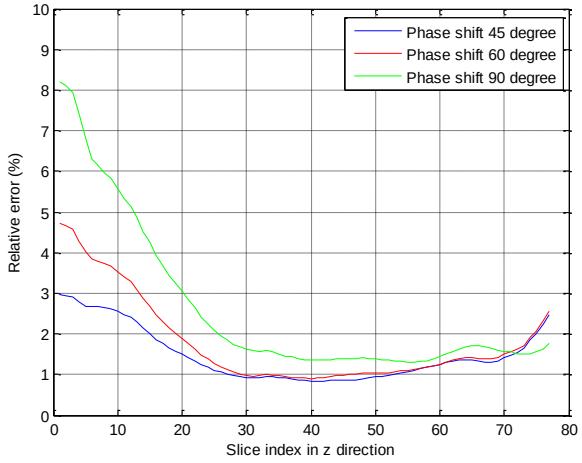

Figure 5.7 Relative error of local SAR of the three-loop array with different phase combinations placed in front of head on different transversal slices. The equivalent medium has ε_r= 36 and σ= 0.657 S/m. The slice indexed by 40 corresponds to the array center.

Table 5.3 Global peak 10g averaged local SAR position and value of a three-loop array with different phase combinations placed in front of the head. The equivalent medium has ε_r= 36 and σ = 0.657 S/m. The number in the parenthesis is the relative error.

Phase shift between adjacent coils(degree)	45		60		90	
	Reference	Dirichlet boundary	Reference	Dirichlet boundary	Reference	Dirichlet boundary
Maximum SAR position (x,y,z) (mm)	(147,204,147)	(147,204,147)	(147,204,147)	(147,204,147)	(135,213,126)	(135,213,126)
Maximum SAR value (W/kg)	1.033069	1.042582 (0.92%)	1.051616	1.062611 (1.05%)	1.356862	1.377571 (1.53%)

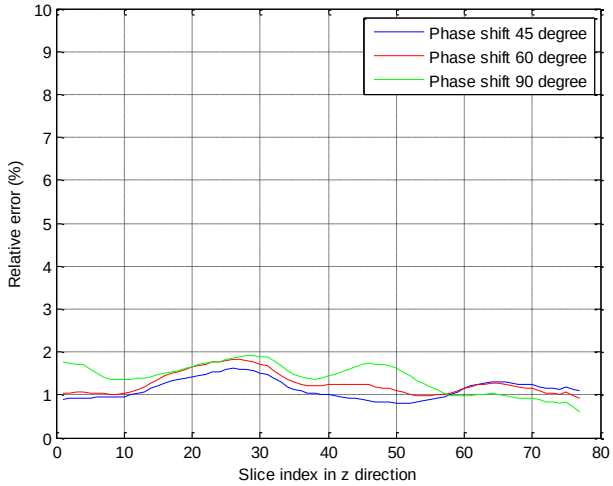

Figure 5.8 Relative error of local SAR of the three-loop array with different phase combinations placed on the back of head on different transversal slices. The equivalent medium has ε_r= 36 and σ= 0.657 S/m. The slice indexed by 40 corresponds to the array center.

Table 5.4 Global peak 10g averaged local SAR position and value of a three-loop array with different phase combinations placed on the back of the head. The equivalent medium has ε_r= 36 and σ = 0.657 S/m. The number in the parenthesis is the relative error.

Phase delay between adjacent coils(degree)	45		60		90	
	Reference	Dirichlet boundary	Reference	Dirichlet boundary	Reference	Dirichlet boundary
Maximum SAR position (x,y,z) (mm)	(93,54,201)	(93,54,201)	(99,66,213)	(99,66,213)	(81,42,165)	(81,42,165)
Maximum SAR value (W/kg)	1.088541	1.104105 (1.43%)	1.117242	1.133848 (1.49%)	1.371618	1.390966 (1.41%)

5.3.3 Hybrid method with TF/SF boundary

As we mentioned in section 5.2, tangential electromagnetic fields on the bounding surface can be injected into FDTD as incident field by TF/SF boundary. The single square coil in section 5.3.1 has been simulated by TF/SF approach. Figure 5.9 shows relative error on each transverse slice. Table 5.5 are positions and values of the global peak local SAR. The equivalent medium used here has ε_r= 36 and σ = 0.657 S/m. The relative errors are smaller than 1%.

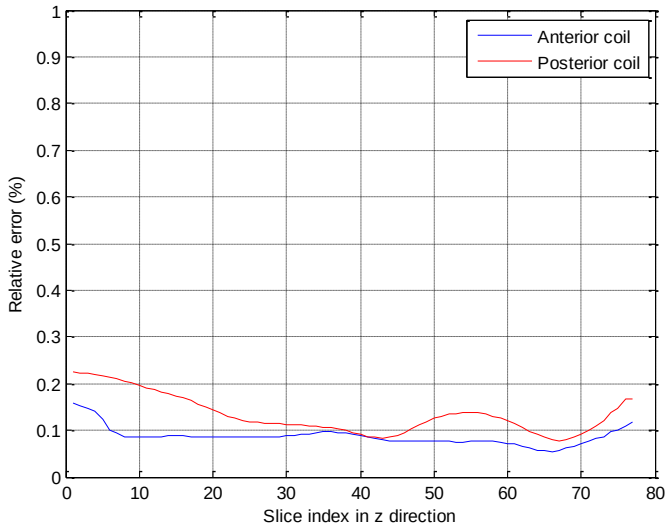

Figure 5.9 Relative error of local SAR of the anterior and posterior single coil on different transversal slices. The equivalent medium has ε_r= 36 and σ= 0.657 S/m and TF/SF approach is used.

Table 5.5 Global peak 10g averaged local SAR position and value of anterior and posterior single coil simulated with TF/SF approach. The equivalent medium has ε_r= 36 and σ = 0.657 S/m. The number in the parenthesis is the relative error.

Coil position	Anterior		Posterior	
	Reference	TF/SF boundary	Reference	TF/SF boundary
Maximum SAR position (x,y,z) (mm)	(147,204,147)	(147,204,147)	(93,45,183)	(93,45,183)
Maximum SAR value (W/kg)	1.245240	1.245952 (0.057%)	1.557160	1.559520 (0.15%)

The three-loop array in section 5.3.2 has also been simulated with TF/SF method. The relative errors on each transverse slice are shown in Figure 5.10 and the global peak SAR values are shown in Table 5.6. As we discussed in section 5.2, the relative error of TF/SF method is smaller than Dirichlet method. However it requires the PML absorbing boundary and the associated air buffer zone, so it is slower than Dirichlet method. In our experiments, TF/SF approach is approximated 6 times slower than Dirichlet method, but is still about 3.8 times faster than conventional FDTD.

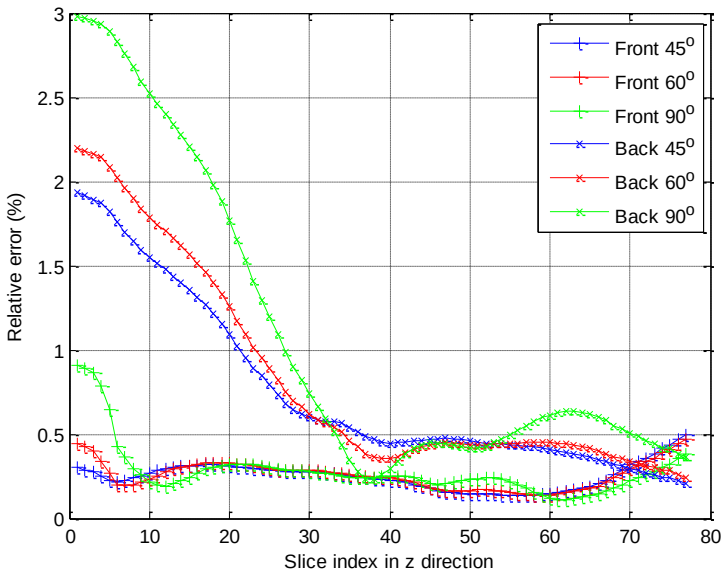

Figure 5.10 Relative error of local SAR of the three-loop array on different transversal slices with different phase combinations. The equivalent medium has ε_r= 36 and σ= 0.657 S/m and TF/SF approach is used.

Table 5.6 Global peak 10g averaged local SAR value of three-loop array with different phase combinations simulated with TF/SF approach. The equivalent medium has ε_r= 36 and σ = 0.657 S/m. The number in the parenthesis is the relative error.

	Reference	TFSF boundary
Anterior /45° phase shift	1.033069	1.031161(0.18%)
Anterior /60° phase shift	1.051616	1.049593(0.19%)
Anterior /90° phase shift	1.356862	1.354952(0.14%)
Posterior /45° phase shift	1.088541	1.083833(0.43%)
Posterior /60° phase shift	1.117242	1.112604(0.42%)
Posterior /90° phase shift	1.371618	1.368623(0.22%)

5.4 Conclusion remarks

A new hybrid technique is proposed for fast local SAR evaluations in high-field MRI. There are two stages in this hybrid method. In the first stage, coil/human coupling is resolved by MoM by approximating the human body as a uniform phantom. In the second stage, the boundary electric fields solved by MoM are used as the Dirichlet boundary condition in FDTD simulations of the electric fields inside the body. In order to obtain a good approximation, the permittivity and conductivity of the uniform phantom should be selected carefully. We have demonstrated that when ε=36, σ=0.657, the effect is optimal, relative error between phantom model and real head is less than 5%. All the results verify the validity of this phantom model.

In the first stage, the efficiency of the MoM can be improved by the Schur complement and dynamic matrix compression, it is demonstrated in [64] that the simulation time of a 32-element coil array on a single commodity CPU is less than 1 min. In the second stage, since the fields on the Dirichlet boundary is the result of coil resonance (with the head) resolved through the MoM, it no longer requires as many iterations as the conventional FDTD does. In addition, it eliminates the PML absorbing boundary. So it is much faster than conventional FDTD method.

Chapter 6 Statistical Simulation of SAR Variability by Using the Unscented Transform

6.1 Introduction

The specific absorption rate (SAR) is critical to the safety of radio frequency (RF) transmit coils [72]-[77][12]. Its evaluation is typically performed by full-wave numerical simulations with available human models that may represent the subject group of interest. Because the human anatomy can vary significantly [78, 79], the SAR also exhibits a certain degree of subject dependency. Besides, different subject positions and tissue properties may affect its value as well [74]. Therefore, a safety margin is required to prevent potential overheating of subjects who are different from the numerical models in simulations [74, 76].

The SAR variation has been investigated by different research groups in recent years. Tian et al computed the local SAR of a 3 Tesla (T) and 4T 16-rung unshielded birdcage coil by using six large, medium and small head models that were obtained by scaling the Hugo model [75]. Shajan et al considered three scaled head models with longitudinal shifts in the study of their 9.4T 16-channel transmit array [74]. It was reported that the 10-g local SAR varies by less than 10%. In the study of a 7T 16-rung shielded high-pass birdcage coil by Wolf et al, longitudinal shift was found to decrease the local SAR by 22%. At the same time, transversal shift affects the local SAR by $\pm$14% [12]. De Greef et al studied the local SAR variation of a 7T 8-channel brain imaging transmit array by using six different human models [76]. A safety margin of 1.4 was found appropriate to cover the worst-case scenario in their study. Ipek et al studied the local SAR variation of a 7T eight-channel prostate imaging transmit array by using four different human models [77]. It was found that the intersubject variability is large enough to invalidate the use of generic human models. Murbach et al [80] thoroughly studied the SAR variation of a 1.5T birdcage coil in different human body models,

at different positions, and with different tissue properties. The local SAR variation of 7T brain imaging coils caused by position changes was investigated in [12].

Because the variations of factors that may affect the SAR are random in nature, it is more appropriate to study the SAR in a statistical manner. In this way, the SAR can be considered as the output of a nonlinear transformation with multiple random input variables. A meaningful SAR limit can be established once its mean and standard deviation are known. Although different human models and subject positions have been considered in the aforementioned studies, SAR statistics, especially the standard deviation, have not been established and the worst-case scenario has no statistical meanings. In fact, conventional statistical simulation methods such as the Monte Carlo require a large number of random human models as its sample points [81]. Even if these models are available, their full-wave simulations can be quite time-consuming. Thus it is imperative to develop a statistical simulation procedure to address the SAR variability issue efficiently.

The approach explored here applies the unscented transform for SAR variability with respect to the probability distributions of multiple random input variables [82]-[85]. Instead of using a large number of random sample points, it only requires a few deterministic sample points to ensure good numerical accuracy. Besides sample point reduction, this method may also ease the difficulty of constructing a large number of human models that satisfy the statistical distributions of anatomical features [86].

6.2 Unscented Transform

Details of the unscented transform can be found in literatures [82]-[85]. Here we apply it to analyze the SAR variability. Consider at first the SAR as a nonlinear transformation of one input variable x with mean μ_x. The nonlinear transformation can be written in terms of a zero-mean univariate random variable $u = x - \mu_x$ as:

$$y = f(x) = f(\mu_x + u) \tag{6.1}$$

The mean and standard deviation of y can be computed by using N so-called sigma points $(u_1 \dots u_n)$ with nonnegative weights $(w_1 \dots w_n)$ as follows:

$$\mu_y = w_0 f(\mu_x) + \sum_{i=1}^{N} w_i f(\mu_x + u_i) \tag{6.2}$$

$$\sigma_y^2 = w_0 \left[f(\mu_x) - \mu_y\right]^2 + \sum_{i=1}^{N} w_i [f(\mu_x + u_i) - \mu_y]^2 \tag{6.3}$$

These sigma points and weights are determined by matching the first 2N central moments with those of U. As a result, only three sigma points, $-\sqrt{3}\sigma_x$, 0, $\sqrt{3}\sigma_x$ with weights 1/6, 2/3, 1/6, where σ_x is the standard deviation of input variable x, are required to get an approximation that is second-order accurate[84].

The extension of the unscented transform to multivariate case is straightforward. Suppose the SAR is a nonlinear transformation of a p-dimensional multivariate random vector, N p-dimensional sigma points can be used with appropriate weights to calculate its mean and standard deviation. In a p-dimensional parametric space where each axis is normalized by the standard deviation of the corresponding input variable, we can choose 2^p points in a cube and 2p points on the axes together with the origin, i.e., $N = 2^p + 2p + 1$. The location and weights of the first group of points are given by:

$$(\pm 1, \pm 1, \dots \pm 1)\sqrt{\frac{p+2}{p}}, \qquad w = \frac{p^2}{2^p(p+2)^2} \tag{6.4}$$

The location and weights of the second group of points are given by:

$$(0 \dots 0, \pm 1, 0 \dots 0)\sqrt{p+2}, \qquad w = \frac{1}{(p+2)^2} \tag{6.5}$$

The weight of the origin is given by $w = (2p + 4)/(p + 2)^2$ [23]. It should be noted that the locations of these sample points are deterministic rather than random. The normalized sigma points and their weights up to 6 variables are shown in Table 6.1.

The sensitivity of the SAR can be studied by examining its marginal standard deviation with respect to each input variable [87], which is treated by the unscented transform as individual univariate cases [84]. More specifically, three sigma points are applied with respect to the mean and standard deviation of each input variable (Table 6.1), while other input variables are set at their mean values. For p input variables, this requires 3p additional numerical simulations, which is an insignificant overhead in general.

Table 6.1 Normalized sigma points and their weights.

	Number of sigma points	Normalized sigma points	Weights
One variable	2	$\pm\sqrt{3}$	1/6
	1	0	2/3
Two variables	4	$(\pm\sqrt{2}, \pm\sqrt{2})$	1/16
	4	$(\pm 2, 0), (0, \pm 2)$	1/16
	1	0	1/2
Three variables	8	$(\pm 1, \pm 1, \pm 1)\sqrt{5/3}$	9/200
	6	$(0, \pm 1, 0)\sqrt{5}$	1/25
	1	0	2/5
Four variables	16	$(\pm 1, \pm 1, \pm 1, \pm 1)\sqrt{3/2}$	1/36
	8	$(0, \dots, \pm 1, \dots 0)\sqrt{6}$	1/36
	1	0	1/3
Five variables	32	$(\pm 1, \pm 1, \dots \pm 1)\sqrt{7/5}$	25/1568
	10	$(0, \dots, 0, \pm 1, 0 \dots 0)\sqrt{7}$	1/49
	1	0	2/7
Six variable	64	$(\pm 1, \pm 1, \dots \pm 1)\sqrt{4/3}$	9/1024
	12	$(0, \dots, 0, \pm 1, 0 \dots 0)2\sqrt{2}$	1/64
	1	0	1/4

6.3 Simulation examples

The FDTD method implemented on Nvidia Tesla C2050 GPU is applied in the following electromagnetic simulation. In all simulations, 10 layers of perfectly-matched layer (PML) are applied as the absorbing boundary with a 10-cell buffer zone from each side of the numerical model. Each coil is tuned to 297 MHz at first by adjusting its capacitor values until

the input reactance at the feeding point became zero. Subsequent simulations are performed by using a 1-Volt voltage source with a 50-Ohm internal resistance. The number of time steps is long enough for the FDTD to converge to a steady state. The 10-g averaged local SAR is calculated and normalized by the total RF power deposition in the corresponding human model. It is found that changing the source internal resistance will affect the convergence rate of the FDTD, not the local SAR results normalized by power deposition.

6.3.1 Local SAR of a 7T spine coil

The variability of the 10-g local SAR of a 10-cm square loop coil for spine imaging with respect to tissue property changes is studied. The coil is fixed at 2-cm away from the human model and numerically tuned with three capacitors (Figure 6.1). Here the Hugo model with a 5-mm isotropic spatial resolution and truncated around the waist is applied. The entire simulation domain consists of $230 \times 155 \times 210$ voxels. All tissues of the Hugo model are included except for the nail and the testicle. The average values of the dielectric property and density of each tissue are determined according to [71]. A 10% standard deviation is introduced to the dielectric properties and densities of 16 tissues that are in a close range to the coil. These include blood, blood vessel, body fluid, cancellous bone, cortical bone, bone marrow, fat, glands, heart, ligament, inner lung, outer lung, lymph, muscle, spine, and skin. Properties of tissues that are far away from the coil, e.g., small intestine and gray matter, have constant values in all simulations. Thus the statistical model consisted of 48 random input variables. Figure 6.1(a) shows the coil and human model, (b) is the 10g SAR distribution on transverse plane.

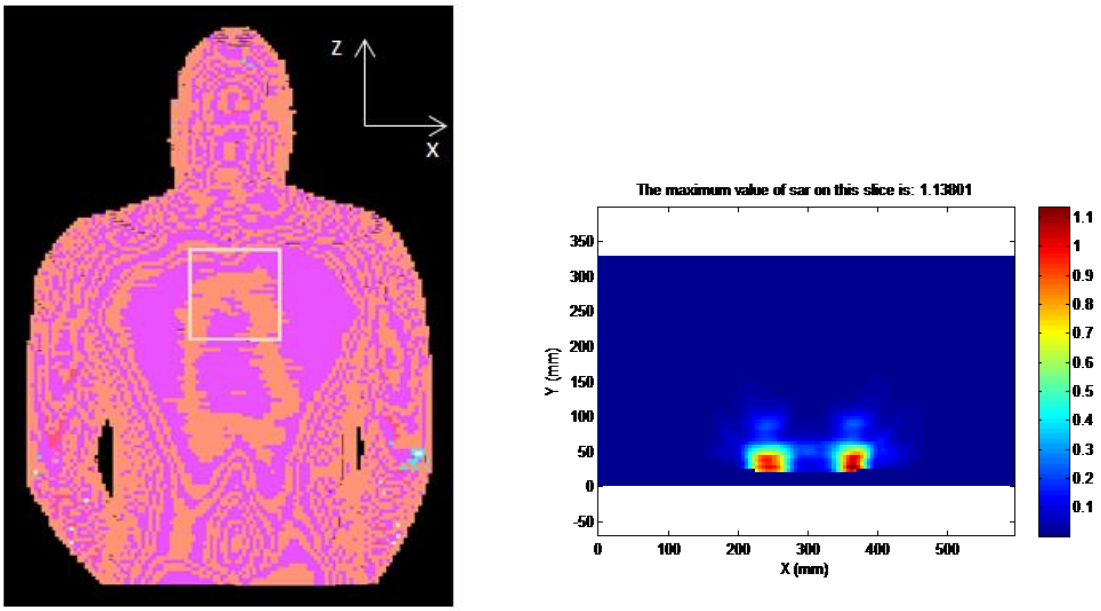

(a) (b)

Figure 6.1 (a) Square loop spine coil and human model; (b) 10g SAR distribution on transverse plane. The SAR is scaled to 1W RF power deposited in the human body, the unit is Watt/kg/Watt.

Table 6.2 The most significant input variables as the result of sensitivity analysis.
Top row: tissue properties ranked by their significance to the 10-g local SAR of the spine coil.
Second row: marginal variability of the 10-g local SAR with respect to the most significant variables.
Third row: the variability of the 10-g local SAR when different numbers of most significant input variables are included in multivariate models. For instance, the fourth column corresponds to the variability when the multivariate model consisted of the first three most significant input variables. The fifth column corresponds to the variability when the multivariate model consisted of the first four most significant input variables.
Fourth row: the reference variability obtained by the Monte Carlo method with 1500 sample points in each case.

	Muscle density	Muscle conductivity	Fat density	Skin density	Muscle permittivity	Skin conductivity
Marginal variability(%)	4.8	4.6	2.6	2.3	1.8	1.4
Multivariate variablility(%)	4.8	6.7	7.3	7.7	7.8	7.9
Reference(%)	5.0	6.9	7.2	(N/A)	(N/A)	(N/A)

A sensitivity analysis is performed at first to study the impact of each input variable. The most significant ones are listed in Table 6.2. The variability in the table is defined as the standard deviation (SD) -to-mean ratio. Next, the unscented transform is applied to study the variability of the 10-g local SAR by progressively adding more significant input variables into multivariate models. In the first batch of simulations, only the most significant variable, i.e., muscle density, is included in the statistical model. In the second batch of simulations,

the first two most significant random variables, i.e., muscle density and conductivity, are included. This iterative procedure converged after the first four most significant input variables are included in the multivariate model. (Table 6.2 and Figure 6.2). The mean and SD of the 10-g local SAR is found to be 1.38 and 0.11 Watt/kg/Watt, respectively.

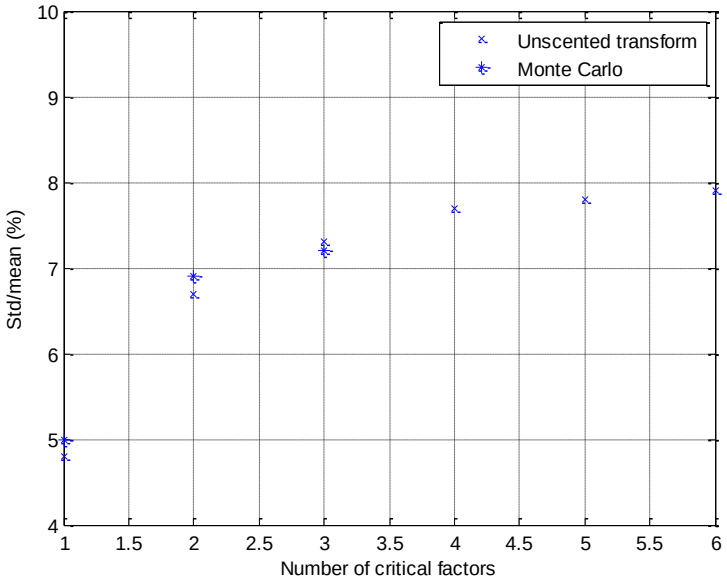

Figure 6.2 The variability of the 10-g local SAR of the spine coil versus the number of significant input variables in the statistical model computed by the unscented transform and the Monte Carlo method with 1500 sample points, respectively.

6.3.2 Local SAR of a 7T 16-channel transmit array

In this example, the Duke model with a 3-mm isotropic spatial resolution and truncated around the chest is applied as the template for model transformations. Tissue properties are specified according to literatures [71]. Six geometric variables are considered for demonstration purposes. They include head breadth (mean=154 mm; SD=6 mm), head length (mean=199 mm; SD=7 mm), shift along the z-direction (mean=0 mm; SD=15 mm), rotations around the x- (left-to-right; mean=0°; SD=5°), the y- (posterior-to-anterior; mean=0°; SD=5°), the z-direction (mean=0°; SD=5°). The statistics of the head length and breadth correspond to those of Caucasians [79]. When z = 0, the midpoint between the innermost points of the eyes aligns with the coil center in the longitudinal direction. The geometric center of the standard

model on the transverse plane, which corresponds to the origin of the p-dimensional parametric space, aligns with that of the coil.

Generating the sigma points that correspond to different head breadths and lengths are accomplished by scaling the head in the x- and y-direction. The same spatial resolution is maintained by projecting pixels in the scaled head model back to the template model. Rotations along the three axes are performed by multiplying the coordinates of all voxels of the Duke template above the throat with the following three basic rotation matrices:

$$R_x(\theta) = \begin{bmatrix} 1 & 0 & 0 \\ 0 & cos\theta & -sin\theta \\ 0 & sin\theta & cos\theta \end{bmatrix} R_y(\theta) = \begin{bmatrix} cos\theta & 0 & sin\theta \\ 0 & 1 & 0 \\ -sin\theta & 0 & cos\theta \end{bmatrix} R_z(\theta) = \begin{bmatrix} cos\theta & -sin\theta & 0 \\ sin\theta & cos\theta & 0 \\ 0 & 0 & 1 \end{bmatrix} \quad (6.6)$$

When rotating around the z-direction, the pivot-axis goes through the geometric center of the anatomy on the slice that cuts through the throat. When rotating around the x- and y-direction, the pivot-axis goes through the furthest point in the direction toward which the head leans. The base of the rotated part is swept incrementally to fill the gap between the rotated and the stationary parts (Figure 6.3). The three basic rotation matrices were combined as $R = R_x(\theta_x)R_y(\theta_y)R_z(\theta_z)$ for arbitrary rotations.

(a) (b)

Figure 6.3 (a) The head rotates along x-axis; (b) The base of the rotated part is swept incrementally to fill the gap between the rotated and the stationary parts.

The 10-g local SAR of a 16-channel shielded transmit array caused by six geometric variations is examined. The array has two rows of loop coils. The inner diameter of this array is 28.75 cm and the height is 25 cm. There is a shield surrounding the coil array, the model is shown in Figure 6.4(a). The entire simulation domain for each model consists of 230 ×155 ×210 voxels. The simulated electromagnetic fields are combined with 45° progressive phase shift to achieve a circularly polarized transverse magnetic field. A sensitivity analysis is performed and the geometric variations ranked by their significance are longitudinal shift, head breadth, head length, rotation along y-axis, rotation along z-axis and rotation along x-axis. The mean and standard deviation of the 10-g local SAR are determined by using 77 sigma points (for six input variables). They are 0.68 and 0.07 Watt/kg/Watt, respectively. Some of the combined B_1^+ and local SAR maps are illustrated in Figure 6.4-Figure 6.8, the color bar shows B_1^+ and 10g-averaged local SAR as the result of 1W RF power deposited in the human body. The unit of B_1^+ is μT and for SAR is Watt/kg/Watt. In Figure 6.4-6.8, for B_1^+ map, the sagittal views are cutting through the same symmetric plane of the human body and the transverse views are adjusted so that they cut through the eyes; for SAR map, the sagittal views and transverse views are adjusted so that they all cut through the peak local SAR location.

6.4 Discussions

6.4.1 Safety Margin

A meaningful safety margin can be determined once SAR statistics are available. In the first example, setting the 10-g local SAR limit to be three-sigma above its mean, i.e., 1.71 Watt/kg/Watt, can cover 93.3% of the cases. Setting it to be six-sigma above its mean, i.e., 2.04 Watt/kg/Watt, can cover nearly all cases. In the 16-channel transmit array example, the 10-g local SAR limit can be six-sigma above its mean, i.e., 1.1 Watt/kg/Watt, to cover the worst-case scenario of all situations being examined. Without knowing SAR statistics, the

safety margin may be either overestimated or underestimated. Both will result in nonoptimal use of RF coils.

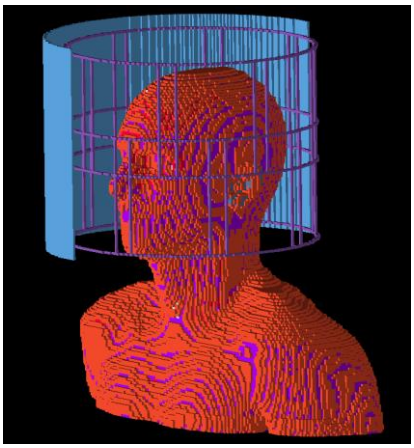

(a)

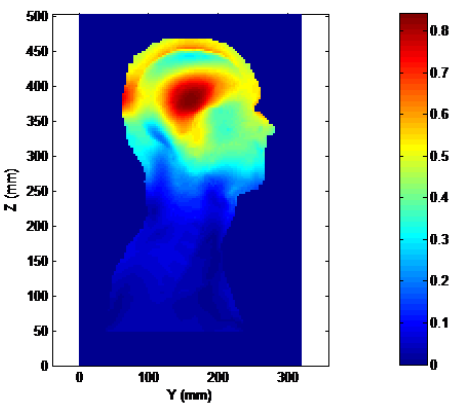

(b)

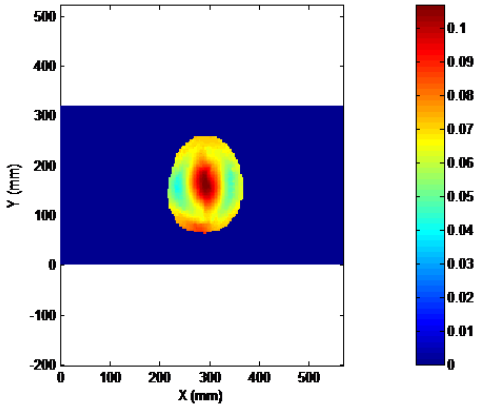

(c)

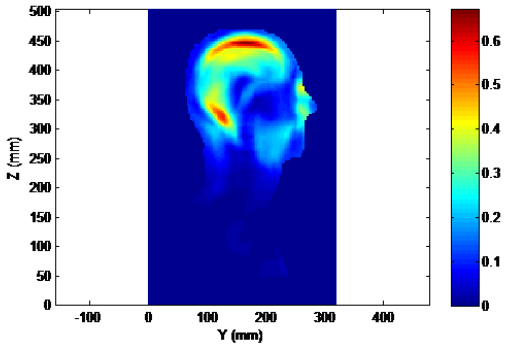

(d)

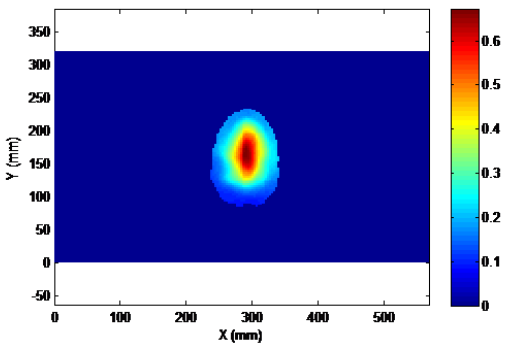

(e)

Figure 6.4 (a) Standard human model; (b)(c) B_1^+ field distribution on sagittal and transverse plane; (d)(e) 10g-averaged local SAR distribution on sagittal and transverse plane. The color bar shows B_1^+ and 10g-averaged local SAR as the result of 1W RF power deposited in the human body. The unit for B_1^+ is μT and for SAR is Watt/kg/Watt.

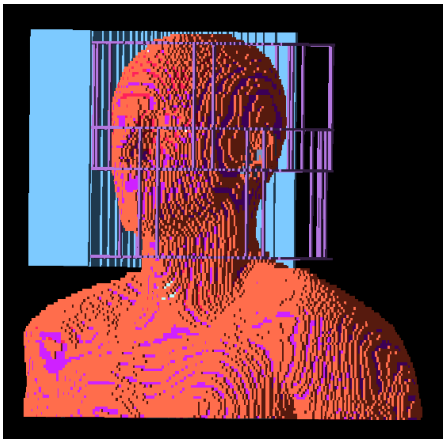

(a)

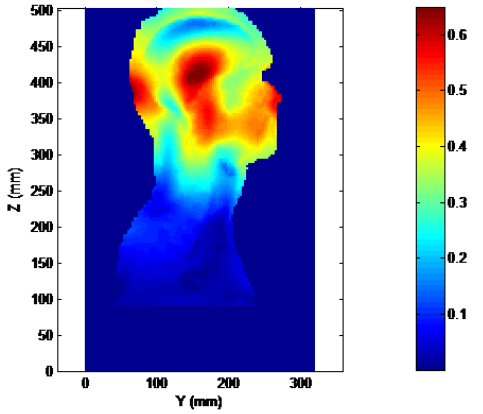

(b)

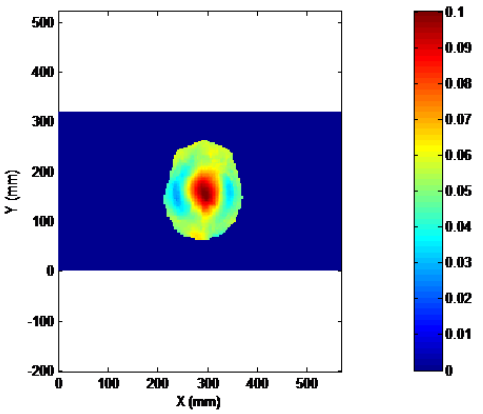

(c)

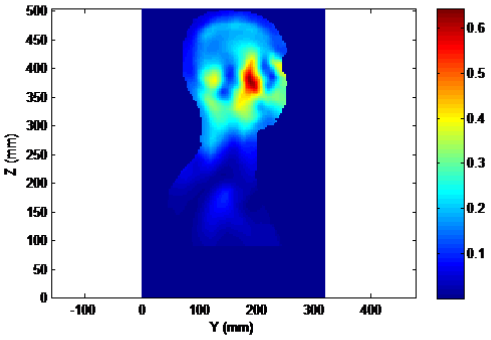

(d)

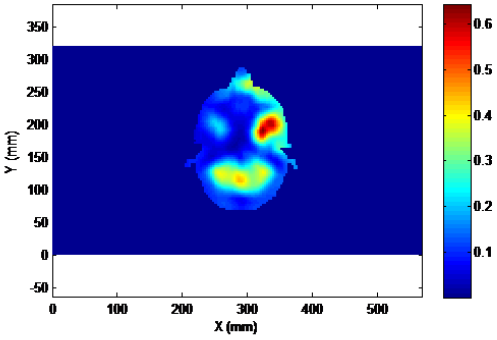

(e)

Figure 6.5 (a) The human model shifts in z-direction by 42.4 mm; (b)(c) B_1^+ field distribution on sagittal and transverse plane; (d)(e) 10g-averaged local SAR distribution on sagittal and transverse plane. The color bar shows B_1^+ and 10g-averaged local SAR as the result of 1W RF power deposited in the human body. The unit for B_1^+ is μT and for SAR is Watt/kg/Watt.

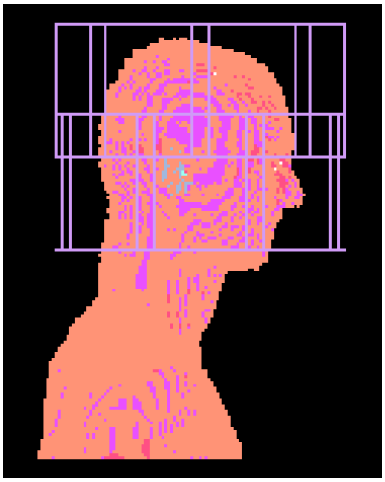

(a)

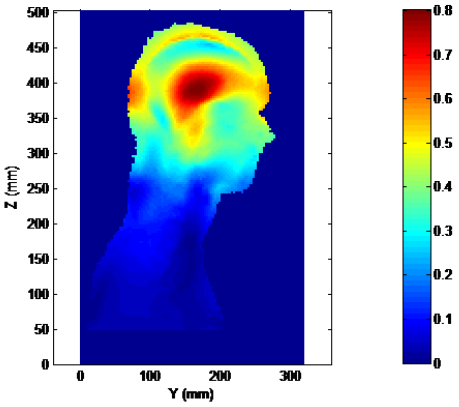

(b)

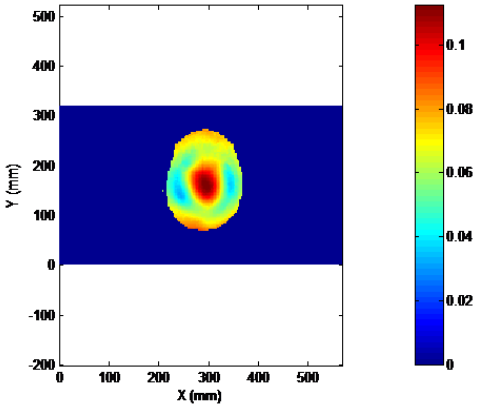

(c)

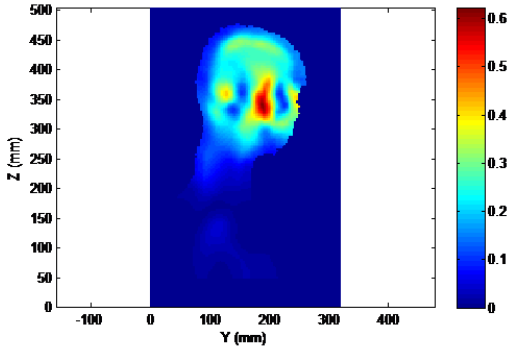

(d)

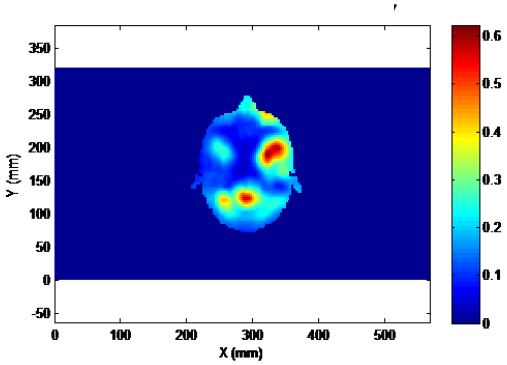

(e)

Figure 6.6 (a) The human model rotates alone x-axis by 14.1°; (b)(c) B_1^+ field distribution on sagittal and transverse plane; (d)(e) 10g-averaged local SAR distribution on sagittal and transverse plane. The color bar shows B_1^+ and 10g-averaged local SAR as the result of 1W RF power deposited in the human body. The unit for B_1^+ is μT and for SAR is Watt/kg/Watt.

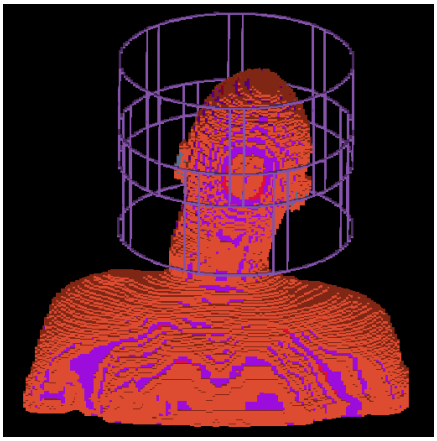

(a)

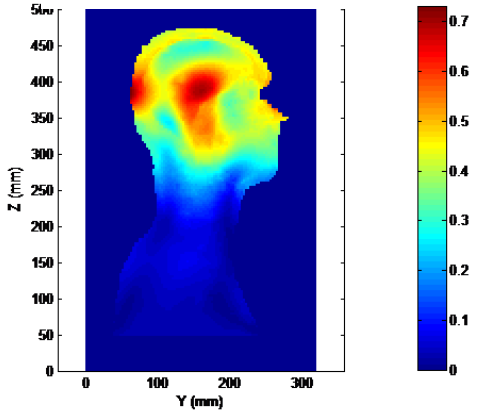

(b)

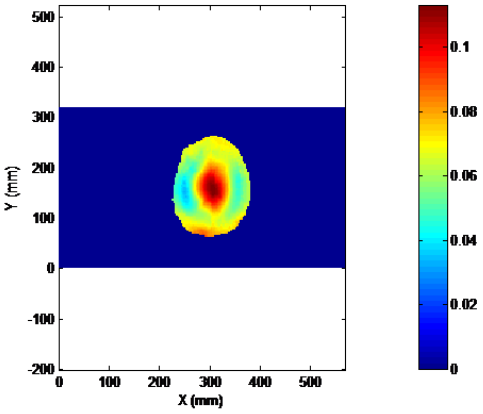

(c)

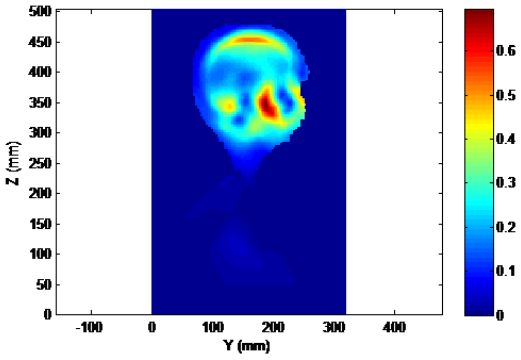

(d)

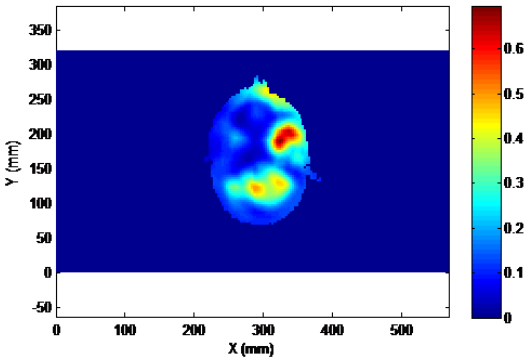

(e)

Figure 6.7 (a) The human model rotates alone y-axis by 14.1°; (b)(c) B_1^+ field distribution on sagittal and transverse plane; (d)(e) 10g-averaged local SAR distribution on sagittal and transverse plane. The color bar shows B_1^+ and 10g-averaged local SAR as the result of 1W RF power deposited in the human body. The unit for B_1^+ is μT and for SAR is Watt/kg/Watt.

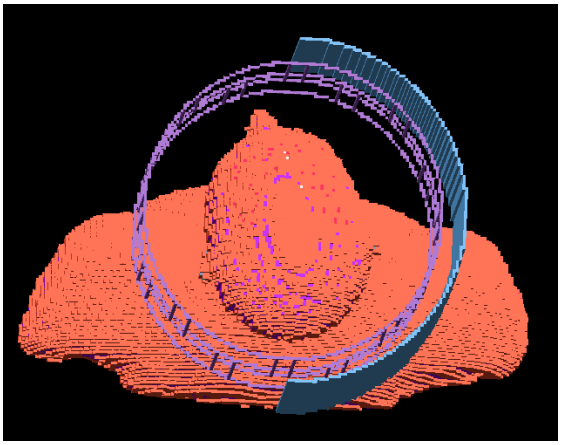

(a)

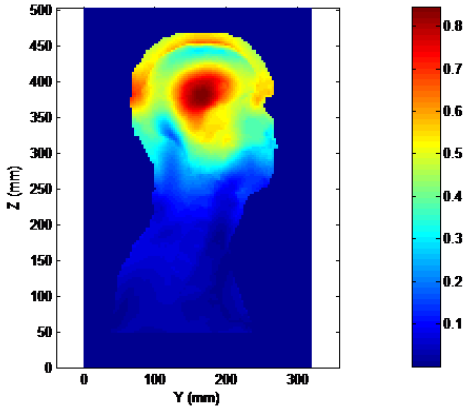

(b)

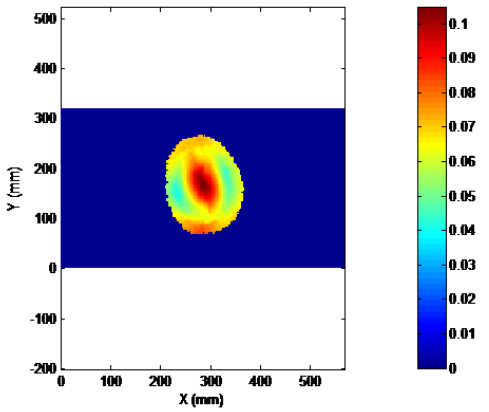

(c)

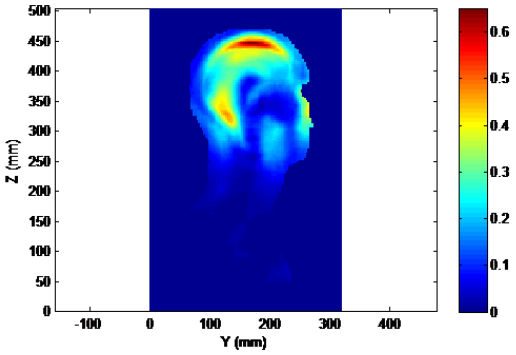

(d)

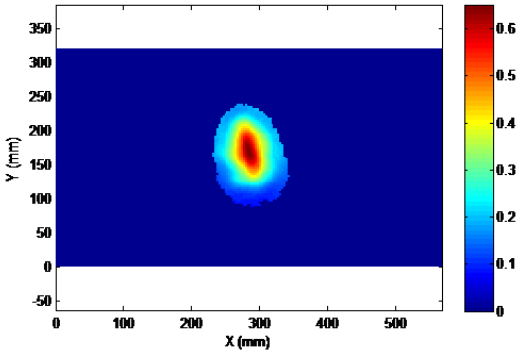

(e)

Figure 6.8 (a) The human model rotates alone z-axis by 14.1°; (b)(c) B_1^+ field distribution on sagittal and transverse plane; (d)(e) 10g-averaged local SAR distribution on sagittal and transverse plane. The color bar shows B_1^+ and 10g-averaged local SAR as the result of 1W RF power deposited in the human body. The unit for B_1^+ is μT and for SAR is Watt/kg/Watt.

6.4.2 Sample point reduction

The first example demonstrates the accuracy and efficiency of the unscented transform. The local SAR variability calculated by the unscented transform with the first one, two, and three most significant input variables are nearly identical to those calculated by the Monte Carlo method with 1500 random sample points (Table 6.2). The convergence of the Monte Carlo method appears to be slow and nonsmooth, which makes the use of a large number sample points necessary even if only one input variable is examined. This can be quite inefficient for sensitivity analysis. The practical sample point reduction ratio depends on how many random input variables are included in the statistical model and how confident one feels about the accuracy of the Monte Carlo method.

6.4.3 Sensitivity Analysis

The sensitivity analysis is especially useful in RF safety studies. First of all, it can reduce the computational complexity of statistical simulations. As demonstrated in the first example, input variables can be added one by one according to their significance in multivariate statistical models until the SAR variability converges. If all input variables are considered together, the statistical model may become too complicated to handle. Secondly, it provides a practical means of reducing the local SAR variability, and, therefore, improving the safety by decreasing the SAR margin. In the second example, the local SAR of the 16-channel array is most sensitive to longitudinal head shift, which may be understood because a virtual ground needs to be formed on the symmetric plane of the array in the longitudinal direction, and least sensitive to rotations, which may be understood because the head is approximately a sphere. Thus the local SAR variability can be reduced if the longitudinal head shift is restricted. On the contrary, using fixation devices to restrict head rotations appears to be least effective because the variations of anatomical features, which are difficult to control, have a more significant impact on local SAR variability.

6.4.4 Random input variables

This study provides a general framework of using the unscented transform for SAR variability studies. Which factor should be included in the statistical model is problem dependent. Naturally all physical and physiological parameters exhibit some degree of randomness. A brute force approach would be performing sensitivity analysis to all imaginable parameters and include them one by one in multivariate statistical models. Alternatively, several parameters can be excluded by physical intuitions. For instance, the properties of the brain and small intestine were assumed constant in the first example because they are far away from the spine coil. Subject positions were not treated as random variables because they are fixed when subjects lying on a spine coil. In the second example, the longitudinal head shift, which is the most significant factor, may also be excluded from the statistical model if it can be restricted. It is a good strategy in general to exclude parameters that will obviously not affect the SAR from the statistical model and perform sensitivity analysis to questionable ones.

The unscented transform is purely mathematical. The input variables are not limited to those presented in this study. For instance, the shape of the skull and the fat content of the human head, which may have a more significant impact on the local SAR, can be studied in the same manner. They were not included in this study due to the lack of their parameterized models and statistics. At the same time, geometric and tissue property variations can be studied together because they are uncorrelated. More research will be performed in the future to demonstrate the advantages of the proposed method in these cases.

Chapter 7 Summary and Conclusion

In MRI application, SAR is an important safety concern. The RF power deposition and SAR level have a significant impact on RF coil and pulse design. MRI is moving toward high B_0 field nowadays, which leads to a high SAR level and high temperature increasing, especially when it comes to metallic medical implants. In high field MRI, multichannel RF transmission is widely used to mitigate B_1 field inhomogeneity. A specific B_1 can be generated by adjusting the magnitude, phase and pulse shape of each coil. The dynamic changing of transmission will result in a subject dependent SAR distribution. Therefor we need to evaluate SAR in real subjects in real time. In addition, because the SAR is subject dependent, we need to investigate a large number of samples to get the statistical character of SAR. However, SAR evaluation requires full-wave electromagnetic simulation, which is time-consuming. So it is necessary to develop fast SAR evaluation methods. This dissertation presents some approaches to fast estimate the SAR in human body during MRI scan.

In Chapter 1, a brief description of the MRI principle is given. The static B_0 field, RF B_1 field, RF coil and SAR are introduced. We discuss the process of how the MRI signal is generated and received and point out that the SNR of MRI is proportional to the strength of B_0. However high B_0field will make B_1 field inhomogeneous and increase SAR level. The regulatory limits suggested by FDA and IEC are presented and the previous contributions made by other research groups are briefly reviewed.

Chapter 2 presents the fundamental theory of FDTD method, which includes the Yee cell, updating equations, PML absorbing boundary, voltage source, current source and plane wave source. The time step and spatial resolution, the stability condition and numerical dispersion are also presented. To verify the validity of the program, plane wave scattering by a dielectric sphere is investigated. The analytical solution to this problem is derived and compared with FDTD simulation results, a good agreement between them is obtained.

Chapter 3 discusses the topic of GPU acceleration of FDTD. GPU architecture and memory hierarchy are briefly introduced and the CUDA parallel programing model is presented. With GPU, FDTD algorithm can be executed by hundreds of cores in parallel. We develop a parallel code for FDTD on GPU and compare its performance with sequential code on CPU. To improve efficiency, a large block size should be applied to increase the occupancy and the on-chip shared memory should be utilized as much as possible. A birdcage coil is simulated as an example, from which we can conclude that as the frequency increases, B_1^+ field becomes inhomogeneous and E field increases.

In Chapter 4, the definition of point SAR, N-gram averaged SAR and global SAR are presented and the calculation algorithm is given. Then the temperature distribution is evaluated with local SAR by using bio-heat equation, the updating equation is derived. A high resolution human model is described. The electric and thermal parameters of human tissues are listed. The birdcage coil with human model is studied at different frequency. The 10g SAR, 1g SAR, point SAR distribution and temperature increasing in human head are presented. We can conclude the SAR and temperature increase with frequency.

In Chapter 5, a rapid local SAR estimation method is developed. It is a hybrid technique that combines method of moments (MoM) and FDTD. In first step, MoM is used to solve the strong coil/body coupling in frequency domain and obtain the fields on an imaginary surface surrounding the human body. Then these fields are injected into FDTD simulation by treating them as Dirichlet boundary condition. Validation and simulation example are presented.

Chapter 6 presents a simulation procedure based on the unscented transform method. Instead of using a large number of random sample points, a few weighted deterministic sigma points are applied for accurate SAR statistics. Sensitivity analysis is performed to identify significant factors to be included in multivariate statistical models. As a result, a meaningful safety margin can be established efficiently and RF coil safety may be improved by possible

elimination of significant input variables. As examples, the local SAR variability as the result of tissue property and geometric changes are examined respectively.

The methods presented in this dissertation will be helpful to the coil design and SAR monitoring in MRI practice. Based on the work of this dissertation, some recommendations are presented for the future research: (1) FDTD algorithm has been implemented on single GPU. However the memory of single GPU is limited, future work can be done to implement FDTD on multi GPU cluster; (2) In the MoM and FDTD hybrid technique, an optimal equivalent medium has been proposed for brain. This method can also be applied to body imaging, future research can focus on identifying the optimal equivalent medium to approximate the human body; (3) In the statistical simulation, some geometric and tissue property variations are investigated in the dissertation. The proposed method is general and more factors that may affect SAR can be examined in the same manner; (4) Based on the B_1^+ field, the transverse magnetization can be calculated by solving Bloch equation. Proper composite RF pulse can be designed to produce homogeneous transverse magnetization. This should be an interesting topic in future research.

Reference

[1] Jerry L. Prince and Jonathan M. Links. Medical Imaging Signals and Systems. Pearson Prentice Hall, Pearson Education, Inc., Upper Saddle River, New Jersey, 2006.

[2] Jianming Jin. Electromagnetic Analysis and Design in Magnetic Resonance Imaging. CRC Press LLC, 1999.

[3] Center for Devices and Radiologic Health. Guidance for the submission of premarket notification for magnetic resonance diagnostic devices. Food and Drug Administration, 1998.

[4] International Electrotechnical Commission. International standard, medical equipment-part 2: particular requirements for safety of magnetic resonance equipment for medical diagnosis, 2nd revision. International Electrotechnical Commission, 2002.

[5] International Electrotechnical Commission. IEC Standard 60601-2-33. Particular requirements for the safety of magnetic resonance equipment for medical diagnosis. International Electrotechnical Commission, 2002.

[6] Martino Grandolfo, Paolo Vecchia and Om P. Gandhi. Magnetic resonance imaging: calculation of rates of energy absorption by a human-torso model. Bioelectromagnetics 11: 117-128, 1990.

[7] Christopher M. Collins, Shizhe Li, Qing X. Yang and Micheal B. Smith. A method for accurate calculation of B1 fields in three dimensions: effects of shield geometry on field strength and homogeneity in the birdcage coil. Journal of Magnetic Resonance 125, 233-241, 1997.

[8] Ji Chen, Zhaomei Feng and Jian-Ming Jin. Numerical simulation of SAR and B1-field inhomogeneity of shielded RF coils loaded with the human head. IEEE Transactions on Biomedical Engineering, Vol. 45, NO. 5, May 1998.

[9] Shumin Wang and Jeff H Duyn. Analysing radio-frequency coil arrays in high-field magnetic resonance imaging by the combine field integral equation method. Phys. Med. Biol. 51, 3211-3229, 2006.

[10] Shumin Wang and Jeff H Duyn. Time-domain finite-difference/ finite-element hybrid simulations of radio frequency coils in magnetic resonance imaging. Phys. Med. Biol. 53, 2677-2692, 2008.

[11] Shumin Wang. Quasi-Block-Cholesky factorization with dynamic matrix compression for fast integral-equation simulations of large-scale human body models. Proceedings of the IEEE, Vol. 101, NO. 2, February 2013.

[12] S. Wolf, D. Diehl, M. Gebhardt, J. Mallow and O. Speck. SAR simulations for High-field MRI: How much detail, effort, and accuracy is needed? Magnetic Resonance in Medicine 69: 1157-1168, 2013.

[13] Christopher M. Collins. Calculations of RF magnetic fields and SAR experienced by the human body during MRI. PhD dissertation, University of Pennsylvania, 1999.

[14] Arslan Amjad. Specific absorption rate during magnetic resonance imaging. PhD dissertation, Purdue University, 2007.

[15] Tamer S. lbrahim and Lin Tang. Insight into RF power requirements and B_1 field homogeneity for human MRI via rigorous FDTD approach. Journal of Magnetic Resonance Imaging 25: 1235-1247, 2007.

[16] Zhangwei Wang, James C. Lin, Weihua Mao, Wanzhan Liu, Michael B. Smith and Christopher M. Collins. SAR and temperature: simulations and comparison to regulatory limits for MRI. Journal of Magnetic Resonance Imaging 26: 437-441, 2007.

[17] Esra Neufeld, Marie-Christine Gosselin, Manuel Murbach, Andreas Christ, Eugenia Cabot and Niels Kuster. Analysis of the local worst-case SAR exposure caused by an MRI multi-transmit body coil in anatomical models of the human body. Phys. Med. Biol. 56, 4649-4659, 2011.

[18] Hanno Homann, Ingmar Graesslin, Holger Eggers, Kay Nehrke, Peter Vernickel, Ulrich Katscher, Olaf Dossel and Peter Bornert. Local SAR management by RF Shimming: a simulation study with multiple human body models. Megn. Reson. Mater. Phy. 25: 193-204, 2012.

[19] Christopher M. Collins, Wanzhan Liu, Jinghua Wang, Rolf Gruetter, J. Thomas Vaughan, Kamil Ugurbil and Michael B. Smith. Temperature and SAR calculations for a human head within volume and surface coil at 64 and 300 MHz. Journal of Magnetic Resonance Imaging 19: 650-656, 2004.

[20] Astrid L.H.M.W. van Lier, Alexis N.T.J. Kotte, Bas W. Raaymakers, Jan J.W. Lagendijk and Cornelis A.T. van den Berg. Radiofrequency heating induced by 7T head MRI: thermal assessment using discrete vasculature or Pennes' bioheat equation. Journal of Magnetic Resonance Imaging 35: 795-803, 2012.

[21] Aurelien Massire, Martjin A. Cloos, Michel Luong, Alexis Amadon, Alexandre Vignaud, Christopher J. Wiggins and Nicolas Boulant. Thermal simulations in the human head for high field MRI using parallel transmission. Journal of Magnetic Resonance Imaging 35: 1312-13421, 2012.

[22] Manuel Murbach, Esra Neufeld, Myles Capstick, Wolfgang Kainz, David O. Brunner, Theodoros Samaras, Klaas P. Pruessmann and Niels Kuster. Thermal tissue damage model analyzed for different whold-body SAR and scan durations for standard MR body coils. Magnetic Resonance in Medicine 71: 421-431, 2014.

[23] Sukhoon Oh, Yeun-Chul Ryu, Giuseppe Carluccio, Christopher T. Sica and Christopher M. Collins. Measurement of SAR-induced temperature increase in a phantom and In vivo with comparison to numerical simulation. Magnetic Resonance in Medicine 71: 1923-1931, 2014.

[24] Henry S. Ho. Safety of metallic implants in magnetic resonance imaging. Journal of Magnetic Resonance Imaging 14: 472-477, 2001.

[25] David W. Carmichael, John S. Thornton, Roman Rodionov, Rachel Thornton, Andrew McEvoy, Philip J. Allen and Louis Lemieux. Safety of localizing epilepsy monitoring intracranial electroencephalograph electrodes using MRI: radiofrequency-induced heating. Journal of Magnetic Resonance Imaging 28: 1233-1244, 2008.

[26] Peter Nordbeck, Ingo Weiss, Philipp Ehses, Oliver Ritter, Marcus Warmuth, Florian Fidler, Volker Herold, Peter M. Jakob, Mark E. Ladd, Harald H. Quick and Wolfgang R. Bauer. Measuring RF-induced currents inside implants: impact of device configuration on MRI safety of cardiac pacemaker leads. Magnetic Resonance in Medicine 61: 570-578, 2009.

[27] Michele Tagliati, Joseph Jankovic, Fernando Pagan, Frandy Susatia, Ioannis U. Isaias and Michael S. Okun. Safety of MRI in patients with implanted deep brain stimulation devices. NeuroImage 47: T53-T57, 2009.

[28] Yan Liu, Ji Chen, Frank G. Shellock and Wolfgang Kainz. Computational and experimental studies of an orthopedic implant: MRI-related heating at 1.5-T/64-MHz and 3-T/128 MHz. Journal of Magnetic Resonance Imaging 37: 491-497, 2013.

[29] Allen Taflove and Susan C. Hagness. Computational Electrodynamics: The Finite-Difference Time-Domain Method. Artech House Inc., Norwood, MA, 2005.

[30] Atef Z. Elsherbeni and Veysel Demir. The Finite-Difference Time-Domain Method for Electromagnetics with MATLAB Simulations. SciTech Publishing Inc., Raleigh, NC, 2009.

[31] Umran S. Inan and Robert A. Marshalll. Numerical Electromagnetics: The FDTD Method. Cambridge University Press, 2011.

[32] Kane Yee. Numerical solution of initial boundary value problems involving Maxwell's equations in isotropic media. IEEE Transactions on Antennas and Propagation, 14(3): 302-307, May 1966.

[33] J.-P. Berenger. A perfectly matched layer for the absorption of electromagnetic waves. Journal of Computational Physics, 114(2): 185-200, October 1994.

[34] J.-P. Berenger. Three-dimensional perfectly matched layer for the absorption of electromagnetic waves. Journal of Computational Physics, 127(2): 363-379, September 1996.

[35] Constantine A. Balanis. Advanced Engineering Electromagnetics. John Wiley & Sons, Inc., Hoboken, NJ, 2012.

[36] Whitepaper NVIDIA's Next Generation CUDA Compute Architecture: Fermi. NVIDIA Corporation, 2009.

[37] NVIDIA CUDA Compute Unified Device Architecture Programming Guide Version 1.0. NVIDIA Corporation, 2007.

[38] NVIDIA CUDA C Programming Guide Version 4.0. NVIDIA Corporation, 2011.

[39] Cyril Zeller. Tutorial CUDA. NVIDIA Corporation, 2008.

[40] Tomoake Nagaoka and Soichi Watanabe. A GPU-Based calculation using the three-dimensional FDTD method for electromagnetic field analysis. 32nd Annual International Conference of the IEEE EMBS, 327-330, 2010.

[41] Tomoake Nagaoka and Soichi Watanabe. Acceleration three-dimensional FDTD calculation on GPU clusters for electromagnetic field smulation. 34th Annual International Conference of the IEEE EMBS, 5691-5694, 2012.

[42] Paulius Micikevicius. 3D finite difference computation on GPUs using CUDA. Proceedings of 2nd Workshop on General Purpose Processing on Graphics Processing Units, 79-84, 2009.

[43] Veysel Demir and Atef Z. Elsherbeni. Compute Unified Device Architecture (CUDA) based Finite-Difference Time-Domain (FDTD) implemension. ACES Journal, 25(4): 303-314, 2010.

[44] J. I. Toivanen, T. P. Stefanski, N. Kuster and N. Chavannes. Comparison of CPML implementation for the GPU-Accelerated FDTD solver. Progress In Electromagnetics Research M, 19: 61-75, 2011.

[45] IEEE Standards Coordinating Committee 39. IEEE recommended practice for determining the peak spatial-averaged specific absorption rate (SAR) in the human head from wireless communications devices: measurement techniques. IEEE Std 1528-2013.

[46] Lohith Ganesh Kini. Fast simulation of E1, B1 and specific absorption rate for 7T MRI with the use of graphical processors. Master thesis, Massachusetts Institute of Technology, 2008.

[47] H. H. Pennes. Analysis of tissue and arterial blood temperatures in resting forearm. J. Appl. Physiol., 1: 93-122, 1948.

[48] P. C. Cherry and M. F. Iskander. Calculations of heating patterns of an array of microwave interstitial antennas. IEEE Trans. Biomed. Eng., 40: 771-779, Aug. 1993.

[49] Jianqing Wang and Osamu Fujiwara. FDTD computation of temperature rise in the human head for portable telephones. IEEE Trans. Microwave Theory Tech., 47: 1528-1534, Aug. 1999.

[50] Paolo Bernardi, Marta Cavagnaro, Stefano Pisa and Emanuele Piuzzi. Specific absorption rate and temperature elevation in a subject exposed in the far-field of radio-frequency sources operating in the 10-900 MHz range. IEEE Trans. Biomed. Eng., 50: 295:304, March 2003.

[51] Akimasa Hirata. Temperature increase in human eyes due to near-field and far-field exposures at 900 MHz, 1.5 GHz, and 1.9 GHz. IEEE Trans. Electromagnetic Compatibility, 47: 68-76, Feb. 2005.

[52] Concettina Buccella, Valerio De Santis and Mauro Feliziani. Prediction of temperature increase in human eyes due to RF sources. IEEE Trans. Electromagnetic Compatibility, 49: 825-833, Nov. 2007

[53] Ozisik M. Necati, Heat Transfer: A Basic Approach. Mcgraw-Hill College, 1984.

[54] A.Christ, W. Kainz, E. G. Hahn, K. Honegger, M. Zefferer, E. Neufeld, W. Rascher, R. Janka, W. Bautz, J. Chen, B. Kiefer, P. Schmitt, H. Hollenbach, J. Shen, M. Oberle, D. Szczerba, A. Kam, J. W. Guag, and N. Kuster. The virtual family—Development of surface-based anatomical models of two adults and two children for dosimetric simulations. Phys. Med. Biol., 55(2): N22-N38, 2010.

[55] An internet resource for the calculation of the dielectric properties of body tissues in the frequency range 10Hz-100GHz, http://niremf.ifac.cnr.it/tissprop/.

[56] T. Vaughan, L. DelaBarre, C. Snyder, L. Tian, C. Akgun, D. Shrivastava, W. Liu, C. Olson, G. Adriany, J. Strupp, P. Andersen, A. Gopinath, P. van de Moortele, M. Garwood and K. Ugurbi. 9.4T human MRI: Preliminary results. Magnetic Resonance in Medicine 56: 1274-1282, 2006.

[57] Frank.Seifert, Gerd Wubbeler, Sven Junge, Bernd Ittermann and Herbert Rinneberg. Patient safety concept for multichannel transmit coils. Journal of Magnetic Resonance Imaging 26: 1315-1321, 2007.

[58] A.C. Zelinski, L. M. angelone, V. K. Goyal, G. Bonmassar, E. Adalsteinsson and L. L. Wald. Specific absorption rate studies of the parallel transmission of inner-volume excitations at 7 Tesla. Journal of Magnetic Resonance Imaging 28: 1005-1008, 2008.

[59] M.C. Gosselin, A. Christ, S. K uhn and N. Kuster. Dependence of the occupational exposure to mobile phone base stations on the properties of the antenna and human body. IEEE Trans. Electromagn. Compat., 51(2): 227-235, 2009.

[60] A. Christ, M. G. Douglas, J.M. Roman, E. B. Cooper, A. P. Sample, B. H. Waters, J. R. Smith and N. Kuster. Evaluation of wireless resonant power transfer systems with human electromagnetic exposure limits. IEEE Trans. Electromagn. Compat., 55(2): 265-274, 2013.

[61] K. Baskourelos and T. Samaras. An iterative FDTD/MoM technique for assessing coupling effects in front of base-station antennas. . IEEE Trans. Electromagn. Compat., 54(6): 1310-1313,2012.

[62] G. Cerri, P. Russo, A. Schiavoni, G. Tribellini and P. Bielli. MoM-FDTD hybrid technique for analyzing scattering problems. Electronics Lett., 34(5): 438-450, 1998.

[63] R. Bretones A., R. Mittra and R. G. Martin. A hybrid technique combining the method of moments in the time domain and FDTD. IEEE Microw. Guided Wave Lett., 8(8): 281-283, 1998.

[64] Shumin Wang, Yu Shao and Shizhe Li. Rapid local specific absorption rate estimation for magnetic resonance imaging. IEEE Transactions on Electromagnetic Compatibility, 56(4): 771-779, 2014.

[65] S. Wan. Quasi block cholesky factorization with dynamic matrix compression for fast integral-equation simulations of large scale human body models. Proc. IEEE, 101(2): 389-400, 2013.

[66] S. Wang and J. H. Duyn. Time-domain finite-difference/finite-element hybrid simulations of radio frequency coils in magnetic resonance imaging. Phys. Med. Biol., 53: 2677-2692, 2008.

[67] G. H. Golub and C. F. V. Loan. Matrix Computations, 3rd ed. Baltimore, MD, USA: Johns Hopkins Univ. Press, 1996.

[68] W.C. Chew, J. M. Jin, E. Michielssen and J. M. Song, Eds. Fast and efficient algorithms in computational electromagnetics. Boston, MA, USA: Artech House, 2000.

[69] R. G. Graglia. On the numerical integration of the linear shape functions times the 3-D Greens function or its gradient on a plane triangle. IEEE Trans. Antennas Propag., 41(10): 1448-1455, 1993.

[70] S. Wang, J. Murphy-Boesch, H. Merkle, A. P. Koretsky and J. H. Duyn. B1 control in MRI by multi-layer coupled coils. IEEE Trans. Med. Imag., 28: 551-554, 2009.

[71] C. Gabriel. Compilation of the dielectric properties of body tissues at RF and microwave frequencies. Tech. Rep. AL/OE-TR-1996-0037, San Antonio, TX, USA, Brooks Air Force, 1996.

[72] Zhu Y, Alon L, Deniz CM, Brown R, Sodickson DK. System and SAR characterization in parallel RF transmission. Magnetic Resonance in Medicine 67: 1367-1378, 2012.

[73] Bastien G, Gebhardt M, Cauley S, Adalsteinsson E, Wald LL. Local specific absorption rate (SAR), global SAR, transmitter power, and excitation accuracy trade-offs in low flip-angle parallel transmit pulse design. Magnetic Resonance in Medicine 71: 1446-1457, 2014.

[74] Shajan G, Kozlov M, Hoffmann J, Turner R, Scheffler K, Pohman R. A 16-channel dual-row transmit array in combination with a 31-element receive array for human brain imaging at 9.4T. Magnetic Resonance in Medicine 71: 870-879, 2014.

[75] Tian J, Snyder CJ, Delabarre1 L, Akgun C, Liu W, Collins CM, Gopinath A, Vaughan JT. Effect of head size to B1, SNR and SAR. In Proceedings of the 15th Annual Meeting of ISMRM, Berlin, Bermany, 2011.

[76] de Greef M, Ipek O, Raaijmakers AJE, Crezee J, van den Berg CAT. Specific absorption rate intersubject variability in 7T parallel transmit MRI of the head. Magnetic Resonance in Medicine 69: 1476-1485, 2013.

[77] Ipek O, Raaijmakers AJ, Lagendijk JL, Luijten PR, can der Berg CAT. Intersubject local SAR variation for 7T prostate MR imaging with an eight-channel single-side adapted dipole antenna array. Magnetic Resonance in Medicine 71: 1559-1567, 2014.

[78] Tilley AR, Associates HD. The measure of man and woman: human factors in design. New York: John Wiley & Sons, 2002.

[79] Ball R, Shu C, Xi P. A comparison between Chinese and Caucasian head shapes. Appl Ergon 41: 832-839, 2010.

[80] Murbach M, Neufeld E, Kainz W, Pruessmann KP, Kuster N. Whole-body and local RF absorption in human models as a function of anatomy and position within 1.5T MR body coil. Magnetic Resonance in Medicine 71: 839-845, 2014.

[81] Rubinstein RY, Kroese DP. Simulation and the Monte Carlo method. Wiley series in probability and statistics. New York: John Wiley & Sons, 2007.

[82] Julier SJ, Uhlmann JK. Unscented filtering and nonlinear estimation. Proc IEEE 92: 401-422, 2004.

[83] Steiner G, Watzenig D, Magele C, Baumgartner U. Statistical robust design using the unscented transformation. COMPEL: The International Journal for Computation and Mathematics in Electrical and Electronics Engineering 24: 606-619, 2005.

[84] de Menezes LRAX, Ajayi A, Christopoulos C, Sewell P, Borges CA. Efficient computation of stochastic electromagnetics problems using unscented transforms. IET Sci Means Technol 2:88-95, 2008.

[85] dos Santos I, Haemmerich D, Schutt D, Ferreira da Rocha A, Menezes LR. Probabilistic finite element analysis of radiofrequency liver ablation using the unscented transform. Phys Med Biol 54: 627-640, 2009.

[86] Yu Shao, Peng Zeng and Shumin Wang. Statistical Simulation of SAR variability with geometric and tissue property changes by using the unscented transform. Magnetic Resonance in Medicine, published online 2014.

[87] Saltelli A, Ratto M, Andres T, Campolongo F, Cariboni J, Gatelli D, Saisana M, Tarantola S. Global sensitivity analysis. The primer. New York: John Wiley & Sons, 2008.